

Utah State University

DigitalCommons@USU

All Graduate Theses and Dissertations

Graduate Studies

12-2012

The Application of Tomographic Reconstruction Techniques to Ill-Conditioned Inverse Problems in Atmospheric Science and Biomedical Imaging

Vern Philip Hart II
Utah State University

Follow this and additional works at: <https://digitalcommons.usu.edu/etd>



Part of the [Physics Commons](#)

Recommended Citation

Hart, Vern Philip II, "The Application of Tomographic Reconstruction Techniques to Ill-Conditioned Inverse Problems in Atmospheric Science and Biomedical Imaging" (2012). *All Graduate Theses and Dissertations*. 1354.

<https://digitalcommons.usu.edu/etd/1354>

This Dissertation is brought to you for free and open access by the Graduate Studies at DigitalCommons@USU. It has been accepted for inclusion in All Graduate Theses and Dissertations by an authorized administrator of DigitalCommons@USU. For more information, please contact digitalcommons@usu.edu.



THE APPLICATION OF TOMOGRAPHIC RECONSTRUCTION TECHNIQUES
TO ILL-CONDITIONED INVERSE PROBLEMS IN ATMOSPHERIC
SCIENCE AND BIOMEDICAL IMAGING

by

Vern Philip Hart II

A dissertation submitted in partial fulfillment
of the requirements for the degree

of

DOCTOR OF PHILOSOPHY

in

Physics

Approved:

Timothy E. Doyle
Major Professor

Ludger Scherliess
Committee Member

James T. Wheeler
Committee Member

Joseph V. Koebbe
Committee Member

Eric D. Held
Committee Member

Mark R. McLellan
Vice President for Research and
Dean of the School of Graduate Studies

UTAH STATE UNIVERSITY
Logan, UT

2012

Copyright © Vern Philip Hart II 2012

All Rights Reserved

ABSTRACT

The Application of Tomographic Reconstruction Techniques to
Ill-Conditioned Inverse Problems in Atmospheric Science
and Biomedical Imaging

by

Vern Philip Hart II, Doctor of Philosophy

Utah State University, 2012

Major Professor: Dr. Timothy E. Doyle
Department: Physics

A methodology is presented for creating tomographic reconstructions from various projection data, and the relevance of the results to applications in atmospheric science and biomedical imaging is analyzed. The fundamental differences between transform and iterative methods are described and the properties of the imaging configurations are addressed. The presented results are particularly suited for highly ill-conditioned inverse problems in which the imaging data are restricted as a result of poor angular coverage, limited detector arrays, or insufficient access to an imaging region. The class of reconstruction algorithms commonly used in sparse tomography, the algebraic reconstruction techniques, is presented, analyzed, and compared. These algorithms are iterative in nature and their accuracy depends significantly on the initialization of the algorithm, the so-called initial guess. A considerable amount of research was conducted into novel initialization techniques as a means of improving the accuracy. The main body of this paper is comprised of three smaller papers, which describe the application of the presented methods to atmospheric and

medical imaging modalities. The first paper details the measurement of mesospheric airglow emissions at two camera sites operated by Utah State University. Reconstructions of vertical airglow emission profiles are presented, including three-dimensional models of the layer formed using a novel fanning technique. The second paper describes the application of the method to the imaging of polar mesospheric clouds (PMCs) by NASA's Aeronomy of Ice in the Mesosphere (AIM) satellite. The contrasting elements of straight-line and diffusive tomography are also discussed in the context of ill-conditioned imaging problems. A number of developing modalities in medical tomography use near-infrared light, which interacts strongly with biological tissue and results in significant optical scattering. In order to perform tomography on the diffused signal, simulations must be incorporated into the algorithm, which describe the sporadic photon migration. The third paper presents a novel Monte Carlo technique derived from the optical scattering solution for spheroidal particles designed to mimic mitochondria and deformed cell nuclei. Simulated results of optical diffusion are presented. The potential for improving existing imaging modalities through continual development of sparse tomography and optical scattering methods is discussed.

(167 pages)

PUBLIC ABSTRACT

Vern Philip Hart II

Tomography is an imaging technique in which 3D models of objects are created from several 2D projections viewed at different angles. When the number of available projections is limited, the resulting data are said to be sparse. This restriction is often a direct result of the imaging geometry used to acquire the data. One-sided views and a small number of receivers can reduce the range of available projections, which makes the object more difficult to reconstruct. Approximate solutions to difficult imaging problems can be obtained using a class of iterative algorithms known as the algebraic reconstruction techniques (ARTs). The presented research examines some of the capabilities of these algorithms and results are presented, which demonstrate that under particular initialization conditions, these algorithms are able to accurately reproduce structure in the imaging object. The presented technique is then applied to atmospheric science and biomedical imaging to further explore its capabilities and potential.

DEDICATION

To my loving wife, Janelle

ACKNOWLEDGMENTS

I wish to first and foremost thank my wife, Janelle, whose patience and tireless support have made all of this possible. I am fortunate to have such a wonderful family, my source of joy in all that I do. I have much to be thankful for.

I owe an incalculable debt to my advisor, mentor, and friend, Dr. Timothy E. Doyle, who has inspired and made possible all that I have accomplished during my time in graduate school and all that I wish to accomplish throughout my career. Without him I would not be where I am today and would not be going where I am in the future.

I would like to thank Dr. Michael J. Taylor, who has provided much of the funding for this project and has been a valuable collaborator and friend. He made this research possible and deserves a significant amount of recognition and praise for the resulting publications. I owe him much and I am grateful for his contributions to my graduate career.

I wish to thank all of the faculty and staff in the Physics Department at Utah State University, as well as my fellow students. Each of you contributed in some way to my success and I owe you a great deal of gratitude. I thoroughly enjoyed working with you and will always be thankful for your influence in my life.

I would like to thank Karalee Ransom for assisting me so selflessly during my initial enrollment at USU and for continuing to provide me and my family with the help that we needed.

I am grateful for the grants and scholarships, which made this research possible. They include: NIH-NCI Grant No. 1 R21 CA131798-01A1, NSF Grant No. ATM 0536876, and the University-based RC Grant and Seeley-Hinckley Scholarship. My experience at USU has been valuable and I will always be thankful for the education I received here. It will always be a part of who I am and I will forever be grateful for it.

Vern Philip Hart II

CONTENTS

	Page
ABSTRACT.....	iii
PUBLIC ABSTRACT	v
ACKNOWLEDGMENTS	vii
LIST OF FIGURES	xi
CHAPTER	
1 INTRODUCTION	1
2 TOMOGRAPHIC THEORY	6
2.1 Transform Methods	6
2.1.1 Radon Transforms.....	7
2.1.2 Fourier Transforms.....	9
2.2 Back Projection	13
2.3 Matrix Methods	14
3 CORRECTION ALGORITHMS.....	18
3.1 The Kaczmarz Method	18
3.2 Algebraic Reconstruction Techniques.....	21
3.3 Initialization.....	24
4 THREE-DIMENSIONAL TOMOGRAPHIC RECONSTRUCTION OF MESO- SPHERIC AIRGLOW STRUCTURES USING TWO-STATION GROUND-BASED IMAGE MEASUREMENTS.....	29
4.1 Introduction	30
4.2 Methods	33
4.2.1 Imaging Configuration.....	33
4.2.2 Tomographic Theory.....	36
4.3 Results	42

4.3.1	Synthetic Data and Validation	42
4.3.2	Airglow Layer Reconstructions	49
4.3.3	Three-Dimensional Mapping of Airglow.....	50
4.4	Discussion.....	52
4.5	Conclusion.....	55
5	TOMOGRAPHIC RECONSTRUCTION OF POLAR MESOSPHERIC CLOUD PROFILES FROM IMAGE DATA COLLECTED DURING THE NASA AIM SATELLITE MISSION	56
5.1	Introduction	56
5.2	Methods	60
5.2.1	Imaging Configuration	61
5.2.2	Tomographic Theory.....	63
5.2.3	Data Interpolation.....	67
5.3	Results	68
5.3.1	Synthetic Data and Validation	69
5.3.2	PMC Layer Reconstructions	71
5.4	Discussion.....	74
5.5	Conclusion	81
6	DIFFUSE TOMOGRAPHY	82
7	A SPHEROIDAL SCATTERING TECHNIQUE FOR SIMULATING DIFFUSE PHOTON MIGRATION IN OPTICAL TOMOGRAPHY OF BIOLOGICAL TISSUE.....	86
7.1	Introduction	86
7.2	Spheroidal Scattering.....	89
7.2.1	Scattering Configuration	90
7.2.2	Spheroidal Coordinates	92
7.2.3	Spheroidal Wave Functions	93
7.2.4	Scattering Solution	96
7.2.5	Scattering Parameters.....	99
7.3	Photon Migration Models in DOT.....	101

7.3.1	Phase Functions.....	102
7.3.2	Mie Scattering	103
7.3.3	Spheroidal Scattering	104
7.4	Results	107
7.5	Discussion.....	110
7.6	Conclusion.....	113
8	CONCLUSION.....	115
	REFERENCES	117
	APPENDICES	128
A	A LAYERED INITIALIZATION TECHNIQUE.....	129
B	ADDITIONAL SCATTERING IMAGES	133
C	SPHEROIDAL COORDINATES	138
D	LETTERS OF PERMISSION	141
	CURRICULUM VITAE	147

LIST OF FIGURES

Figure	Page
2.1 An illustration of the fundamental definition of a projection in straight-line tomography	7
2.2 The fan beam projection used in tomographic imaging.....	10
2.3 The parallel projection used in tomographic imaging	11
2.4 A demonstration of the back projection method commonly used in diagnostic imaging	15
2.5 The discretized representation of an imaging region used in matrix methods	17
3.1 An illustration of the Kaczmarz method for iteratively finding solutions to linear systems of equations	20
3.2 The results of using a constant initial guess for grids of varying size	26
3.3 The effect the altitude of an initial profile has on the accuracy of reconstructed images	27
4.1 Synchronous OH airglow images from BLO and SVO recorded on February 15, 2009 at 07:51:32 UT showing gravity wave structures	36
4.2 Time sequence of OH airglow images from the BLO (left) and SVO (right) with a 7.5 minute difference between successive images illustrating coherent wave motion (indicated by arrows)	37
4.3 An example of the overlapping technique used to align simultaneous images from BLO and SVO.....	38
4.4 Plots of OH emission brightness for BLO (top) and SVO (center) along a common 120km profile (indicated by the yellow line in Fig. 4.1)	39
4.5 An illustration of the discretized imaging region used in algebraic tomography	40
4.6 The reconstructed results of synthetic testing performed using the three initial profiles shown in Fig. 4.7	45
4.7 Three of the profiles used to initialize the reconstruction algorithm during synthetic testing.....	47

4.8	An average volume emission rate (VER) profile of the OH emission determined from SABER observations onboard NASA's TIMED satellite.....	48
4.9	A cross-sectional tomographic reconstruction of the OH layer using data from two ground-based CCD cameras and constrained using a Gaussian profile	49
4.10	A sketch showing the fanning configuration applied to the airglow data.....	50
4.11	A composite 3D rendering of the airglow layer formed by combining 180 individual 2D reconstructions using the fanning geometry of Fig. 4.10	51
4.12	An expanded view of the 3D airglow mapping shown in Fig. 4.11	52
4.13	The lower portion of the 3D airglow mapping shown in Fig. 4.11 segmented normal to the wave crests.....	53
5.1	An illustration of the imaging configuration from which the reconstructed data were acquired.....	62
5.2	An example of a composite scene created from images acquired by the four CIPS cameras onboard the AIM satellite	63
5.3	The interpolation procedure used to refine the 2km spatial resolution of the data collected by the satellite-based CIPS cameras.....	68
5.4	The Gaussian layer used to initialize the PCART algorithm in the synthetic testing and PMC reconstructions.....	69
5.5	Typical synthetic testing performed using an artificially generated object in combination with a Gaussian initial guess and actual imaging configuration.....	71
5.6	Tomographic reconstructions of the PMC layer from data collected by the CIPS cameras onboard the AIM satellite, shown with increasingly higher resolution from top (a) to bottom (d).....	73
5.7	The predicted layer thickness as a function of interpolated resolution.....	74
5.8	Various portions of the 0.25km-resolution reconstruction of the PMC layer shown in Fig.5.6	75
5.9	Additional portions of the 0.25km-resolution reconstruction.....	76

5.10	A proposed method for creating 3D reconstructions of PMCs using the CIPS image data from the AIM satellite and the fanning technique developed by the authors for use in airglow tomography	78
5.11	Vertical emission profile centroids plotted against position.....	80
6.1	A diffusive random-walk simulation demonstrating sporadic photon migration	83
7.1	The prolate spheroidal coordinate system.....	93
7.2	Simulations of the scattered wave fields measured away from a spheroidal particle.....	100
7.3	The scattered intensity of light measured on the surface of a spheroid for the case of $\zeta=0.3$	101
7.4	The scattered intensity of light measured on the surface of a sphere	105
7.5	The scattered intensity of light measured on the surface of a spheroid for the case of $\zeta=0$	106
7.6	A diagram of scattering events in the spheroidal coordinate system.....	107
7.7	A simulated diffusion profile along the plane $y=0$ using isotropic scattering	108
7.8	Diffused intensity measured along the surface of the tissue	109
7.9	A 3D model of optical diffusion in biological tissue	110
7.10	A cross-sectional view of the 3D model of optical diffusion in biological tissue	111
7.11	A comparison of diffusion profiles formed using various scattering techniques	112
7.12	Plots of depth intensities measured along the z axes of the diffusion profiles shown in Fig. 7.11	113
A.1	Reconstructed intensities using a single-layer initial profile	131
A.2	A plot of the normalized layer intensities against altitude.....	132
B.1	An explanation of the axes omitted in the subsequent scattering diagrams.....	133

B.2	Additional scattering images shown for incident angles $\zeta=0.60^\circ$ through $\zeta=24.64^\circ$	134
B.3	Additional scattering images shown for incident angles $\zeta=26.36^\circ$ through $\zeta=50.42^\circ$	135
B.4	Additional scattering images shown for incident angles $\zeta=52.14^\circ$ through $\zeta=76.20^\circ$	136
B.5	Additional scattering images shown for incident angles $\zeta=77.92^\circ$ through $\zeta=89.95^\circ$	137
C.1	An explanation of the prolate spheroidal coordinate system	139

CHAPTER 1

INTRODUCTION

Optical tomography is a rapidly evolving field, which has experienced a significant number of new developments in the last few decades. The introduction of novel imaging modalities and the expansion of conventional tomographic applications to a wider variety of studies continues to increase. Conventional tomography has long been associated with clinical applications because of its broad use and likely because the technology has its origins in the medical industry. The first functional computerized tomography (CT) scanner was developed for diagnostic purposes, and preserved human brains were among the first objects to be tested by prototypes of the machine. The concept for CT was first proposed by Hounsfield (and concurrently by Cormack) when he postulated that the structure of an object hidden in a box could be recreated using x-ray or gamma ray measurements taken at different angles [1]. This would be accomplished by considering the object to be a series of two-dimensional slices. The attenuation coefficient of a given region could then be determined using a matrix formalism as will be explained further in the following chapters.

A working prototype was built on a lathe bed, which utilized transuranic Americium 95 as a gamma ray source, and a photon detector was placed opposite the emitting sample with an imaging object between them. The scan required 9 hours to complete a 180° rotation and 2.5 hours to computationally reconstruct the image [1]. After Hounsfield tested the machine on various animal organs, and eventually on himself, the first working model was introduced at Atkinson Morley Hospital in Wimbeldon, London in 1971 [2]. An interesting observation is made in the description of the first full-body scanner. It is noted that the imaging region (the body) is represented by 6,400 volume cubes and that the number of projected rays through this region is 28,800 ($160 \times 180^\circ$). This configuration results in 28,800 simultaneous equations and only 6,400 variables, constituting an overdetermined system of equations. Hounsfield then states that, providing there are more equations than

variables, the system can be solved. “In short there must be more x-ray readings than picture points” [2].

The unprecedented imaging capabilities of CT were soon demonstrated by comparing known absorption coefficients to corresponding pixel densities. The accuracy of the reconstructions was characterized by a $\sim 0.5\%$ error, surpassing the theoretically predicted value of 1%. The results led to CT being introduced at hospitals worldwide over the next several years and eventually becoming a mainstream diagnostic tool. The computational limitations of the 1970s meant that reconstructions were slow and the tomographic algorithms were eventually abandoned in favor of a back projection method. It was believed at the time that, in order to perform a large number of scans, the reconstructions would need to be processed at a central mainframe and that it could potentially limit further improvements to the technique [1]. Computational and algorithmic developments have since revolutionized the field of tomography. Advances in reconstruction algorithms and significantly faster processing speeds, which allow for practical implementation of complex algorithms, have reduced the need for overdetermined systems. This has allowed for the application of tomographic techniques to a vast new range of fields.

The concept of an underdetermined system being solved computationally had been explored prior to the introduction of medical tomography, but seemed impractical at the time [1]. The algebraic reconstruction technique (ART), an image processing algorithm derived from the Kaczmarz method of linear algebra, had been developed for electron microscopy and was capable of reconstructing an image from an underdetermined system of equations with varying accuracy [3]. A number of tomographic applications were suggested in the years following (and preceding) the introduction of CT, which did not allow for the same amount of data collection as was feasible with the higher resolution provided by x-rays. In 1963 Cormack proposed positron annihilation radiation scanning (a predecessor of positron emission tomography) and tomography using heavy charged particles, such as protons [4].

Crowe and his colleagues developed a successful tomograph utilizing 910 MeV helium ions in 1975 [5].

Conventional CT allows for the acquisition of large amounts of data. Depending on the intensities used, photon counts from an x-ray source can be high and scans can be performed from any angle as the detector is rotated around the imaging object. The resulting system of simultaneous equations is overdetermined and the inverse problem is said to be well-conditioned. Most modern tomographic applications, many of which were initially proposed in the years following the introduction of CT, do not inherently provide significant amounts of data. The resulting projections are said to be sparse, the system of equations underdetermined, and the inverse problem ill-conditioned.

A number of factors influence the amount of data collected during a scan. Projections can be sparse if the intensity of the radiation is low. For example, the data acquired from mammograms are generated by a low-intensity x-ray in an attempt to reduce the total radiation exposure of vital organs. A recent development known as digital mammography [6] attempts to reduce the necessary exposure time allowing for more accurate diagnosis with less risk to surrounding regions of the body. Nuclear imaging [7] and neuroimaging [8] also require low radiation doses, which lead to a weak signal and sparse data. The prostate is a deep organ with limited exterior access and it has been suggested that an endorectal probe could be placed close enough to the prostate wall for sufficient tomographic information to be collected [9]. Any data collected in this manner, however, would be inherently one-sided and would also be geometrically limited in its angular coverage. The small diameter of the probe would limit the number of detectors available for measuring signal attenuation. The resulting data would thus be inherently sparse. A large imaging region, such as a cloud layer, can also be difficult to access from a variety of angles, thereby reducing the angular coverage of the rays [10]. These and other uses of tomography exhibit inherently limited imaging configurations, which complicate the accurate reconstruction of projection data.

The difficulties associated with solving underdetermined systems have been significantly reduced by advances in iterative reconstruction algorithms. A number of variations of the ART algorithm have been developed and together constitute the class of algebraic reconstruction techniques (ARTs). Given proper initial conditions, the ART algorithms are capable of approximating solutions to systems with several times (some systems have required as many as 50) more variables than equations. These and other technological advances, specifically in data collection, continue to drive the creation of new imaging modalities and have allowed for a diverse range of tomographic applications. Medical imaging modalities now include (but are not limited to) optical coherence tomography (OCT) [11], positron emission tomography (PET) [12], single photon emission computed tomography (SPECT) [13], and diffuse optical tomography (DOT) [14]. Tomographic methods have been used to measure the thickness of nerve fiber layers in the study of ocular diseases [15], conduct void analysis in thin soil sections [16], measure crystal defects [17], and have proven to be an effective tool in numerous other studies.

This paper presents research into novel techniques for initializing and tomographically reconstructing sparse or one-sided imaging data. The capabilities of these techniques are examined in the context of their application to atmospheric and biomedical imaging. The foundational theories of tomography are presented, including transform and back projection methods commonly used in medical imaging. The fundamental properties of discrete tomographic descriptions, which are relevant to sparse projection data and limited imaging configurations, are analyzed. The class of algebraic reconstruction techniques (ARTs) are presented and the behavior of the individual algorithms is examined using a simulated imaging region and a synthetic object. The influence of the initial guess on the convergence of an iterative reconstruction algorithm is also demonstrated using simulations.

Three individual papers are then presented, which apply these ART reconstruction algorithms to airglow imaging experiments conducted at Utah State University, satellite images

of PMC layers, and optical biomedical imaging. The first paper explains, in further detail, the methods and relevant algorithms used to image the airglow layer, and the results of the tomographic reconstructions are presented. The second paper describes the application of ART algorithms to imaging polar mesospheric clouds from data acquired by NASA's Aeronomy of Ice in the Mesosphere (AIM) satellite. A novel technique is presented, which detects height variations in the layer using brightness asymmetries in the reconstructed images. The third paper discusses the application of sparse reconstruction algorithms to biomedical imaging in the context of diffuse tomography methods. Monte Carlo techniques used to simulate diffuse photon migration in biological tissue are presented and a description of Mie scattering theory is given. The phase function methods often used to describe optical diffusion in tissue are discussed. A novel Monte Carlo technique based on the optical scattering solution for a spheroidal particle is then presented. This method is used to model sporadic photon migration in tissue and the interaction of light with cells and intracellular structures. Mitochondria and deformed cell nuclei, which account for a significant amount of cellular scattering, are spheroidal in shape. The spheroidal scattering method is therefore proposed to be a more physical approach than phase function techniques. Results of simulated optical diffusion are presented. Finally, the capabilities of sparse tomographic techniques are summarized, and the prospects of improving existing imaging modalities through advanced scattering and reconstruction methods are analyzed and discussed.

CHAPTER 2

TOMOGRAPHIC THEORY

The primary function of straight-line tomography is the recreation of structure from multiple attenuated projections measured through a range of angles. The processes used to reconstruct the object typically belong to one of three classifications: transform methods, back projection methods, and matrix methods. These techniques form the foundation of tomographic theory and are discussed in detail in the following sections, beginning with transform methods, which are perhaps the most fundamental. Back projection methods are commonly used in medical CT and provide an example of algorithm initialization, which is discussed in further detail in subsequent chapters. Matrix methods are pertinent to sparse tomography and have been used to reconstruct the airglow and polar mesospheric cloud layers presented in this paper.

2.1. Transform Methods

A fundamental tomographic description typically quantifies the effect that an imaging object has on a projection. Physically, this represents the attenuation of the traversing radiation being measured on the other side of the imaging region. A description of the interaction between the projections and the object allows its structure to be determined using tomographic methods. A mapping of absorption coefficients or other properties, which are closely related to the density of an object, can thereby produce images of its internal structure. In some instances the measured signal is not being absorbed but emitted. There are applications (such as airglow tomography) in which an emissive object is being imaged and the radiated intensity is analogous to the attenuated signal used in other applications. The presented projection imagery differs slightly between the two cases, but the underlying principle remains the same. A description is established to quantify the effect that a region of the object has on the signal measured at a given angle. From this information, the object

can be reconstructed. The subsequent derivations follow the style of the text by Kak and Slaney [18].

2.1.1. Radon Transforms

In simple form, a two-dimensional (2D) cross section of an inhomogeneous imaging object may be represented as a function of two variables (x,y) :

$$\text{object} \rightarrow f(x,y). \quad (2.1)$$

If a given straight path through the object is defined by two parametric variables (θ, t) , as shown in Fig. 2.1, then the projection through $f(x,y)$ along s can be represented by the line integral

$$P(\theta, t) = \int_{(\theta, t) \text{ line}} f(x,y) ds. \quad (2.2)$$

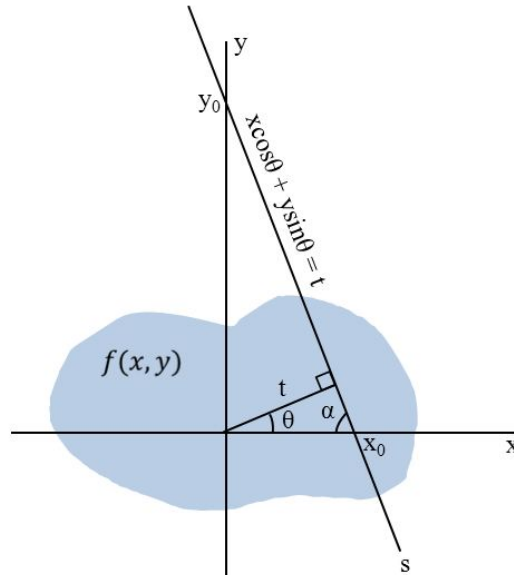


Fig. 2.1. An illustration of the fundamental definition of a projection in straight-line tomography. The projection $P(\theta, t)$ is defined as the line integral of $f(x,y)$ along (straight) curve s . The line is parameterized by two variables, θ and t . The parameterized equation of s is shown in the figure and is used in the argument of a delta function to restrict all-space integrals to a single path in Radon transforms.

The equation of the line s in terms of x, y , and t can be deduced from the diagram. The y -intercept of s is denoted by y_0 in the figure and the x -intercept by x_0 . Given the line's orientation, its slope can be expressed by

$$slope = \frac{y_0}{(-x_0)}, \quad (2.3)$$

and the equation of the line can then be written as

$$y = y_0 - \frac{y_0}{x_0}x. \quad (2.4)$$

The angle denoted by α in the figure is seen to be complementary to θ and thus

$$\alpha = \frac{\pi}{2} - \theta. \quad (2.5)$$

Notice that the slope of s can also be expressed using:

$$slope = -\frac{y_0}{x_0} = -\tan\alpha = -\tan\left(\frac{\pi}{2} - \theta\right) = -\cot\theta = -\frac{\cos\theta}{\sin\theta}. \quad (2.6)$$

Also, notice the following:

$$\sin\theta = \frac{t}{y_0} \rightarrow y_0 = \frac{t}{\sin\theta}. \quad (2.7)$$

The equation of s is then written as

$$y = \frac{t}{\sin\theta} - \frac{\cos\theta}{\sin\theta}x. \quad (2.8)$$

Multiplying through and rearranging gives:

$$x\cos\theta + y\sin\theta = t \quad (2.9)$$

for the parametric description of the line s in terms of x, y , and t . A delta function utilizing our parametric form can then be used to select a single path through the imaging region. This allows us to convert our line integral to an all-space integral as follows:

$$P(\theta, t) = \int_{-\infty}^{\infty} \int_{-\infty}^{\infty} f(x, y) \delta(x\cos\theta + y\sin\theta - t) dx dy. \quad (2.10)$$

This function, $P(\theta, t)$, is known as the Radon transform of $f(x, y)$ and serves as the fundamental basis for the description of projections in transform methods. Once projection data have been acquired, an inverse Radon transform can then be applied to solve for $f(x, y)$ and recover the structure of the object. A number of inverse techniques have been suggested since the original Radon transform was proposed in 1917 [19]. Durrani and Bisset [20] define the Radon transform as:

$$R_{p\tau}\{f(x, y)\} \triangleq U(p, \tau) = \int_{-\infty}^{\infty} \int_{-\infty}^{\infty} f(x, y) \delta[y - (\tau + px)] dy dx, \quad (2.11)$$

where p represents the slope of the line and τ its intercept, analogous to the previous definition. The inverse Radon transform (suggested by Robinson [21]) is then given by

$$f(x, y) = \frac{1}{2\pi} \int_{-\infty}^{\infty} \frac{d}{dy} H\{U(p, y - px)\} dp, \quad (2.12)$$

where $\tau = y - px$ and H is the Hilbert transform operator.

2.1.2. Fourier Transforms

A number of alternative transforms exist for recovering the structure of an imaged object. Once the projection of a ray is defined in terms of a certain operator, the inverse operator can be applied to recover $f(x, y)$. For this reason, transform methods are sometimes referred to as inverse methods or inversion methods. Common transforms used in tomography include Lorentz [21], Fourier [18], Laplace [22], and Hilbert [20] transforms, in addition to the Radon transform, which has multiple inverse definitions.

The Fourier slice theorem is another inversion technique, which makes use of the Fourier transform. A complete explanation of the theory requires the introduction of two types of projection arrays. When the rays emanate from a point source (theoretical) the configuration is known as a fan beam projection and is shown in Fig. 2.2. This orientation is often appropriate for imaging modalities, which make use of a single emitter or receiver. It is also applicable if the emitter and detector arrays are separated by a large distance as in

the case of the airglow and AIM research. A detector of finite size can be approximated as point-like in the limit that the separation distance becomes large relative to the size of the detector. Alternatively, if an array of detectors and emitters are in relatively close proximity to each other, the resulting rays do not diverge as in the previous case. This is known as a parallel projection and is shown in Fig. 2.3. Since the series of rays share the same orientation angle in the parallel projection, a Radon transform can be defined for each angle, which is only a function of the separation distance t . The projection takes the form $P_\theta(t)$ in parallel and $P(\theta, t)$ in the fan beam orientation.

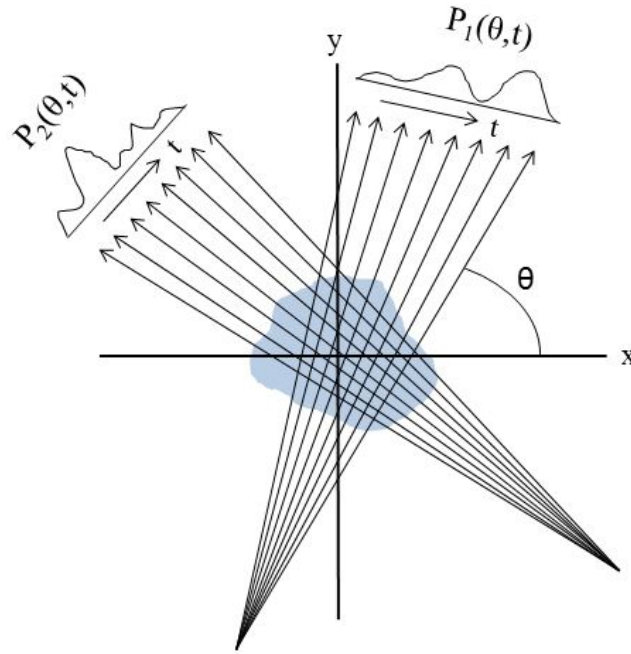


Fig. 2.2. The fan beam projection used in tomographic imaging. The projected rays emanate from a series of individual point sources and spread through a range of angles. The projections measured using this technique are inherently functions of θ and t since a given emission point exhibits multiple projection angles.

The series of rays oriented at a given angle in a parallel projection form a projection function as seen in the figure. The Fourier slice theorem states that the one-dimensional Fourier transform of a parallel projection function is equal to the corresponding slice of

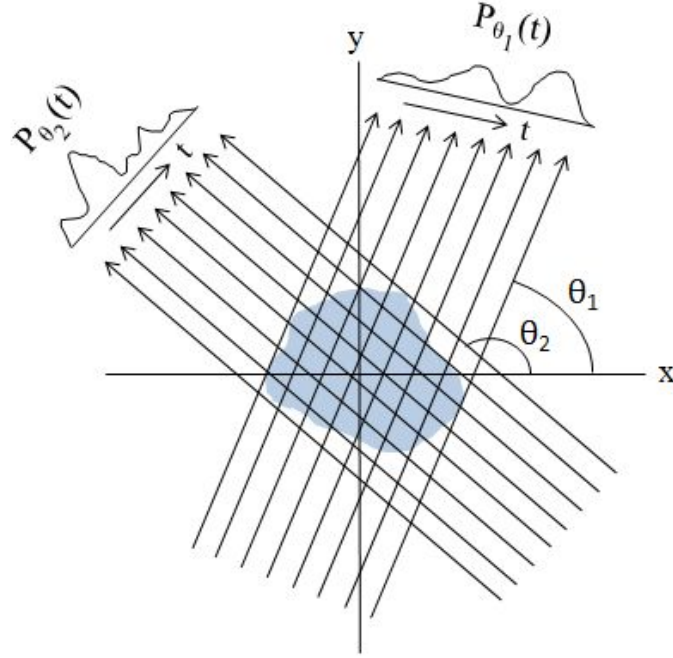


Fig. 2.3. The parallel projection used in tomographic imaging. The projected rays emanate from a series of linear array sources defined by a specific angle. The projections measured using this technique are inherently functions of t only since the rays leaving a given emission location are characterized by a single angle.

the two-dimensional Fourier transform of the original object. Given the measured projection data, the two-dimensional object function $f(x,y)$ can be recovered by performing an inverse 2D Fourier transform. A more rigorous description of the theory can be obtained by considering the (t,s) coordinate system to be a rotated version of the (x,y) coordinate system [18]. The parameterized coordinates of the line integrals defining the projections can be related to the coordinate system of the imaging object through the use of a rotation matrix

$$\begin{bmatrix} t \\ s \end{bmatrix} = \begin{bmatrix} \cos \theta & \sin \theta \\ -\sin \theta & \cos \theta \end{bmatrix} \begin{bmatrix} x \\ y \end{bmatrix}. \quad (2.13)$$

In this coordinate system, a linear path is represented by a curve of constant t and the

parallel projection along such a line is given by

$$P_\theta(t) = \int_{-\infty}^{\infty} f(t, s) ds. \quad (2.14)$$

The Fourier transform of a projection is defined as

$$S_\theta(\omega) = \int_{-\infty}^{\infty} P_\theta(t) e^{-2\pi i \omega t} dt, \quad (2.15)$$

or equivalently

$$S_\theta(\omega) = \int_{-\infty}^{\infty} \int_{-\infty}^{\infty} f(t, s) e^{-2\pi i \omega t} ds dt. \quad (2.16)$$

The rotation matrix can be used to map this result into the (x, y) coordinate system:

$$S_\theta(\omega) = \int_{-\infty}^{\infty} \int_{-\infty}^{\infty} f(x, y) e^{-2\pi i \omega (x \cos \theta + y \sin \theta)} dx dy. \quad (2.17)$$

This result represents a 2D Fourier transform of $f(x, y)$:

$$S_\theta(\omega) = \mathcal{F}(\omega, \theta) = \mathcal{F}\{f(x, y)\}. \quad (2.18)$$

This equation is a mathematical representation of the Fourier slice theorem and is a fundamental relationship in straight-line tomography [18]. The object function $f(x, y)$ can then be recovered by performing an inverse 2D Fourier transform as follows

$$f(x, y) = \int_{-\infty}^{\infty} \int_{-\infty}^{\infty} \mathcal{F}(u, v) e^{2\pi i (ux + vy)} du dv, \quad (2.19)$$

where the definitions $u = \omega \cos \theta$ and $v = \omega \sin \theta$ have been used. The theory requires that if the object function is to be completely determined, the value of the Fourier transform $\mathcal{F}(u, v)$ must be known at each point in the uv plane. This condition necessitates the theoretical existence of an infinite number of projections. Practically, if a finite number of projections are measured, the projection function can be interpolated from the resulting data. The accuracy of this approach, however, is then dependant upon the coverage density of the rays. The set of projections must be sufficiently large in order for an approximation of this type to be valid. This can be accomplished by using a large number of emitters

and detectors or with arrays exhibiting sufficiently high resolutions. In medical CT, virtual arrays are created by rotating x-ray sources and receivers around the imaging region. Transform methods are applicable to medical applications because large data sets and excellent angular coverage are readily available.

2.2. Back Projection

In some ways, the medical applications of CT are unique among the variety of uses for tomography. The wide angular coverage and dense projection data made available by rotating the source arrays are atypical despite their familiarity. Projection data are so plentiful in medical CT that they enable the use of a reconstruction technique, which is not practical in most other forms of tomography. The back projection method requires little calculation and is thereby faster than inversion techniques and significantly faster than iterative techniques. For this reason, it has replaced other reconstruction methods as the preferred rendering technique in most clinical imaging modalities. Medical applications constitute its primary use because the accurate reconstruction of complex systems utilizing an algorithm based solely on a back-projected image requires massive amounts of data measured through a full range of angles [18].

In back projection, a series of parallel rays are projected through the imaging object and the attenuation of the incident radiation at a given angle is then recorded. Since the intensities of the incident and attenuated signals are known, the contribution of the unknown imaging object to the measured projection can be quantified. The path a projection takes through the imaging object can be interpolated from the width of the beam and the angle of incidence. An image is then formed by projecting the measured signal backwards across the path it took through the imaging object. This process is demonstrated using a homogenous spheroid in Fig. 2.4. The measured signals are projected back across the imaging region. Initially the result does not resemble the original object. However, once multiple projections are included from a wide range of angles, the reconstruction begins

to take form. The recreation of complex internal structure requires a significant number of back projections, which interfere constructively to produce fine detail. The background of the image, not common to each projection, can be removed in order to enhance clarity as shown in the figure. For this reason, the presented technique is sometimes referred to as filtered back projection as the ambient signal is filtered out to accentuate the structure of the imaging object.

2.3. Matrix Methods

It is apparent from the figures that a small number of projections are not able to recreate a complex imaging object via back projection. The accuracy of transform methods is also limited by the density of projection data. Sparse or sporadic data are not a good approximation of smooth integral functions. There are a number of fields including geophysics, aeronomy, soil science, and oceanography, among others, in which access to an imaging object is limited and opportunities to collect data through large ranges of angles are not available. Even certain medical imaging modalities, because of concern for exposure to vital organs or the wavelength of light being used, do not allow vast amounts of projection data to be collected. Tomographic applications of this type rely on a class of tomographic techniques known as matrix methods, which are particularly suited to sparse projections. Matrix methods were ironically the first to be developed for use in CT and were implemented by Hounsfield in his original body scanner. The gamma ray source he was using provided relatively low photon counts, which were easily incorporated into a discrete representation. Many emerging applications of tomography rely on a matrix formalism and improving the accuracy and applicability of iterative reconstruction algorithms has been a heavily researched topic in recent years. Matrix methods are introduced briefly as they are discussed in further detail in later chapters.

Matrix methods are typically invoked when available data are limited and a description of the imaging object as a continuous function is no longer valid. A discontinuous

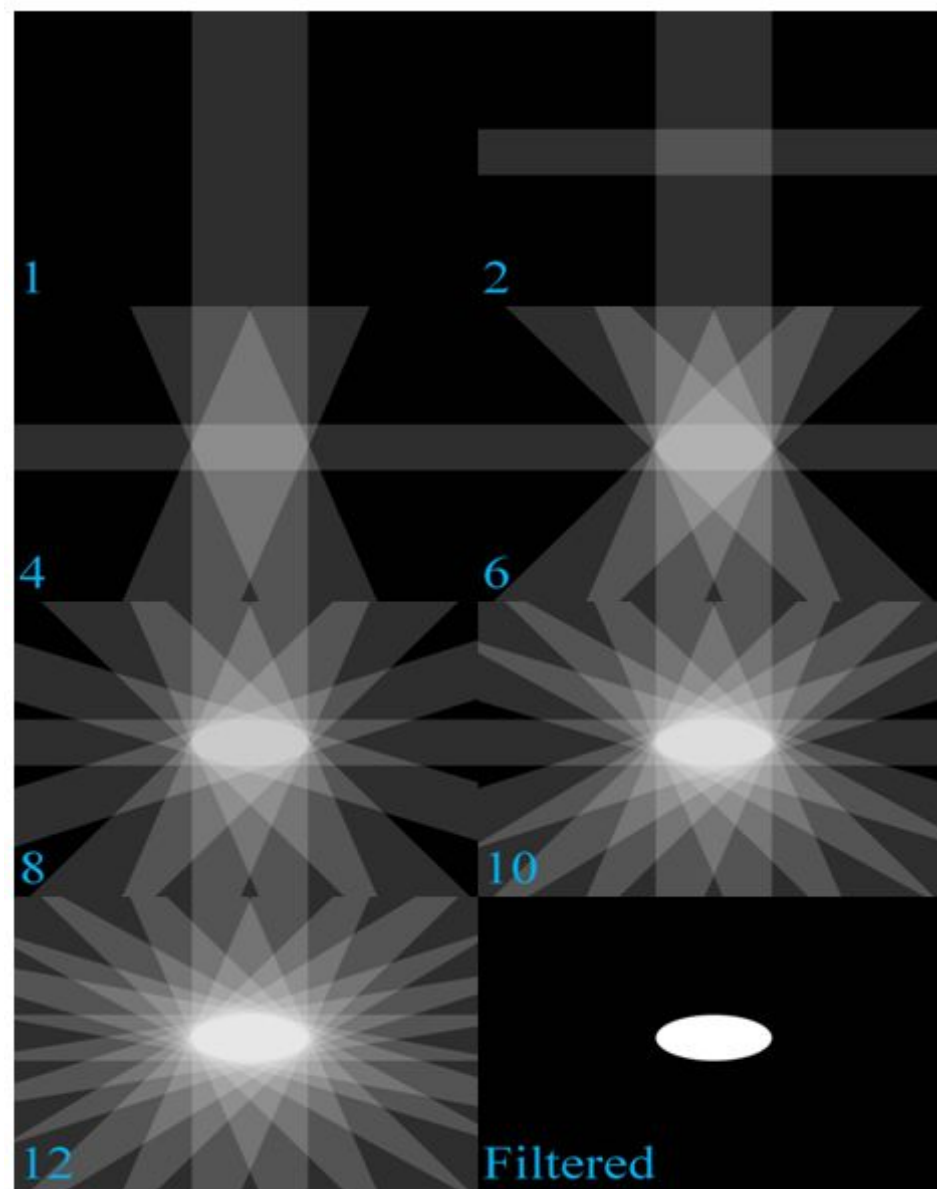


Fig. 2.4. A demonstration of the back projection method commonly used in diagnostic imaging. The attenuation of a signal emitted at a specific angle is recorded and projected back across the imaging region. The process is repeated for each emission angle and the projections constructively interfere to form an image. The background of the reconstruction can be filtered out to provide clarity in a process called filtered back projection. The accuracy of this technique is predicated upon the use of large amounts of projection data collected through a full range of angles. For this reason, the technique is often restricted to medical CT.

approximation is then adopted in which the imaging object is discretized into a grid of constant-valued pixels as shown in Fig. 2.5. The projected rays become finite and a projection is no longer defined to be a series of line integrals, but rather the area between two adjacent rays. The effect that the imaging object has on the attenuated signal is represented by the contribution of each pixel. The signal measured at a given angle is equivalent to the sum of the interactions with each pixel in the grid. The contribution of a given pixel to a projection is defined by the weighting factor w . The weighting factor is calculated to be the normalized area of intersection between the pixel and the projection as seen in the figure. The projected signal p incurs a linear relationship and is expressed as the product

$$p = wf, \quad (2.20)$$

where f is the numerical value of the pixel. The measured projection resulting from interactions with multiple pixels can then be expressed as the sum

$$p = \sum_{n=1}^N w_n f_n \quad (2.21)$$

for N total interactions. In matrix methods the number of rays reaching a receiver is defined to be finite and the projection of the m_{th} ray through the imaging object is given by

$$p_m = \sum_{n=1}^N w_{m,n} f_n. \quad (2.22)$$

Multiple projections through the imaging object constitute a system of linear equations:

$$w_{11}f_1 + w_{12}f_2 + w_{13}f_3 + \cdots + w_{1N}f_N = p_1, \quad (2.23)$$

$$w_{21}f_1 + w_{22}f_2 + w_{23}f_3 + \cdots + w_{2N}f_N = p_2, \quad (2.24)$$

$$\vdots$$

$$w_{M1}f_1 + w_{M2}f_2 + w_{M3}f_3 + \cdots + w_{MN}f_N = p_M, \quad (2.25)$$

which can be expressed as a matrix equation:

$$\begin{bmatrix} w_{11} & w_{12} & w_{13} & \cdots & w_{1N} \\ w_{21} & w_{22} & w_{23} & \cdots & w_{2N} \\ w_{31} & w_{32} & w_{33} & \cdots & w_{3N} \\ \vdots & \vdots & \vdots & \ddots & \vdots \\ w_{M1} & w_{M2} & w_{M3} & \cdots & w_{MN} \end{bmatrix} \begin{bmatrix} f_1 \\ f_2 \\ f_3 \\ \vdots \\ f_N \end{bmatrix} = \begin{bmatrix} p_1 \\ p_2 \\ p_3 \\ \vdots \\ p_M \end{bmatrix}. \quad (2.26)$$

Matrix methods derive their name from these types of matrix equations ($\vec{w}\vec{f} = \vec{p}$), which in practical applications, often contain large numbers of array elements and can be grossly underdetermined. The lack of a unique solution and the size of the matrices involved can make finding an accurate solution difficult. Successfully solving systems of this type forms the foundation of algebraic tomography. Solutions are typically found using an iterative reconstruction algorithm such as the set of algebraic reconstruction techniques.

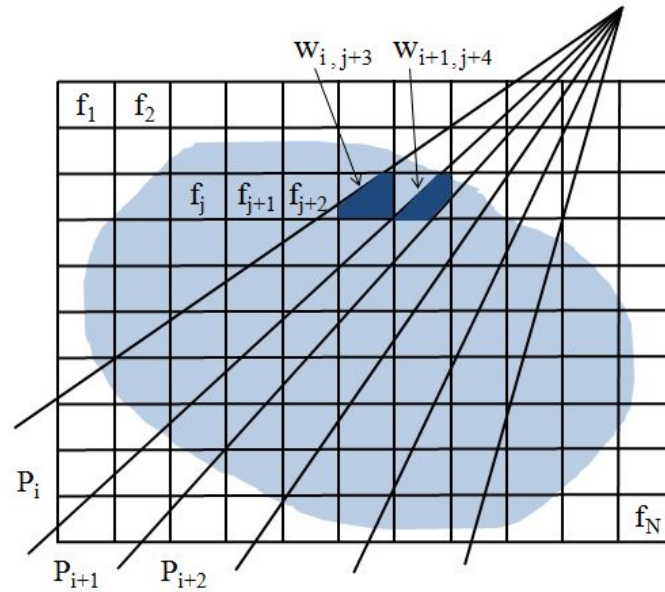


Fig. 2.5. The discretized representation of an imaging region used in matrix methods. This quantized description of projections is adopted when imaging data are sparse and a continuous representation is not sufficiently accurate. Weighting factors are calculated using the area of intersection between each pair of adjacent rays and the pixels in the image grid. Projections are defined as the weighted sum of the contributions of each pixel.

CHAPTER 3

CORRECTION ALGORITHMS

The size, sparsity, and indeterminacy of tomographic matrix equations often prohibits the use of most numerical methods. Techniques commonly applied to solving systems of equations, such as singular value decomposition (SVD), may be capable of processing relatively large or nonsquare matrices, but their functionality declines as the size or ill-conditioning of the problem increases. Matrix equations created by sparse imaging configurations typically require sophisticated correction algorithms to solve. The weighting matrix, for example, encountered during the AIM research consisted of 14,478 columns and 1,905 rows, a ratio of 7.6. Of the 27,580,590 resulting elements, 27,388,172 (99.3%) were zero and only 192,418 were nonzero. This is due to the fact that a single projection only passes through a small percentage of the pixels in the imaging region. The exposure frequency of the CIPS cameras onboard the AIM satellite only allowed for five different views of the PMC layer and at no time did the angular coverage of the rays exceed 63.4° from the vertical. This is in contrast to medical CT, which allows for full 360° angular coverage and thousands of different views. The airglow research only utilized two cameras and the angular coverage never exceeded 46.7° from the vertical. The resulting airglow matrix consisted of 9,600 columns and 320 rows, a ratio of 30. Of the 3,072,000 elements, 3,026,768 (98.5%) were zero and only 45,232 were nonzero. These matrices were large, sparse, highly ill-conditioned, and a direct result of the limited imaging configurations involved in the AIM and airglow research. The angular coverage and number of viewing positions were restricted and the data were only collected from one side of the imaging region. Each of these features complicated the reconstruction process.

3.1. The Kaczmarz Method

Highly-underdetermined tomographic inversion problems are often solved using correction

algorithms. These are iterative techniques in which an assumed structure is gradually improved upon through successive iterations, which approach some approximate solution to a linear system. Most modern correction algorithms and a significant number of imaging technologies rely on this process. The mathematical foundation of these algorithms is derived from the work of Polish mathematician Stefan Kaczmarz [23]. The Kaczmarz method was developed in 1937 for solving large systems of equations and was rediscovered for biomedical imaging in 1970 by Gordon, Bender, and Herman [3].

The method states that given a real or complex $m \times n$ matrix A and a real or complex vector b , an approximate solution to the system $Ax = b$ can be found using the expression

$$x^{k+1} = x^k + \lambda_k \frac{b_i - \langle a_i, x^k \rangle}{\|a_i\|^2} a_i. \quad (3.1)$$

The iteration value is represented by k and $i = k \bmod m + 1$. The i_{th} row of matrix A is given by a_i and the i_{th} component of vector b by b_i . In this notation $\langle \cdot, \cdot \rangle$ refers to the inner product of two vectors and $\|\cdot\|$ to the euclidian norm of a vector. The formula also includes an adaptive relaxation parameter λ_k , which controls the algorithm's rate of convergence.

The Kaczmarz method is an alternating projection algorithm in which a given point is alternately projected onto the hyperplanes defined by the system of equations. Methods of this type are often known as projection onto convex sets (POCS) algorithms. This process is illustrated in Fig. 3.1 for a 2×2 system and demonstrates the concept of an iterative solution. Suppose that a set of two equations in two variables contains a single unique solution. This system can be represented by two lines intersecting at one point in two-dimensional space as seen in the figure. A point is selected as the initial guess for the solution. The inner product $\langle a_i, x^k \rangle = b_i^c$ serves as a projection operator. The computed value of the vector b_i^c obtained from the initial guess differs from the known value b_i . As a result, the point is projected onto the line (hyperplane) defined by a_i . The process is repeated as the point is successively projected onto the hyperplanes defined by each row

of the matrix A . In the example seen in the figure, the repeated projection of the initial point results in its convergence to an approximate solution, which is equivalent to the exact solution in the limit that the number of projections, becomes infinite. The process is less intuitive for large matrices although it utilizes the same principles.

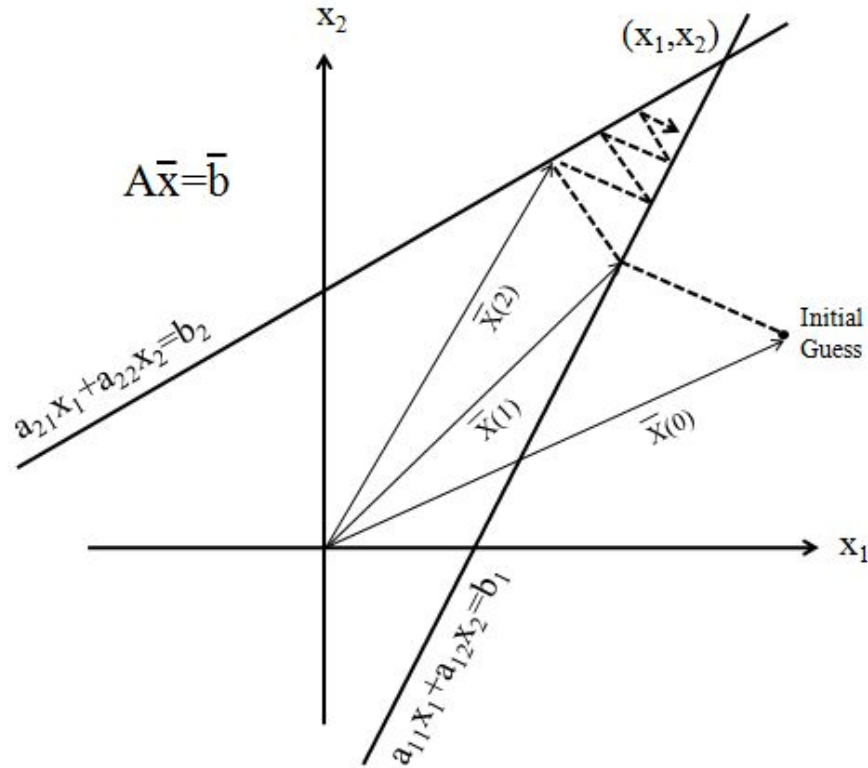


Fig. 3.1. An illustration of the Kaczmarz method for iteratively finding solutions to linear systems of equations. An initial coordinate vector is selected to initialize the algorithm. The vector is then successively projected onto the lines (hyperplanes) defined by the set of equations. If the system is completely determined, the algorithm iteratively converges to the unique solution. The behavior is more complex in higher dimensions and for underdetermined systems, however, the same procedure is followed. The method is used in image reconstruction and is equivalent to the ART algorithm.

When the system is underdetermined a unique solution does not exist and, as a result, the Kaczmarz method cannot converge to a single point. The question naturally arises as to how the algorithm behaves when presented with an infinite number of solutions. Gaarder

and Herman proposed that if an infinite set of solutions exists, the optimal solution is that which exhibits the greatest uniformity [24]. This minimum variance principle suggests that the smoothest solution, which varies the least from the mean value, is the least likely to contain erroneous imaging artifacts. Therefore, it is theoretically more accurate than other solutions. Herman, Lent, and Rowland showed that the Kazcmarz method, which is equivalent to the ART algorithm, converges to the minimum variance solution for an underdetermined system [25]. Variations of this technique have been developed, which minimize properties other than the variance and hence, do not converge to the most uniform solution. Least-squares approaches have been suggested, which minimize the 2-norm of the residual [26]. The conjugate gradient method attempts to minimize a quadratic function given by

$$f(x) = \frac{1}{2}x^T Ax - x^T b, \quad (3.2)$$

which indicates proximity to the solution x . It has also been shown that when inequality constraints are placed on the fundamental ART, the resulting algorithms do not converge to a minimum variance solution as will be discussed further in the following section [25]. Convergence to the smoothest solution is not always ideal and the choice of technique is dependant upon the application. The fundamental ART algorithm, which comprises the Kazcmarz method, is the foundational iterative reconstruction theory and its multiple variations constitute the set of algebraic reconstruction techniques.

3.2. Algebraic Reconstruction Techniques

Despite their differences, the algorithms comprising the set of algebraic reconstruction techniques each follow a similar pattern during their operation. The algorithms are first initialized using an assumed image of the reconstructed object. This information can come from a number of sources and will be discussed further in a subsequent section. The weighting matrix is then used to create a set of projections from the initialized image in a process

called the forward problem. These calculated projections are compared to the measured projections and the resulting difference is then distributed around the image grid using the known weighting factors. Corrections for a given ray are applied to the pixels intersected by that ray, further supporting the need for adequate ray coverage as non-intersected pixels are not updated. This process is repeated for a specified number of iterations, each of which successively improves upon or corrects the existing image. While the iterative nature of correction methods is evident in all of the ART algorithms they do exhibit their own individual properties. Each is designed to function optimally when provided with certain conditions. A number of variations to the fundamental ART algorithm, which belong to the ART class, are presented here and discussed.

The fundamental iterative correction technique is the ART (or Kaczmarz) algorithm. In notation commonly used for image reconstruction, the algorithm (3.1) takes the form [18]

$$\vec{f}^{(i)} = \vec{f}^{(i-1)} - \frac{(\vec{f}^{(i-1)} \cdot \vec{w}_i - p_i)}{\vec{w}_i \cdot \vec{w}_i} \vec{w}_i. \quad (3.3)$$

When ART is applied to an underdetermined system it converges to the most uniform solution. Other solutions may be found by imposing inequality constraints on the algorithm. Though the number of reconstructions, which satisfy the matrix equation may be infinite, restrictions can be placed on the solutions to which the algorithm will converge. In most tomographic applications, negative pixel values are not physically meaningful and thus can be eliminated. Rather than searching for any solution to the $m \times n$ matrix equation, a solution \vec{f} can be sought for which

$$\vec{w}\vec{f} = \vec{p}, \quad (3.4)$$

such that

$$f_i \geq 0, \quad 1 \leq i \leq n. \quad (3.5)$$

This is known as the partially constrained reconstruction problem (PRP). When the ART algorithm is modified to set negative pixel values to zero in search of a solution to PRP, it

is known as the partially constrained algebraic reconstruction technique (PCART). A limit may also be placed on the maximum value of a reconstructed pixel. When the projection data is normalized this maximum value is often set to one. Thus a solution \vec{f} may be sought for which

$$\vec{w}\vec{f} = \vec{p}, \quad (3.6)$$

such that

$$0 \leq f_i \leq 1, \quad 1 \leq i \leq n. \quad (3.7)$$

This is known as the fully constrained reconstruction problem (FRP). When the ART algorithm is modified to constrain values outside of this region to either zero or one, in search of a solution to FRP, it is known as the fully or totally constrained ART (FCART or TCART). It has been shown that PCART and TCART converge to solutions, which satisfy PRP and FRP, respectively, as opposed to the minimum variance solution of ART [25].

Additional modifications to the ART algorithm include simultaneous ART (SART) in which all of the corrections to a pixel value are made simultaneously. This reduces computational run time because the image is produced after only one iteration. It also prevents the propagation of errors, which arise from noise in the measured projection data. A variation of SART exists, which is referred to as the simultaneous iterative reconstruction technique (SIRT). In SIRT the algorithm proceeds as usual, but the corrections are not made until the end of an iteration. The net correction term is calculated as the average of the correction terms for each ray. This process is slower than ART but typically results in more accurate images [18].

Other variations include memory ART in which the minimum and maximum pixel values created during an iteration are stored in a memory matrix. The corresponding pixels are set to either one (maximum) or zero (minimum) and then removed from the solution vector and corresponding matrix column. This is done in an attempt to reduce the size and indeterminacy of the matrix equation. Multiplicative ART (MART) provides updates to ex-

isting pixel values through multiplication by a correction term rather than by the addition of one. The multiplicative factor is simply the ratio between the measured (p_i) and computed (p_i^c) projections and the algorithm is given by

$$\vec{f}^{(i)} = \vec{f}^{(i-1)} \frac{p_i}{p_i^c}. \quad (3.8)$$

The term weighted ART is sometimes used to identify a process in which the area of intersection between a ray and pixel, often used to calculate weighting factors, is replaced by a binary representation. If a ray intersects a pixel the weight is assigned to one, otherwise it is set to zero. This process runs faster than ART, however it often requires more projection data to be accurate. The accuracy of each of these algorithms was tested using synthetic data and it was determined that PCART would be the most appropriate for use in the airglow and AIM research. The images created by the MART algorithm were practically indistinguishable from those generated by PCART and it should be noted that MART would likely have functioned equally well. The accuracy and run times of the algorithms varied, but one common factor found during the testing was that the overall performance of each method significantly improved whenever the initial guess closely resembled the imaging object.

3.3. Initialization

Throughout the course of this research, extensive synthetic testing was conducted in order to further understand the effect initialization had on the performance of the ART algorithms. While the particular behavior caused by each imaging configuration was unique, certain patterns emerged after repeated study. The research was specifically focused on sparse tomography because of the applications to atmospheric and certain biomedical imaging modalities. One characteristic, which was noticed early on in this process, was the dependance of ill-conditioned imaging problems upon an accurate initial guess. The indeterminacy of large sparse matrix equations is well understood and manifested itself in

the techniques used to initialize the reconstruction algorithms. Specifically, if an imaging region was relatively small compared to the number of projections (number of pixels on the order of the number of rays) no initial guess was required. A constant (or empty) initial guess, which assumes no a priori information could be used and the algorithm, was capable of reproducing the object. This property is demonstrated in Fig. 3.2. In contrast, if the imaging region was relatively large (number of pixels on higher order of magnitude than number of rays) the reconstructed object did not localize correctly. This demonstrates that large or ill-conditioned imaging configurations require a priori information in their initialization in order to converge accurately. The imaging configurations used in the presented atmospheric applications were very large and highly sparse. The results of early synthetic testing indicated that a structured (non-constant) initial guess would be required. This led to the discovery of another pattern evident in the behavior of the ART algorithms.

Due to the stratified structure of airglow emission layers and noctilucent clouds, a Gaussian profile was used as an initial guess during the atmospheric research. Synthetic tests performed using a Gaussian initialization revealed another characteristic of the algorithms. The shape, size, and structure of the initial guess were not nearly as important as its altitude. If the vertical location of an initial profile corresponded to that of the imaging object, the algorithm was able to compensate for other deficiencies. The size and sparsity of an imaging problem could be overcome by positioning the Gaussian profile in the correct vertical location. This effect is shown in Fig. 3.3. If the initial Gaussian profile was positioned at the same height as the imaging object, the resulting reconstruction was highly accurate. The size of the grid, the sparsity of the projections, and the horizontal discrepancy in the structure of the imaging object were all compensated for. In contrast if the Gaussian was located at a different height, a smearing effect is seen similar to that of the constant initialization. The reconstruction does not localize and experiences difficulty in recognizing the true location of the object.

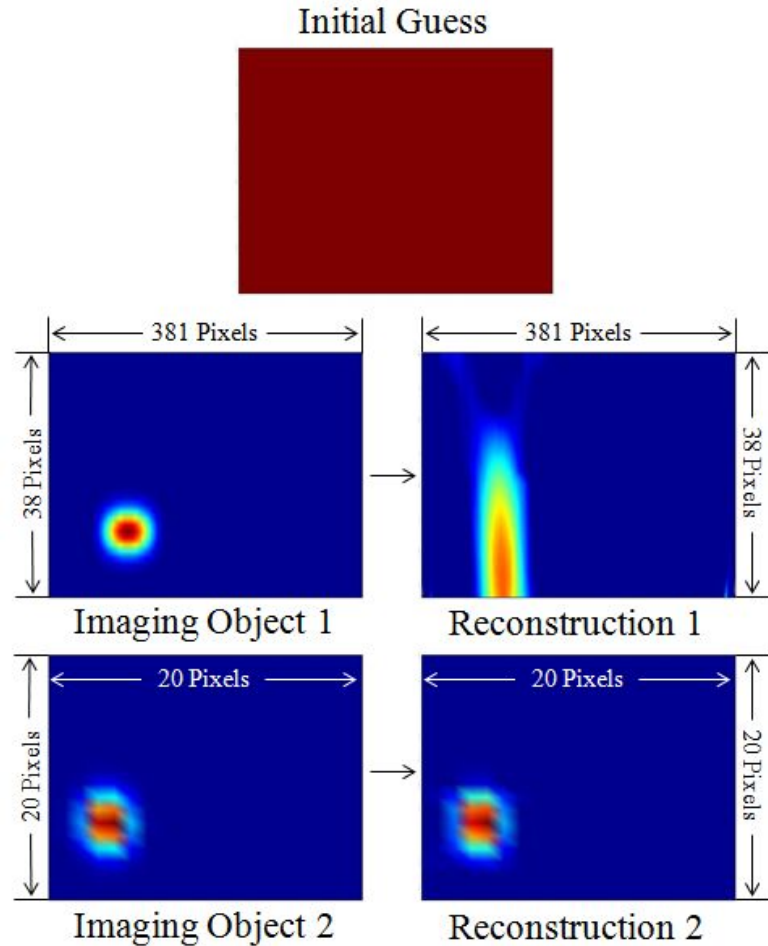


Fig. 3.2. The results of using a constant initial guess for grids of varying size. The algorithm was initialized using a constant background in which each pixel was set to a value of one. An ART algorithm was then used to generate a synthetic reconstruction. For the imaging object consisting of 14478 pixels (upper left), the reconstructed object does not localize correctly (upper right). Conversely the imaging object consisting of 400 pixels (lower left) is reconstructed with considerable accuracy (lower right). This result demonstrates the need for a priori information in the initialization of large or highly sparse imaging configurations.

These results demonstrate that, despite the advanced capabilities of the ART algorithms, highly ill-conditioned inverse problems require a semi-precise initialization in order to converge to an accurate image. This is particularly true for large or sparse imaging grids in which a constant initialization causes the reconstruction to wash out. This technique does, however, show considerable potential for the use of Gaussian profiles in sparse tomogra-

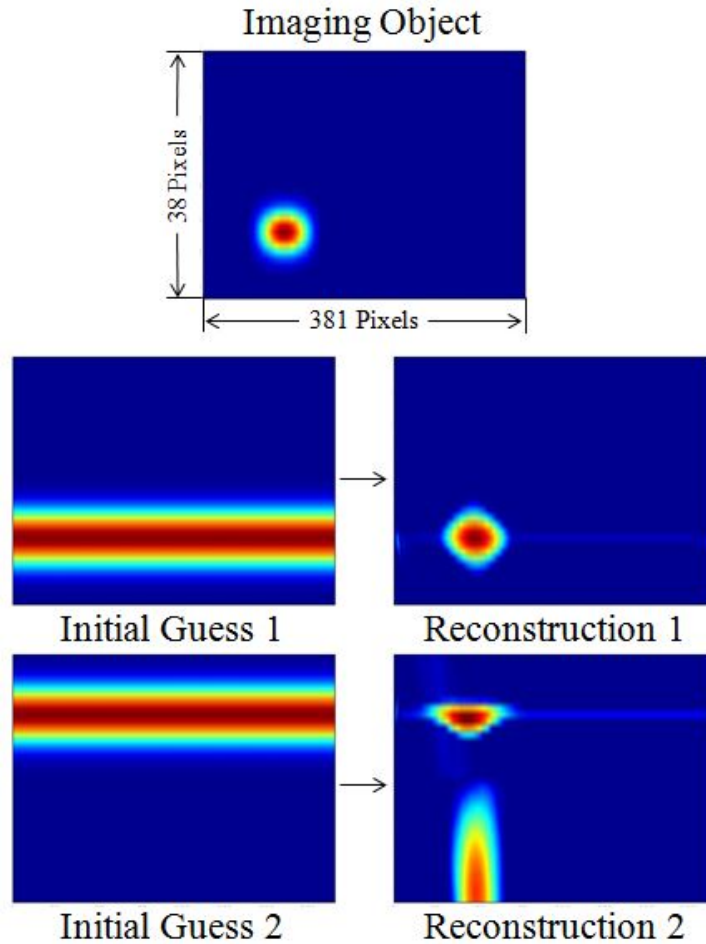


Fig. 3.3. The effect the altitude of an initial profile has on the accuracy of reconstructed images. If the vertical position of an imaging object and corresponding initial profile (upper left) coincided, the algorithm was able to compensate for the size and sparsity of the imaging configuration. The resulting reconstruction was highly accurate (upper right). In contrast if the vertical position of the object differed from that of the initial guess (lower left), the reconstruction (lower right) did not localize well and the accuracy was diminished. This demonstrates the importance and potential of correctly associating an altitude with an initial profile.

phy. Locating the specific position of the imaging object does not appear to be necessary as long as the vertical location is known. In practical applications, there are often a number of approaches that can be used to quantify the height, depth, or altitude of an imaging object within the grid. Triangulation can be performed using supplementary measurements performed by additional imaging instrumentation. The filtered back projections discussed

previously are often used as initial guesses in imaging algorithms. However, they require a large number of measured projections from a wide range of angles in order to be representative of the imaging object. When the data are sparse and collected from only one side, as in the case of the airglow and AIM research, the back projection is far less accurate than other techniques. A layered initialization technique developed during this project is designed to detect the altitude of a structure using a series of reconstructions. The series of initial guesses were located at varying heights and scanned vertically across the imaging grid. The height of the object is then assessed from the response of the reconstructions. This approach is explained further in Appendix A. The initialization of reconstruction algorithms using Gaussian profiles at known altitudes could have significant potential in the field of atmospheric tomography. The technique was applied to tomographic imaging of airglow emissions and noctilucent clouds in the following chapters.

CHAPTER 4

THREE-DIMENSIONAL TOMOGRAPHIC RECONSTRUCTION OF MESOSPHERIC
AIRGLOW STRUCTURES USING TWO-STATION GROUND-BASED IMAGE
MEASUREMENTS¹

A new methodology is presented to create two-dimensional (2D) and three-dimensional (3D) tomographic reconstructions of mesospheric airglow layer structure using two-station all-sky image measurements. A fanning technique is presented, which produces a series of cross sectional 2D reconstructions that are combined to create a 3D mapping of the airglow volume. The imaging configuration is discussed and the inherent challenges of using limited-angle data in tomographic reconstructions have been analyzed through synthetic testing of artificially generated imaging objects. An iterative reconstruction method, the partially constrained algebraic reconstruction technique (PCART), was used in conjunction with a priori information of the airglow emission profile to constrain the height of the imaged region, thereby reducing the indeterminacy of the inverse problem. Synthetic projection data were acquired from the imaging objects and forward problem to validate the tomographic method and to demonstrate the ability of this technique to accurately reconstruct information using only two ground-based sites. Reconstructions of the OH airglow layer were created using data recorded by all-sky CCD cameras located at Bear Lake Observatory, Utah, and at Star Valley, Wyoming, with an optimal site separation of ~ 100 km. The ability to extend powerful 2D and 3D tomographic methods to two-station ground-based measurements offers obvious practical advantages for new measurement programs. The importance and applications of mesospheric tomographic reconstructions in airglow studies, as well as the need for future measurements and continued development of techniques of this type, are discussed.

¹Coauthored by Timothy E. Doyle, Michael J. Taylor, Brent L. Carruth, Pierre-Dominique Pautet, and Yucheng Zhao. Letters permitting the use of coauthored material are included in Appendix D.

4.1. Introduction

Ground-based spectrometric and imaging methods were first developed for studying the aurora and later the fainter airglow emissions. Some of the first scientific measurements of airglow emissions were conducted in the Soviet Union using a spectrograph as early as 1933. Subsequent observations and additional spectrographic measurements were more widely performed in the years that followed [27].

Although ground-based imaging is easily accessible, it inevitably encounters some difficulties arising from the limited angular views available from the ground. Another problem is the amount of background light captured in the images, leading to a noisy signal [28]. This complication is commonly countered by performing measurements at night or occasionally during the twilight hours [29]. A total solar eclipse has also been used to accommodate daytime observation of airglow [30]. The absence of sunlight makes such measurements possible, but further restricts the times when the airglow observations can be made.

As the technology available for airglow measurements improved, many of these restrictions have been reduced or eliminated. The need to observe emissions at night can be negated by conducting observations at higher altitudes [28]. The feasibility of using near-infrared (NIR) cameras onboard high-altitude balloons to study daytime auroral and airglow emissions has also been investigated [31]. In addition to ground-based studies, detailed observations of airglow emissions have now been obtained using sounding rockets, as well as remote sensing satellite measurements [32, 33]. Importantly, auroral brightness measurements have been made from sounding rockets and used to tomographically reconstruct two-dimensional distributions of auroral volume emission rates [34, 35]. Tomographic inversion of the mesospheric airglow layer has also been conducted using satellite-based limb scans [36, 37]. Developments in atmospheric imaging have further aided the study of other phenomena such as ozone [38, 39] and polar mesospheric clouds [40].

Advances made in data acquisition, particularly for space-based measurements, have provided a means for understanding the chemical and physical processes responsible for producing airglow emissions [28]. For example, satellite information has been used for the OI (557.7nm) airglow emission during the early ISIS II mission [41] while a broad dayglow spectrum was obtained from instruments onboard the space shuttle [42]. Significant contributions to the early development of space-based atmospheric imaging were also made by Anger and colleagues who published a series of papers detailing results from the Ultraviolet Imager onboard the Viking Spacecraft [43]. These studies focused on understanding auroral dynamics while more recent studies using the OSIRIS instrument onboard the Odin spacecraft have investigated the airglow emissions and have included tomographic techniques [44–46].

While advanced techniques provide novel opportunities for observing the airglow layer, they often lack the accessibility of ground-based measurements. Technological advances have eliminated most of the difficulties associated with observing airglow from the ground [47]. The application of tomography methods in atmospheric science is proving to be a powerful tool for investigating structure and dynamics of airglow emissions using relatively sparse image data. On this note, Nygrén, Markkanen, Lehtinen, and Kaila examined the use of a stochastic inversion algorithm for reconstructing 2D tomographic images of aurora using two cameras separated by 200km [48]. Due to the large distance between the sites, reconstructions were only obtained from an area close to one of the sites. This technique was later applied to 2D tomographic reconstructions of gravity wave structure in the OH airglow layer; the study was, however, limited to simulated reconstructions and a linear chain of five camera sites [49]. A subsequent airglow study compared the performance of a five-camera chain to a two-camera configuration with simulations, and also presented reconstructions from two-camera measurements of the OI (557.7nm) emission layer from Hawaii [50]. However, the large site separation (152km) provided a poor range

of projection angles for reconstruction and it was concluded that three or more stations were necessary to provide reasonably good results. Also, a linear chain of sites could not image specific gravity wave features, such as wave fronts, that are parallel to the chain [50].

Recently, a virtual chain was created by collecting a sequence of all-sky OH images for 2D tomographic imaging using a single camera on an airplane [51]. However, the motion of the aircraft combined with the integration time of the imagers limited the resolution of the data to 8km for an assumed stationary gravity wave. The reconstructions were obtained by performing a least-squares minimization of a weighted vector norm, and were constrained using a vertical envelop function for the airglow layer estimated from the experimental data. In contrast, Semeter and Mendillo conducted simulation studies of tomographic imaging of upper-atmospheric airglow emissions using a nonlinear optimization technique, and constrained the reconstructions using Chapman profiles for the vertical emission profiles [52]. Their work, however, was limited to 2D reconstructions and focused on measurements from a chain of four equally spaced cameras.

Although significant progress has been achieved in airglow tomography with three or more stations, considerably less progress has been reported for advancing the possibilities of two-station tomography [48, 50]. This paper examines the capabilities and potential of using sparse ground-based imaging measurements from only two-stations for tomographic studies of the airglow emission structures. The abilities of two-station data are demonstrated using both synthetically created imaging objects (modeled data) and OH airglow data. For modeled data, synthetic projections are created from the object and used to create a reconstruction. The synthetic reconstruction was then compared to the original object in order to validate the tomography methods and algorithms. The working hypothesis for this research was that two viewing stations are sufficient for creating accurate tomographic reconstructions when provided with a priori knowledge of the layer's vertical distribution. The typical extent or thickness of this layer was provided by altitude studies of hydroxyl

(OH) airglow using rocket measurements and suggested a layer thickness of 8.6 ± 3.1 km [53], as well as recent measurements of the OH emission layer made by the SABER instrument onboard NASA's TIMED satellite. This value is sufficiently larger than the resolution of our cameras at mesospheric altitudes, which allows for the delineation of fine vertical structure in the images. The ability to resolve vertical variations is of significant interest to mesospheric studies because of its relevance to the propagation of gravity waves and the formation of certain cloud layers [54].

Images of the OH airglow layer were reconstructed using the PCART algorithm from data recorded by all-sky CCD cameras located at the Bear Lake and Star Valley observatories, operated by the airglow group at Utah State University (USU). These reconstructions were generated using projection data measured along linear profiles common to images obtained at each viewing site. A novel 3D fanning technique was developed, which combines multiple 2D reconstructions to form a 3D mapping of the OH airglow structure from which detailed investigations of the thickness, height, and internal structure of the layer were possible. The results presented here promote the use of 3D tomographic imaging capabilities, using two-station arrays optimized for airglow emissions, to investigate mesospheric gravity wave structure and propagation in unprecedented detail. The technique may also require less computational run time than conventional 3D tomography as it eliminates the need to compute volumes of intersections between rays and voxels. The accuracy and applicability of this technique is a topic of ongoing research.

4.2. Methods

4.2.1. Imaging Configuration

A number of parameters affect the choice of location for ground-based imaging instrumentation. Although proximity provides researchers with greater accessibility to equipment, ambient light pollution often necessitates the placement of imaging systems in sparsely

populated areas. While methods exist, which can account for background noise in atmospheric imaging [55], the limited nature of two-station data is further complicated by such inclusions.

The objective of this project was to test the capability of tomographically reconstructing airglow emission data collected from only two viewing stations. The locations of the two stations were therefore optimized to ensure that the data were of the highest quality possible to create accurate reconstructions. Several low-population areas are in close proximity to the USU campus in Logan, Utah. The university-owned Bear Lake Observatory (BLO) was a prime location for one of the all-sky CCD cameras used to acquire the airglow measurements. The BLO is located on a mountainside a few miles west of Bear Lake, Utah, (41.95° N 111.49° W) and provided a superior night-sky viewing capability.

The viewing conditions of the two sites needed to be as similar as possible so that simultaneous observations of events could provide consistent data from each location. In addition to this requirement, the distance between the two cameras is important for providing a tomographically conducive imaging configuration. In order to provide sufficient angular coverage, the distance between the two viewing stations should be on the same order of magnitude as the height of the OH airglow emission layer. As described in the introduction measurements of median OH layer altitudes have been conducted using a number of remote-sensing techniques including rockets, satellites, and ground-based imaging systems in which volume emission profiles were estimated using tomographic techniques [53, 56, 57]. These measurements suggest a mean altitude of 87 ± 3.0 km for the OH M band [53, 58]. A search for a suitable site for the second camera identified Afton, Wyoming, which is located ~ 100 km almost due north of BLO. A mobile observatory was constructed and located on the playing field of Afton's Star Valley High School (42.74° N 110.95° W), which was located at a similar altitude to BLO and provided good viewing conditions. This second station is hereafter referred to as the Star Valley Observatory (SVO).

An all-sky imager was operated at each site during the winter period of 2009-10. Each imager utilized a sensitive back-thinned 1024x1024-pixel CCD of high quantum efficiency ($\sim 80\%$ at visible, 50% at NIR wavelengths) to measure the mesospheric NIR OH Meinel broad band emission (710-930nm). The large dynamic range and low noise characteristics (dark current $< 0.5 \text{ e}^-/\text{pixel}/\text{sec}$) of these devices provided an exceptional capability for quantitative measurements of faint, low contrast ($< 5\%$) gravity waves. The exposure time for each camera, synchronized using GPS, was 15 seconds with an image acquired every 30 seconds. The data were 2x2 binned on the chip, down to 512x512 pixels, resulting in a zenith horizontal resolution of $\sim 0.5\text{km}$ suitable for short-period gravity wave measurements [59].

Figure 4.1 is an example of two coincident CCD images recorded from BLO and SVO on the night of February 15, 2009 at 07:51:32 UT. The displacement of prominent wave structures in these two images is evident. The images were calibrated using the known star background to accurately determine each camera's orientation and pixel scale size. They were then filtered to remove stars and unwarped to correct for the all-sky observing geometry and projected onto a rectangular geographical grid of dimensions 256x256km for an assumed OH emission altitude of 87km [60,61]. A time sequence of these images at 7.5 minute intervals is shown in Fig. 4.2 illustrating the coherent motion of the wave structures. The top two images were used to create the airglow reconstructions presented in this paper.

To process these data for tomographic reconstruction, simultaneous image pairs were geographically aligned and then overlapped creating a common measurement area as shown in Fig. 4.3. From these composite images, projection data were calculated, which represented the intensity of the emissions measured at a given angle for each viewing location. These data constituted the tomographic projections used to create the airglow reconstructions. The yellow line in the figure represents the emission profile common to both images from which the projection data were extracted as described below.

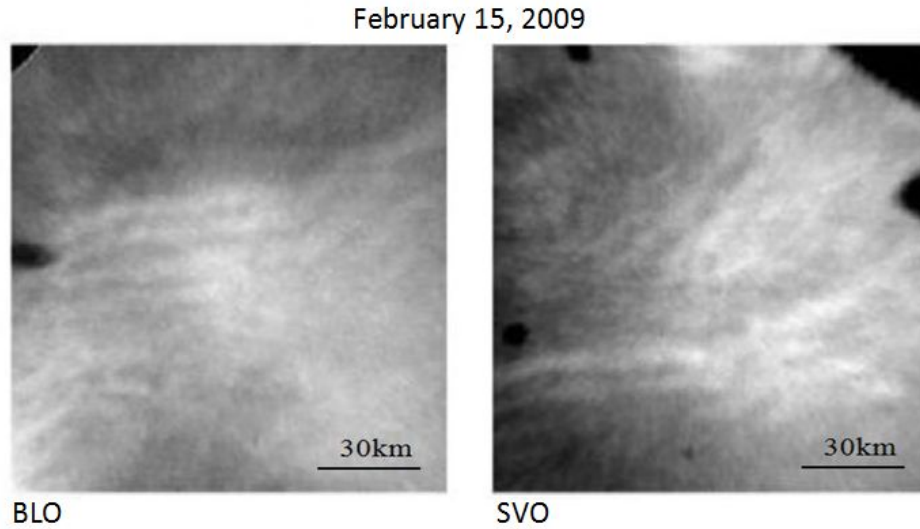


Fig. 4.1. Synchronous OH airglow images from BLO and SVO recorded on February 15, 2009 at 07:51:32 UT showing gravity wave structures. Images have been flat-fielded and processed to remove the star background and projected onto a 256x256km grid.

Once the projection data were extracted from the common imaging profile, large-scale intensity fluctuations were filtered out to compensate for light from non-airglow sources and any differences in the spatial responses of the two cameras. Figure 4.4 shows this process. The upper two plots show the OH signal with fitted background curves, which were used to remove the large-scale amplitude variations. The lower plot shows the resultant excellent agreement between the relative intensities of the BLO and SVO data. The similarity of the relative magnitudes of projection data acquired at each imaging location is an important element of creating accurate tomographic reconstructions.

4.2.2. Tomographic Theory

Large-scale tomographic measurements, such as the airglow measurements described here, are often naturally limited in their range of viewing angles resulting in a sparse ray distribution. This limitation creates an ill-conditioned inverse problem, which is most appropriately solved using a class of reconstruction algorithms known as matrix methods. This is in contrast to the set of transform methods in which the object to be reconstructed

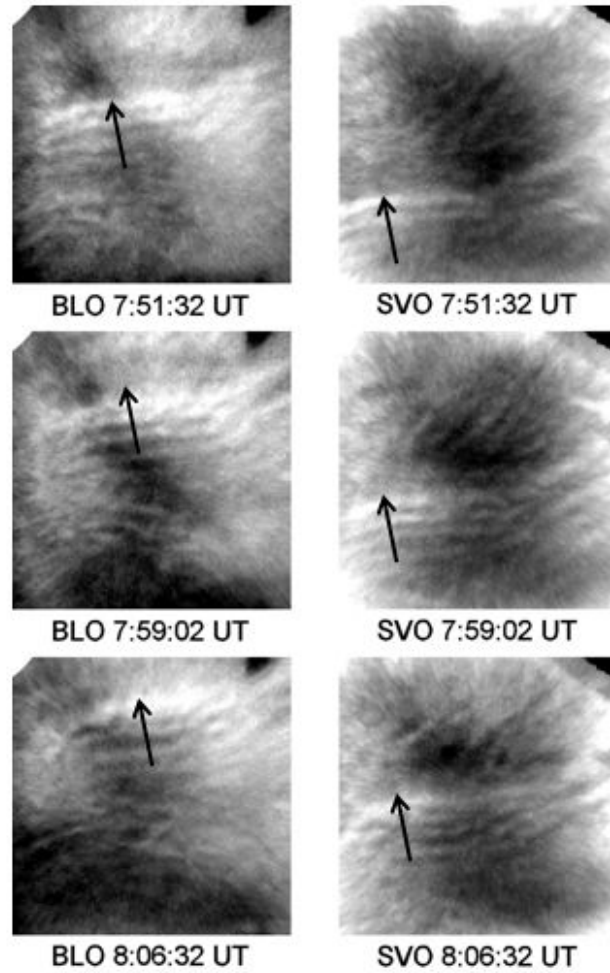


Fig. 4.2. Time sequence of OH airglow images from the BLO (left) and SVO (right) with a 7.5 minute difference between successive images illustrating coherent wave motion (indicated by arrows). The top two images were used for the tomographic reconstructions in this article.

can be approximated as continuous because of the dense ray distribution (e.g. medical imaging). With matrix methods, the low density of the projected rays necessitates the use of a quantized representation for the imaged object. The assumed continuity of the imaged object and its projections is therefore replaced by a discretized description. The grid overlayed on the imaged object is also given a discontinuous structure through division into pixels. The quantization of the imaging object and its projections gives rise to a linear (algebraic) description and a matrix formalism.

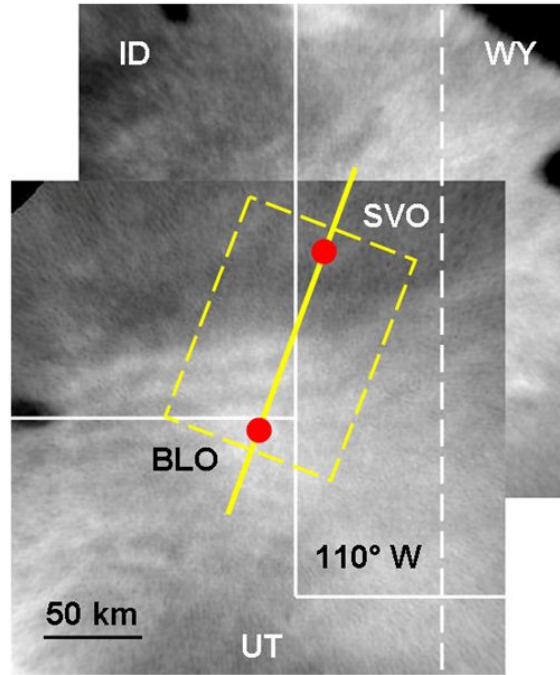


Fig. 4.3. An example of the overlapping technique used to align simultaneous images from BLO and SVO. The yellow line represents a common imaging profile from which projection data were extracted and used to create tomographic reconstructions of the OH structures.

The projection of a ray through a pixel is given by the direct relationship:

$$p = wf. \quad (4.1)$$

The single pixel projection p is equal to the product of the weighting factor w and the functional pixel value f . The weighting factor expresses the area of the pixel, which is intersected by the ray. This convention is shown in Fig. 4.5. The weight $w_{m,n}$ of the n_{th} pixel in the m_{th} projection is defined as the area of intersection between the pixel and the two rays (lines) constituting the projection. This common area is represented by the red shaded regions in the diagram. The total projection p_m is given by the sum of the weights of each intersected pixel.

The total measured signal along a given angle resulting from the ray's interaction with N pixels can be expressed as the sum:

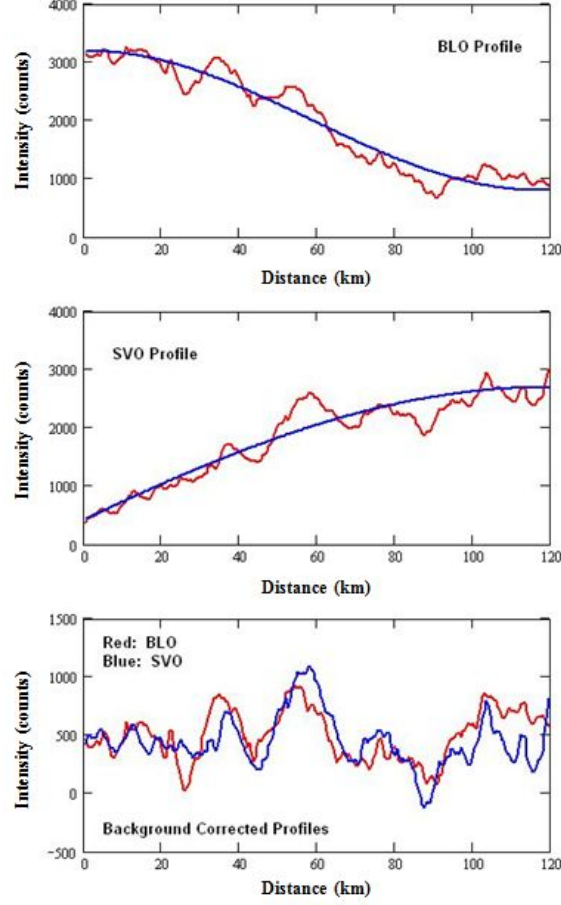


Fig. 4.4. Plots of OH emission brightness for BLO (top) and SVO (center) along a common 120km profile (indicated by the yellow line in Fig. 4.1). The fitted background curve were used to remove large-scale brightness variations across these profiles. The bottom image demonstrates the excellent agreement between the two intensity profiles once these variations are removed.

$$p = \sum_{n=1}^N w_n f_n. \quad (4.2)$$

In matrix methods, as used here, the number of constructed rays from a given site is finite and the projection of the m_{th} ray through the imaging region is given by:

$$p_m = \sum_{n=1}^N w_{m,n} f_n. \quad (4.3)$$

These projected rays constitute a vector, which contains the combined contribution of each pixel. The resulting system of equations can be expressed as the following matrix:

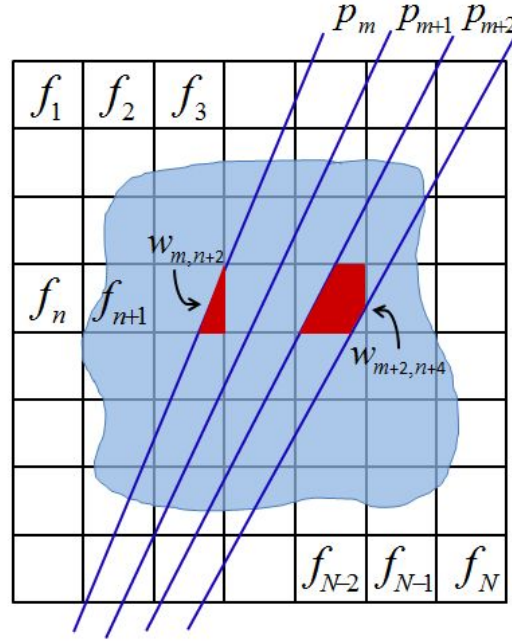


Fig. 4.5. An illustration of the discretized imaging region used in algebraic tomography. The contribution of a given pixel to a measured projection is defined by the weighting factor w represented by the shaded region showing the intersection of a ray with a pixel. The lightly shaded region represents the imaging object.

$$\begin{bmatrix} w_{11} & w_{12} & w_{13} & \cdots & w_{1N} \\ w_{21} & w_{22} & w_{23} & \cdots & w_{2N} \\ w_{31} & w_{32} & w_{33} & \cdots & w_{3N} \\ \vdots & \vdots & \vdots & \ddots & \vdots \\ w_{M1} & w_{M2} & w_{M3} & \cdots & w_{MN} \end{bmatrix} \begin{bmatrix} f_1 \\ f_2 \\ f_3 \\ \vdots \\ f_N \end{bmatrix} = \begin{bmatrix} p_1 \\ p_2 \\ p_3 \\ \vdots \\ p_M \end{bmatrix}. \quad (4.4)$$

This matrix equation, $\overline{W}\mathbf{f} = \mathbf{p}$, is in practice difficult to solve. The primary reason for this is that most applications of matrix methods generate underdetermined systems for which no unique solution exists [18]. Additionally, arrays with large numbers of elements can make accurate approximations difficult. Finding sufficiently accurate solutions to this system forms the foundation of algebraic tomography. The most common approach to finding solutions of this system utilizes a set of tomographic methods known as algebraic

reconstruction techniques (ARTs) [18]. ARTs are a set of correction algorithms in which an initial image is gradually improved upon as successive iterations are carried out. An initial approximation of the object's structure (e.g., nominal OH layer profile) is provided to the algorithm as a vector and a correction factor is repetitively added. This correction term is calculated by comparing the tomographic projections of the previous image in the iteration with the measured projections. The way in which this correction term is computed defines the reconstruction technique used here.

The fundamental algorithm upon which the set of ARTs is based is called the algebraic reconstruction technique (ART). Subsequent modifications to this technique have been developed, which are designed for optimizing certain aspects of the data in order to create more accurate reconstructions. Among them are the constrained or totally constrained ART (TCART), the multiplicative ART (MART), the simultaneous iterative technique (SIRT), the simultaneous ART (SART), and the memory ART [18]. Using both synthetic and measured data, these and other algorithms were tested and assessed on the basis of their ability to accurately reconstruct airglow-like images from limited tomographic projection data. The testing determined that the partially constrained algebraic reconstruction technique (PCART) provided accurate and reliable reconstruction capabilities for our two-station imaging configuration. However, reconstructions formed using the MART algorithm were essentially indistinguishable from the PCART results described here.

The correction algorithm for PCART is:

$$f_{m,n} = f_{m-1,n} + \lambda \frac{(p_m - p_m^i)w_{m,n}}{N_m}, \quad (4.5)$$

where $f_{m,n}$ is the discrete value of the reconstructed image for the m th ray and the n th pixel. While this expression is given in a matrix-vector form conducive to imaging, it is equivalent to the Kaczmarz method (Eqs. (3.1) and (3.3)). The addition of a correction factor to previous image values, $f_{m-1,n}$, provides the iterative step for this iterative reconstruction technique. The elements of the weighting matrix are given by $w_{m,n}$ and the convergence of

the corrections can be controlled by the relaxation parameter λ . The measured projections correspond to p_m and the computed projections to p_m^i . The N_m term in the denominator is the total weight of the m th ray and can be expressed as the sum of each individual weighting factor for the N pixels in the imaging area:

$$N_m = \sum_{n=1}^N w_{m,n}. \quad (4.6)$$

The initial value of f can also have a significant impact on the convergence of iterative algorithms. This basis value, sometimes called the initial guess, was found to be of critical importance to the synthetic testing and method validation used for this project. Varying initial guesses were used in combination with specific artificial imaging objects in order to test the influence of the initial guess on the converged image. This synthetic testing provided an important means of validation for the algorithms used to reconstruct the airglow emission structure.

4.3. Results

The results of this study are divided into two parts using synthetic and measured data. The synthetic data are first discussed as a means of validating the PCART tomographic method used here. OH data and their corresponding reconstructions are then presented to demonstrate the capability of this technique for future airglow imaging studies.

4.3.1. Synthetic Data and Validation

Synthetic imaging objects were generated by artificially specifying the values of f corresponding to a terminal iteration value. The weighting matrix was then utilized in a forward modeling approach to create synthetic projections of the artificial object. These synthetic projections were then processed by the tomographic (inverse) algorithm to generate reconstructed images. The validity of these images was assessed by comparison with the original artificial imaging objects. Through successive testing, an understanding of the

behavior of the reconstruction algorithm under conditions appropriate to the airglow measurements was achieved. The combination of these assessments provided a good qualitative assessment of the accuracy of the tomographic algorithm. Confidence in the reconstructions was obtained through synthetic testing of artificial imaging objects, which closely resembled the airglow structure. In this study, typical synthetic objects were constructed using a vertical profile and periodic wave structure to simulate gravity waves propagating through the OH layer.

As two-station airglow tomography involves an imaging configuration, which restricts the ray coverage, an assumed vertical profile or some other form of height constraint is necessary in the inversion process. This need for an a priori initialization of the correction algorithm has been previously described in the literature. The rocket-based tomography reported by McDade, Lloyd, and Llewellyn as part of the ARIES campaign included a careful selection of pixel elements, which were allowed to contribute to line-of-sight brightness measurements. The imaging region was restricted to a rectangular grid, which conservatively enclosed the primary auroral form as determined separately from ground-based observations [35]. Similarly, Semeter and Mendillo regularized the ill-posed tomographic problem of reconstructing atmospheric emissions observed from the ground by constraining the vertical profile to a Chapman function. The resulting nonlinear optimization problem was minimized and used as the initial guess in a MART algorithm [52]. Of particular relevance to our OH airglow study, Anderson, Kamalabadi, and Swenson used a Gaussian function as the vertical profile for their atmospheric gravity wave (AGW) parameter estimation method [62].

During the synthetic testing, the algorithm's independence from ray geometries and sensitivity to various vertical profiles were examined. The effects of different ray-tracing geometries on the PCART algorithm was performed using a range of imaging grids that were varied independently between the forward problem (synthetic data) and inverse prob-

lem (tomographic reconstructions). For example the synthetic object shown at the top of Fig. 4.6 was generated using a 50x200-pixel grid. This differs from the 60x160-pixel grid used in the three reconstructed images shown in the figure (bottom). The algorithm's ability to reconstruct the object when provided with a different projection matrix, resulting from varied ray coverage, demonstrates a robustness, which provides confidence in the tomographic algorithm and the Gaussian initialization.

As part of the synthetic testing, various vertical profiles were used to initialize the reconstruction algorithm in order to study its behavior. These distributions were characterized by their width (Γ), vertical position (μ), and maximum value (P^m). Three of which are described as follows. The square or constant profile (Fig. 4.7 upper panel) is defined by

$$P_S(z) = \begin{cases} P_S^m & \text{if } \mu - \frac{\Gamma}{2} < z < \mu + \frac{\Gamma}{2} \\ 0 & \text{otherwise,} \end{cases} \quad (4.7)$$

which is the simplest assumption and includes the least a priori information. The maximum value (P^m) is not unique to any single altitude. The value of μ is the center of the distribution as opposed to a maximum or peak value.

A common asymmetric profile frequently encountered in aeronomy is the Chapman function. It is defined by [52]

$$P_C(z) = P_C^m e^{\frac{1}{2}(1-\tilde{z}-e^{-\tilde{z}})}, \quad (4.8)$$

where

$$\tilde{z} = \frac{z - \mu}{\Gamma}. \quad (4.9)$$

The Chapman profile can be seen in Fig. 4.7. Due to asymmetry, the value of μ defines the altitude of the maximum emission rate as opposed to the function centroid. The characteristic width (Γ) is less intuitive in this case. However, it is analogous to the parameterized width of a Gaussian defined by:

$$P_G(z) = P_G^m e^{-\frac{(z-\mu)^2}{\Gamma}}. \quad (4.10)$$

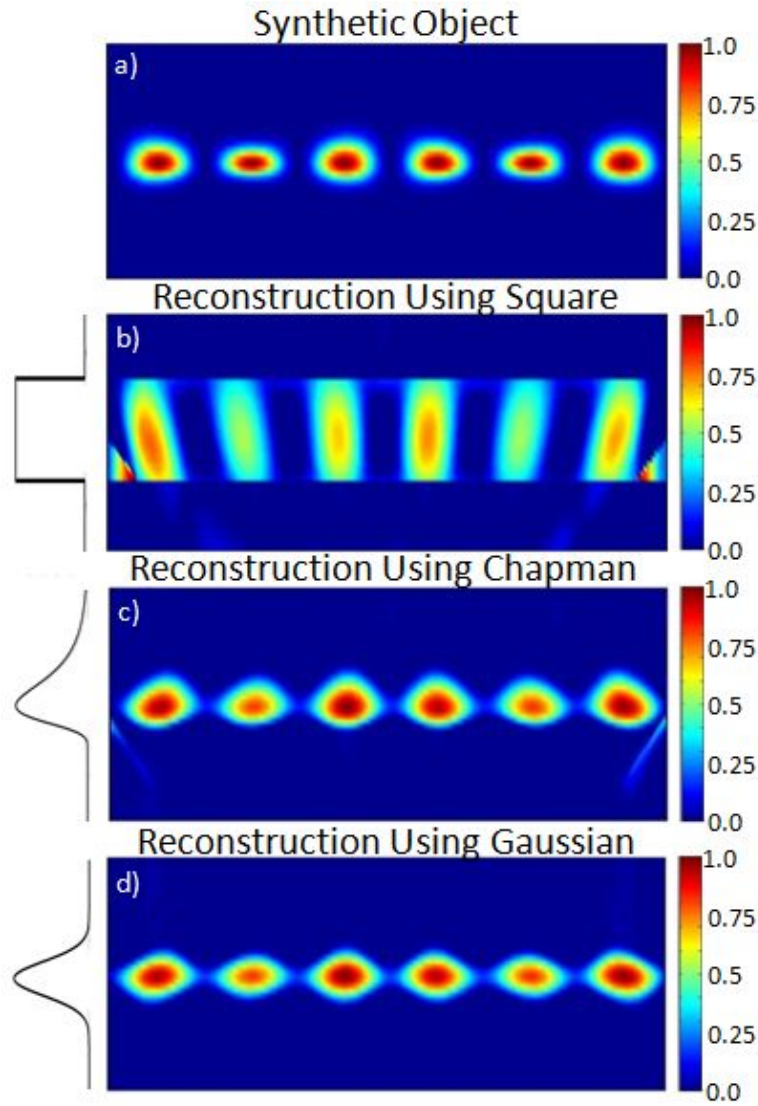


Fig. 4.6. The reconstructed results of synthetic testing performed using the three initial profiles shown in Fig. 4.7. The synthetic object (a) was designed to include asymmetries and height variation in order to test the robustness of the algorithm and compare initial guesses. The reconstructions resulting from square (b), Chapman (c), and Gaussian (d) initializations are shown.

The Gaussian profile (Fig. 4.7) has been used in prior studies to represent the stratified form of cloud or emission layers in atmospheric imaging [62]. It is simpler than the Chapman function and is symmetric. These three functions were used to initialize the reconstruction algorithm during synthetic testing.

Figure 4.6 shows one example of an artificial airglow imaging object representing a vertical cross-section through several wave crests. The three profiles discussed above were used to initialize the algorithm in an attempt to reconstruct the artificial object. The resulting reconstructions are also shown in Fig. 4.6. The use of a square initial guess prevents the reconstruction from localizing and a broader square initialization causes it to wash out completely. Using this imaging configuration, there is not enough projection data to reconstruct an image without the use of a height constraint. In contrast, the accuracy of the reconstruction using the Gaussian and Chapman profiles is evident in both cases (Fig. 4.6). Minor effects and artifacts are visible, but the overall integrity of the reconstructed images is apparent. The reconstructions are shown for 20 iterations, by which point the value of the sum of each pixel in the image changed by less than 1% during an iteration.

A more detailed comparison between the reconstructions using the Gaussian and Chapman profiles shows that although the Chapman initialization contains more information on the layer's assumed vertical profile, it did not significantly alter the resulting structure along the bottom edge. Asymmetries and height variations were also included in the synthetic object to test the capabilities of the Chapman function, as well as the performance of a symmetric Gaussian, under these same conditions. The Gaussian initialization proved capable of reconstructing these asymmetric objects while the Chapman profile caused some distortion along the top edge and exhibited a higher occurrence of imaging artifacts. Furthermore, the use of a slightly wider Gaussian (as much as twice the width of the synthetic object) did not significantly alter the reconstructions.

The choice of a Gaussian structure in simulating airglow layer emission profiles is also supported by previous ground-based measurements using combinations of Na lidar, radar, imaging, and interferometric measurements of different airglow layers [58, 62, 63]. Additional support is provided by the SABER instrument onboard NASA's TIMED satellite. SABER was designed to measure the vertical distribution of infrared radiation emitted by

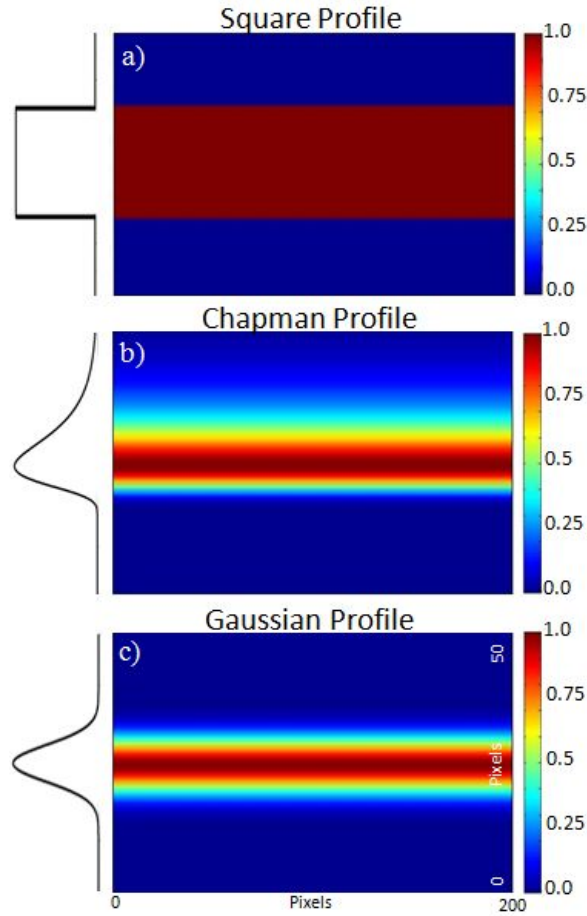


Fig. 4.7. Three of the profiles used to initialize the reconstruction algorithm during synthetic testing. The square (top), Chapman (center), and Gaussian (bottom) profiles are shown along with their vertical cross-sections (left).

various atmospheric gases. The graph in Fig. 4.8 displays an average volume emission rate (VER) for the $1.64\mu\text{m}$ band (channel 9) as a function of altitude. These data comprise an average of 35 nighttime measurements made as the satellite passed within 10° longitude and 10° latitude of BLO in February of 2009, spanning the time period when the tomographic measurements were made. The average OH VER exhibits a Gaussian-like response with a peak emission altitude of 87.3km and a FWHM of 9.8km, in good agreement with previous OH emission measurements [53]. This channel is dominated by the OH (4,2) and (5,3) band emissions, which typically originate at a slightly lower peak altitude (approx-

imately 1.5km) than the broad-band (710-930nm) OH emissions, primarily the OH (6,2) and (7,3) bands, imaged by both cameras [64].

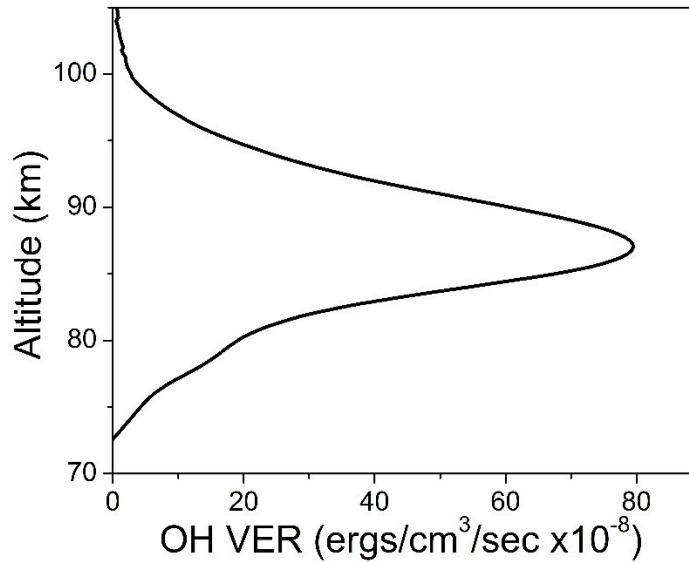


Fig. 4.8. An average volume emission rate (VER) profile of the OH emission determined from SABER observations onboard NASA's TIMED satellite. The data were collected in February of 2009 and correspond to instances when the satellite passed within the vicinity of BLO. The profile exhibits a Gaussian-like shape of FWHM 9.8km and a peak height of 87.3km.

In summary, the simplicity of the Gaussian and its success in reconstructing the synthetic imaging object when compared to more sophisticated (Chapman-like) initializations has made it a natural choice for an initial guess in this study. It also assumes less a priori information than the Chapman profile and has proven to be sufficiently independent of ray configurations. Furthermore, the Gaussian initialization also proved superior to back-projection and other forms of distributive initializations (not discussed here). As accurate tomographic imaging of airglow from a limited number of viewing angles requires the use of a height constraint, a SABER-like Gaussian profile conveniently centered at 85km has been used in the OH airglow reconstructions. This is well within the nominal height range of the OH layer [53].

4.3.2. Airglow Layer Reconstructions

The synthetic testing results support the use of the PCART algorithm for the two-station tomographic airglow study, while the tests conducted using different emission profiles support the use of a symmetric Gaussian and provide confidence that the resulting structures are authentic and not artificially introduced by the initial guess. Emission data were uniformly sampled along a line joining the two camera sites (Fig. 4.3) and processed using the presented tomographic technique to reconstruct a 2D cross-sectional view of the airglow layer and its structure as shown in Fig. 4.9. The reconstruction was made over a height range of 70-100km and a horizontal ground range of 80km using a Gaussian centered at 85km with a FWHM of 10km. The reconstruction yielded information on the airglow layer over the altitude range of 82-88km. As expected, the structured region between the 40 and 80km range coincides with the wave pattern, comprising three main crests evident, near BLO in Fig. 4.3, while the structureless region closer to SVO appears to be thinner. As the upper and lower boundaries of the reconstruction were created by the tomography algorithm and not artificially introduced, they appear to represent significant changes in the bottom-side altitude of the OH layer. Furthermore, several finer wave structures within the vicinity of BLO are also evident in the reconstruction. These are more easily seen in the later images of the time series of Fig. 4.2.

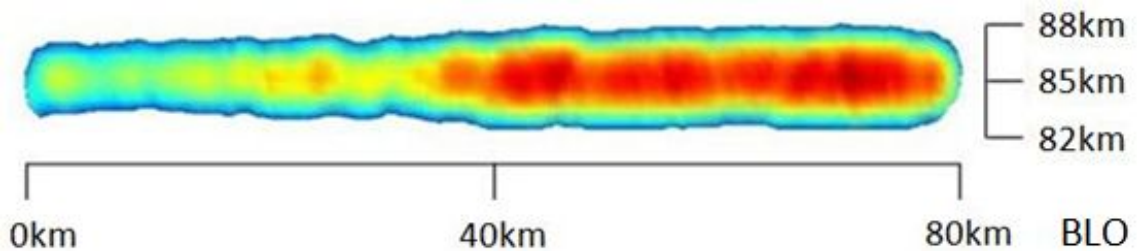


Fig. 4.9. A cross-sectional tomographic reconstruction of the OH layer using data from two ground-based CCD cameras and constrained using a Gaussian profile. Note the change in structure, content, and apparent layer depth along the line joining BLO and SVO.

4.3.3. Three-Dimensional Mapping of Airglow

While a standard 2D reconstruction of the airglow layer provides information on the structure within the zenith plane, it is clearly limited and does not utilize the full 3D imaging volume for quantitative studies of the wave evolution and propagation. To do this, we have developed a novel tomographic fanning technique to create a true 3D mapping of the airglow layer and its structure. In this method, a series of 2D reconstructions are acquired at varying angles away from the zenith plane and combined together to form a 3D reconstruction. This concept is illustrated in Fig. 4.10. The two horizontal planes shown represent the upper and lower boundaries of the tomographic imaging region.

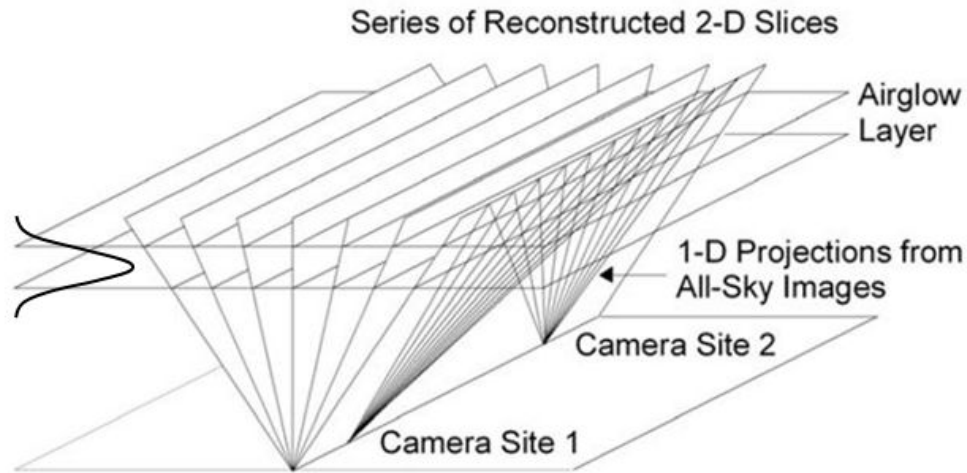


Fig. 4.10. A sketch showing the fanning configuration applied to the airglow data. Images were acquired by all-sky cameras at BLO and SVO (sites 1 and 2 in the figure) and tomographically reconstructed to create a 3D mapping of the OH layer.

Successive 2D reconstructions (totalling 180 slices) were generated at viewing angles incremented at 0.33° (limited by CCD pixel resolution) up to $\pm 30^\circ$ from the zenith. These images were then combined using volume-rendering software to create a 3D mapping of the airglow layer as shown in Fig. 4.11. The spatial extent of the 3D imaging volume is illustrated by the dashed rectangle in Fig. 4.3.

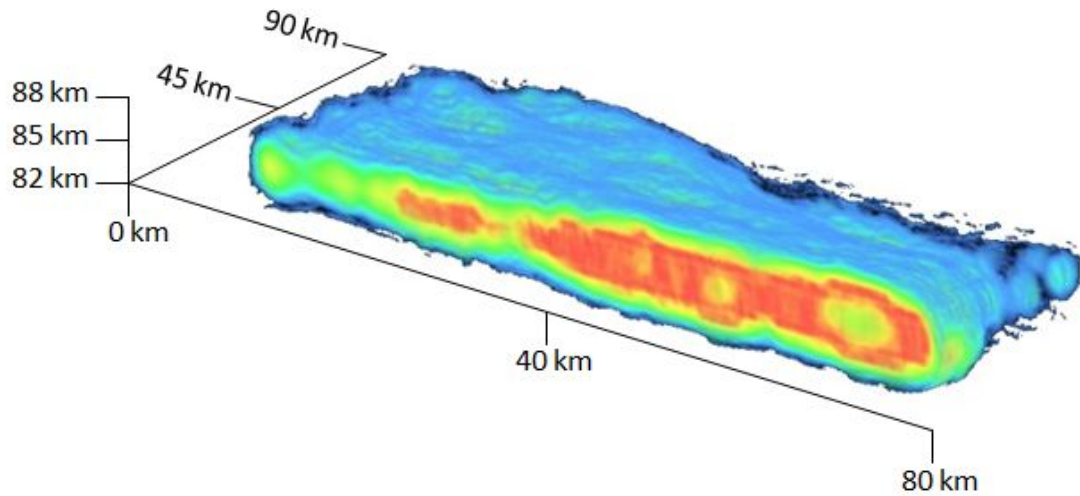


Fig. 4.11. A composite 3D rendering of the airglow layer formed by combining 180 individual 2D reconstructions using the fanning geometry of Fig. 4.10.

The 3D surface provides information about the structure and extent of the wave features, which is not accessible in 2D reconstructions. For example, the three primary wave crests (horizontal wavelength $\sim 20\text{-}30\text{ km}$) are clearly seen extending across the top of the airglow mapping as surface undulations with significant peak-to-peak variations $> 1\text{ km}$. These correspond to the short-period waves seen in Fig. 4.2. Further information can be obtained by slicing the 3D mapping at selected altitudes creating several horizontal 2D cross-sectional segments. An example of this process is presented in Fig. 4.12, which is an expanded view of Fig. 4.11. In this case, the 3D rendering has been divided into six slices, each separated by 1.2 km and spanning the altitude range $82\text{-}88\text{ km}$. The finger-like wave structures are seen in each level, establishing the coherence of the wave throughout the airglow layer. However, the structure in adjacent levels shows significant difference in the fine-scale structures. This new fanning technique clearly provides additional detailed structural information, which is not readily available using current limited tomographic methods applied to atmospheric data.

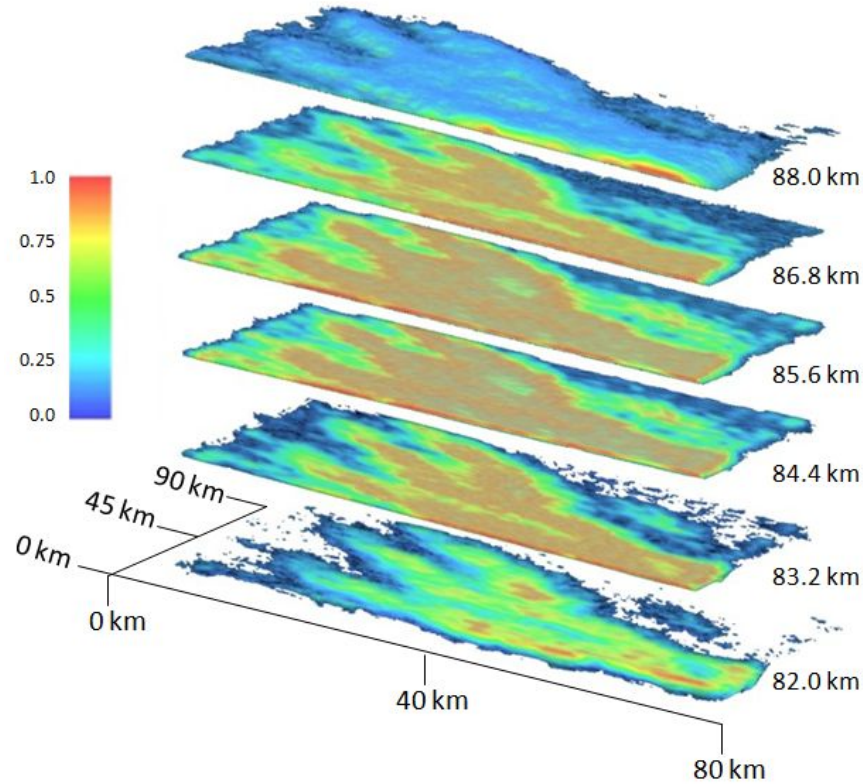


Fig. 4.12. An expanded view of the 3D airglow mapping shown in Fig. 4.11. The 3D rendering has been divided into six horizontal slices, each separated by 1.2km. The ability to observe individual wave-like structures within the airglow layer demonstrates the advantage of using the 3D fanning technique.

4.4. Discussion

The ability to perform detailed tomographic processing of airglow image data from only two stations has major practical advantages. This is because high-quality imaging instrumentation is relatively sparse and the placement and maintenance of three or more such instruments can be logistically difficult. Previously, 3D tomographic reconstruction of the airglow layer was thought to require at least three cameras with one of the sites not in line with the other two [50]. However, it has been demonstrated here that the fanning technique can provide robust 3D reconstructions using data from only two-stations. This was achieved by combining a number of adjacent 2D slices reconstructed from projection

planes that are incrementally tilted from the zenith (Fig. 4.10). The resultant 3D airglow reconstructions exhibited consistent and well-defined variations in layer height, thickness, and internal structure (Figs. 4.11 and 4.12).

This study has been restricted to the development and demonstration of the fanning technique using suitable a priori knowledge of the layer to investigate 3D wave structure in the OH layer. Multiple 3D renderings constructed from time sequences of image pairs would provide important new information on the wave propagation, evolution, and possibly even its dissipation during the course of a night. Frequently more than one wave pattern is observed in the airglow layers (as is evident in the time sequence of Fig. 4.2) and the 3D data can be used to investigate different structures along various angled planes. The potential to view the 3D mapping along specific axes of interest is illustrated in Fig. 4.13, which plots the lower half of Fig. 4.11 along a plane normal to the wave crests (i.e. orthogonal to the direction of the wave propagation). Such data can provide clearer structural information on the individual wave events.

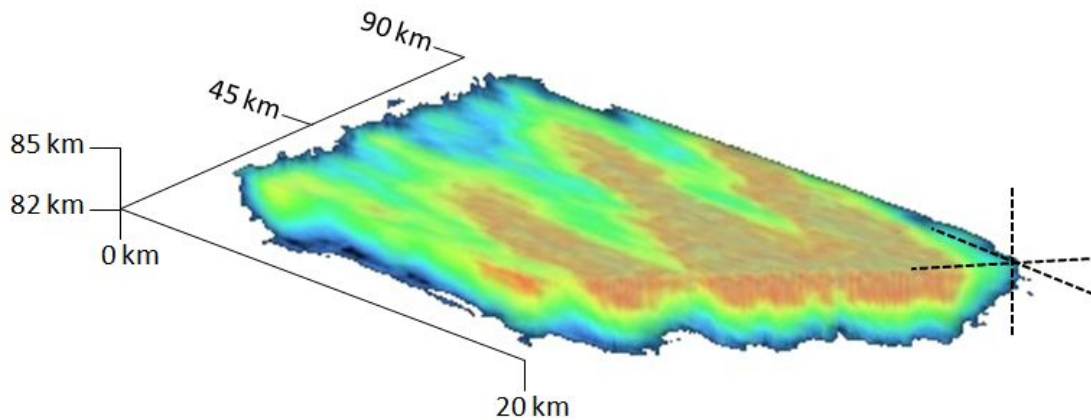


Fig. 4.13. The lower portion of the 3D airglow mapping shown in Fig. 4.11 segmented normal to the wave crests.

Airglow imagery are frequently used to obtain key parameters of the gravity waves in the mesosphere-lower thermosphere (MLT) to define their characteristics and to better un-

derstand how they transfer momentum and generate turbulence at these altitudes [51]. One of these parameters is the intrinsic phase speed of the wave (i.e., speed relative to the background wind field at that altitude). This can be obtained through a knowledge of the wave's vertical and horizontal wave components, which usually requires coincident measurements of the wind field. Alternatively, this information may be obtained directly from the observed pitch angle of the wave front. The ability to acquire 3D reconstructions containing information on the wave tilt significantly broadens the range of information that can be acquired, as well as the types of wave phenomena that can be studied. For example, horizontal variations in the pitch of the wave front can be determined across the wave field over distances significantly larger than the wavelength of short-period, small-scale (5-50km) waves (Figs. 4.11 and 4.12). The structure and dynamics of more complex phenomena can be studied as well, such as mesospheric bore events, which are characterized by sharp leading wave fronts and undular trailing waves that increase in number with time. Additionally, 3D tomography may be used to investigate interfering wave patterns and embedded instabilities called ripples that are associated with gravity wave breaking. The ability to image the scale of these features, as well as to render their 3D structures as they evolve in time, will lead to new and unprecedented models for upper atmospheric dynamics.

Although the studies reported in this paper were limited to only the NIR OH emissions at 87km, they are also applicable to other MLT airglow emission layers such as the Na (589.2nm line centered at 90km), the O₂ (0,1 band at 94km), and the OI (557.7nm green line emission at 96km) [59]. One intriguing possibility is the simultaneous acquisition of tomographic data from several emission bands spanning the 80-100km region of the MLT. Combining the separate emission band reconstructions would extend the vertical range of the tomographic imaging, thereby allowing the observation of phenomena such as the upward or downward propagation of gravity waves or other dynamic phenomena across a wide altitude range.

Finally, the tomographic methods presented in this paper may also be applicable to other upper atmospheric features such as ionospheric F-region airglow, auroral emissions, meteor trails, and polar mesospheric clouds. The ability to collect tomographic data from only two stations is particularly well suited to temporary or campaign-style studies where the cost, availability, or access to equipment is a key issue.

4.5. Conclusion

A new method has been presented for creating 3D tomographic reconstructions of the upper mesospheric OH airglow emission using only two-station image data. Through synthetic testing the potential of the fanning method has been demonstrated. The accuracy of the tomographic reconstructions was greatest with the use of the PCART algorithm in conjunction with a height constraint. When the initialization was assumed to have a Gaussian-like structure, the algorithm proved capable of reconstructing asymmetries present in the imaged object. This a priori knowledge localized the initialization and ensured that it was vertically coincident with the imaging object. This technique is especially well suited to airglow tomography because the altitudes of the MLT emission layers are well measured and relatively stable, especially the OH emission layer [53], with wave-induced changes of only a few kilometers [58]. Opportune satellite measurements of some of these emissions are also currently available (e.g., TIMED satellite). The method was applied to OH airglow data taken by two all-sky cameras located at BLO and SVO with an optimal line-of-sight separation of 100km. Cross sectional reconstructions of the layer structure have been presented and analyzed. Multiple reconstructions from a range of angles measured from the zenith were combined to create a 3D mapping of the airglow layer displaying variations in layer thickness, height, and internal structure. The results presented here support the future use of this method for detailed tomographic studies of MLT structure and dynamics.

CHAPTER 5

TOMOGRAPHIC RECONSTRUCTION OF POLAR MESOSPHERIC CLOUD PROFILES FROM IMAGE DATA COLLECTED DURING THE NASA AIM SATELLITE MISSION¹

Tomographic methods and algorithms used to reconstruct vertical profiles of polar mesospheric clouds (PMCs) from satellite image data are described. The Aeronomy of Ice in the Mesosphere (AIM) satellite was commissioned by NASA to investigate the relationship between the temporal variability of PMCs and changes in the Earth's climate. An overview is given of the geometry of the AIM measurements and the difficulties of using satellite imagery for investigating mesospheric phenomena. A technique which uses a vertical height constraint in the initialization of the inverse problem is presented for overcoming some of these challenges. Synthetically created data by way of the forward problem were used to analyze the effectiveness of the height constraint technique and to validate the tomographic methods used to create the vertical profiles. Examples of reconstructions from the satellite data are presented and interpreted. Since the image data had approximately the same resolution as the PMC thickness, the data were interpolated using a cubic spline to a finer resolution and reconstructed using the same techniques. This was done to allow for clearer delineation of structure and to assess the effect that interpolation had on the vertical profile of the reconstructions. The resulting images demonstrate the potential of using tomographic methods for studying the height variability of the PMC layer and indicate the potential for future analysis of higher resolution data. The importance of tomography to the study of the PMC layer is discussed.

5.1. Introduction

The earliest recorded observations of polar mesospheric clouds (PMCs) were made on

¹Coauthored by Timothy E. Doyle, Michael J. Taylor, Brent L. Carruth, Pierre-Dominique Pautet, and Yucheng Zhao. Letters permitting the use of coauthored material are included in Appendix D.

June 8, 1885 [65]. Their existence was subsequently noted by other observers throughout the summer of that same year [66]. There appears to be no record of their observation prior to 1885. Significant interest was generated at the time of their discovery as a result of triangulation techniques, which predicted a formation altitude of 82km, suggesting the atmosphere extended much further than had previously been believed [67]. The present interest in PMCs is a result of the chronological correlation between their discovery and the global increase of fossil fuel usage, which occurred in the 19th century. It has been suggested that their initial appearance may have been a result of increasing methane (CH_4) levels caused by the industrial revolution [68]. Methane oxidizes to form H_2O in the stratosphere and an increase in CH_4 would lead to an increase of water vapor in the upper atmosphere, promoting PMC growth [69]. Although variations in the occurrence frequency of PMCs have been observed, long-term (28 yr.) trends show an increase ranging from 7-20% per decade depending on latitude [70]. The study of PMCs is therefore of great interest to atmospheric science as their occurrence frequency could act as an indicator of global climate change.

The formation of PMCs has been the topic of considerable investigation and several theories have been developed since their discovery. The earliest of these theories suggested that their formation was caused by volcanism [71]. Thomas gives a thorough description of the historical development of PMC studies and notes that subsequent hypotheses pertaining to their formation included cosmic dust and water-ice nucleation models [67]. Data collected by the Halogen Occultation Experiment (HALOE) support the existence of water-ice crystals as the primary component of PMCs [69].

In addition to their composition and formation, the dynamics of PMCs is of great interest to the study of global climate change. Observations made by the Student Nitric Oxide Explorer (SNOE) suggest the occurrence frequency is strongly influenced by dynamic mesospheric processes [72]. A desire to better understand the structure, extent, occurrence, and evolution of PMCs has led to several experiments designed to image the PMC layer.

Ground-based imaging techniques were the first to be utilized in PMC studies and date back to initial triangulation measurements, which were simultaneously conducted in Russia and Germany in 1896 [73]. The development of lidar [74], radar [75], and other technologies have helped to advance imaging methods for use in atmospheric studies. Despite these advances, the use of ground-based imaging of PMCs is inherently restricted to a relatively small geographic range. Although observations have been reported as low as 42° N latitude [76], they are typically limited to within 50° latitude from either the North or South Pole with an ideal observation range of 53 - 57° north or south and 5 weeks before or after the summer solstice [67]. This restriction limits accessibility, which is the primary advantage of ground-based techniques in comparison to airborne or satellite imaging methods.

While major advances have been made in ground-based imaging techniques, opportunities are currently being provided by space-based imaging experiments, which are simply not available by any other means. High-altitude balloons are common in atmospheric studies, but have not been used extensively in PMC research as the altitude of the mesosphere prevents the possibility of *in situ* balloon measurements [77]. Rockets have been used to collect data samples at mesospheric altitudes, often for PMC composition and formation studies [78], however they do not provide substantial opportunities for conducting imaging experiments. Early space-based research into PMCs generated significant contributions to the field when limb-scanning measurements made by an airglow photometer onboard the OGO 6 satellite observed a scattering layer, which extended to the poles and increased in brightness in the poleward direction [79]. This discovery led to the terminology polar mesospheric cloud [67]. Prior to that time they had been referred to as noctilucent clouds (NLCs) or night-shining clouds. The term noctilucent cloud (NLC) is still used in the literature and is typically reserved for ground-based observation. There appears to be no difference between NLCs and PMCs and the two terminologies are mostly used to distinguish space-based observation (PMC) from ground-based observation (NLC) [80].

Satellite observations of PMCs began with Soyuz 9 in 1970 [81] and were later conducted from Skylab [82]. The Solar Mesosphere Explorer (SME) spacecraft, launched in 1981, was used to conduct spectroscopic observations of the PMC layer [83]. Additional mesospheric data were acquired by the Upper Atmosphere Research Satellite (UARS) [84] and the Thermosphere Ionosphere Mesosphere Energetics and Dynamics (TIMED) satellite [85]. The Swedish-led satellite Odin with its onboard Optical Spectrograph and Infrared Imaging System (OSIRIS) was not launched with the intention of mesospheric investigation but rather of ozone depletion and star formation studies [86]. The satellite outlived its required lifetime of two years and the OSIRIS instrument has subsequently been used to collect additional atmospheric data using limb-scans from 15-120km in altitude [86, 87].

Line-of-sight brightness measurements have also been acquired using the onboard infrared imager (IRI), a component of the OSIRIS instrument. These data provided multiple-angle views and facilitated a tomographic imaging approach, which has been explored and applied to OSIRIS data by various authors since Odin was launched in 2001. Degenstein *et al.* investigated the feasibility of retrieving atmospheric structure from a series of limb images taken aboard a satellite using a likelihood expectation maximization algorithm [88]. They concluded that even in the presence of substantial observational noise, it is possible to retrieve both horizontal and vertical structure. These same authors later used data collected by the IRI to map volume emission rates of the oxygen infrared atmospheric (OIRA) band [44].

The Odin satellite mission consequently represents a significant advancement in space-based mesospheric studies as it marks the first time that tomographic inversion methods have been a significant component of the resulting data analysis. Tomography is a powerful imaging tool, which has long been used in medical diagnostics and is currently experiencing a rapid expansion of applications in a wide range of fields. The Aeronomy of Ice in the Mesosphere (AIM) satellite, launched in 2007, is the first satellite mission in history

with the primary objective of studying PMCs [89]. The Cloud Imaging and Particle Size (CIPS) experiment provides four onboard cameras capable of unprecedented 2km horizontal resolution at mesospheric altitudes. The AIM satellite and the corresponding CIPS data consequently provide a unique opportunity for studying PMCs.

The present work represents some of the first efforts to reconstruct vertical profiles of PMCs from AIM satellite data. The imaging configuration of the CIPS cameras onboard the AIM satellite is examined and the challenges of using satellite data in tomographic reconstructions are discussed. The tomographic theory of sparse data is examined as it relates to the AIM-PMC geometry. Algorithm validation is conducted using synthetically created data and the results of tomographic methods applied to the CIPS data are presented and discussed. The data are interpolated to a finer resolution using a cubic spline to explore the impact it has on the vertical profile of the reconstructions. The PMC layer is geometrically thin (1-3km) [90] and has presented a challenge for limb-scanning instruments, which are often used to map atmospheric profiles, including OSIRIS [91]. The interpolated data are reconstructed using the same tomographic methods and the vertical structure is analyzed. The prospect of future satellite data collection at higher resolutions is discussed, as well as the importance of tomographic applications to PMC studies.

5.2. Methods

The predominant challenge associated with the application of tomographic methods to atmospheric measurements is the sparsity of the acquired data. More conventional applications of tomography typically involve data, which has been collected from large arrays of sources or viewing angles. In medical CT, emitters and receivers are rotated around the region of the body that is to be imaged. The resulting data are collected from hundreds or even thousands of source and receiver positions. Large amounts of data collected from large numbers of viewing angles provide for a well-conditioned solution set and thereby reduce the indeterminacy of the inverse problem. This allows for high-resolution recon-

structions capable of resolving fine structure with little or no a priori information about the imaging region required for initializing the algorithm. Atmospheric data are very different by comparison as the region to be imaged is inherently less accessible. Measurements are often collected by only a few receivers and the high altitudes involved can restrict the range of available viewing angles.

Despite these challenges, optical tomography has proven to be a powerful imaging tool in a variety of fields. Specific classes of correction algorithms have been developed for approximating solutions to highly underdetermined inverse problems. Such ill-conditioned systems can, however, be highly sensitive to the initialization of the algorithm or the so-called initial guess, and therefore present their own unique complications. Accurate reconstructions of sparse data therefore require a sound understanding of the applied algorithm and how it relates to a specific imaging configuration. The initialization of the algorithm with a priori information is also necessary in order to obtain the desired convergence. This section examines the acquisition of the AIM data and its unique imaging configuration, along with the choice of a correction algorithm and its initialization using a Gaussian layer.

5.2.1. Imaging Configuration

The AIM satellite was launched from Vandenberg Air Force Base (CA), by the Pegasus XL rocket on April 25, 2007. Its retrograde orbit with an inclination of 97.8° is nearly polar and exhibits a period of 96 minutes and 32 seconds [89]. The altitude of the AIM satellite varies slightly, but an approximate height of 600km was used in the reconstructions. The typical occurrence altitude of PMCs is 82-83km [90] and a height of 83km was used as the center of the initial guess in the correction algorithm. This implies that the AIM satellite orbits at an altitude of 517km above the PMC layer as can be seen in Fig. 5.1.

The CIPS experiment provides four onboard cameras facing in the forward, aft, port, and starboard directions. The composite instrument is a wide-angle imager with a field of view spanning 120° along track and 80° across track (1800x800km) [92]. Images are

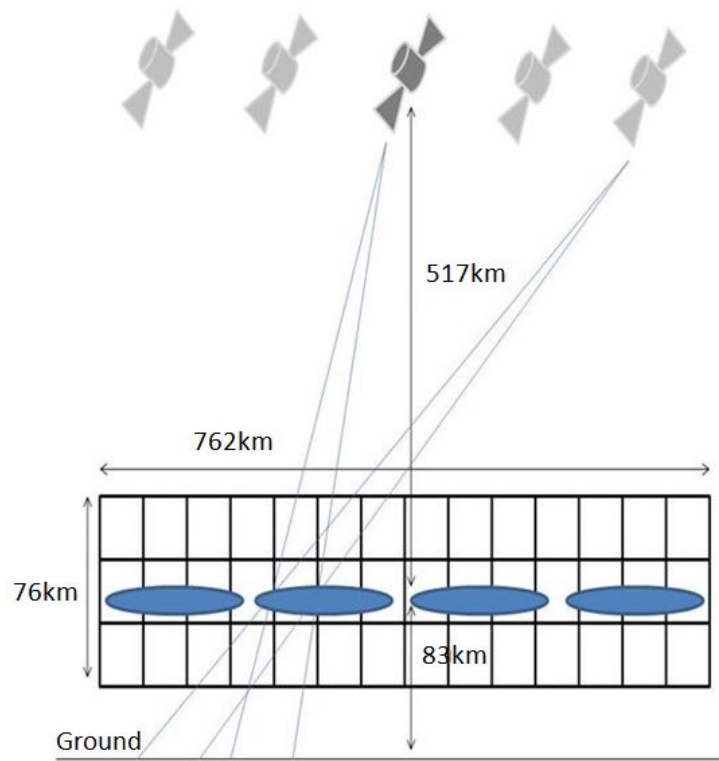


Fig. 5.1. An illustration of the imaging configuration from which the reconstructed data were acquired. The AIM satellite orbits 517km above the PMC layer at an altitude of approximately 600km. Photographs were taken by onboard CIPS cameras at five orbital positions and used to reconstruct PMC profiles.

acquired by each of the four cameras simultaneously at varying orbital positions and then merged and binned to form a single composite image called a scene. An example of a composite image from the four cameras is shown in Fig. 5.2.

Figure 5.2 also illustrates the overlapping technique, which is used to extract a common profile from multiple angular views. Images are acquired by the CIPS cameras at consecutive orbital positions separated by 190.5km. The field of view spans 1800km along the orbital direction allowing the same region of the PMC layer to be visible in multiple scenes. In order to acquire the needed projection data, five adjacent scenes were overlapped and an imaging region common to each was identified. This region is represented by the yellow line in Fig. 5.2. The emission intensities measured along the same linear section of the

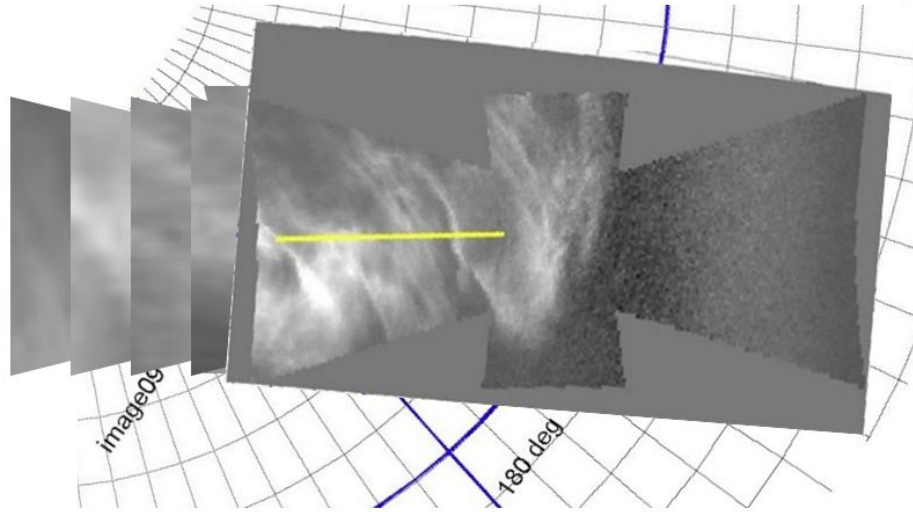


Fig. 5.2. An example of a composite scene created from images acquired by the four CIPS cameras onboard the AIM satellite. Also shown is the overlapping technique from which a common profile is extracted from five composite scenes and used to create tomographic reconstructions of PMCs.

PMC layer comprised a set of five different angular views from the image data that were used to create the reconstructions in this study.

5.2.2. Tomographic Theory

Accurately reconstructing atmospheric layers presents a unique tomographic challenge. Regardless of the method used for data collection, the number of available viewing positions from which the data are acquired is inherently limited compared with other applications. This restriction increases the indeterminacy of the inverse problem and can make convergence to a high-fidelity solution difficult. Satellite acquisition of image data is a promising method for performing atmospheric tomography, yet provides its own specific complexities. The obtaining of an optimal spread of tomographic ray geometries necessitates that the separation of imaging locations be comparable to the altitude disparity between the imagers and the layer itself. The CIPS data were acquired at locations separated by 190.5km, suggesting a tomographically optimal orbital altitude of 273.5km. The actual

AIM orbital altitude of 600km accordingly narrows the angular spread of the rays, which can complicate reconstruction.

Large-scale tomographic measurements often provide sparse data sets, which are most appropriately solved using a class of correction algorithms known as matrix methods. In contrast to the set of transform methods wherein projected rays can be approximated as continuous because of their dense distribution, matrix methods provide a quantized description appropriate for low ray densities. The assumed continuity of the imaging object and its projections is replaced by a discretized representation, and the imaging region is given a discontinuous structure through division into pixels. This quantization of the imaging object and its projections gives rise to a linear description and a matrix formalism [18].

In the discretized representation, the projection p is equal to the product of the weighting factor w and the pixel value f :

$$p = wf. \quad (5.1)$$

The weighting factor represents the individual contribution of a pixel to the attenuation of the ray passing through it. In straight-line tomography, attenuation is characterized by a decrease in the signal measured at a given angle. This is typically caused by scattering as it is a more dominant mechanism than absorption in most translucent materials. The contribution of a pixel is often represented by the length of a ray segment traversing the pixel or more accurately by the area of the ray intersecting the pixel. The total measured projection along a given angle resulting from the ray's interaction with N pixels can be expressed as the sum:

$$p = \sum_{n=1}^N w_n f_n. \quad (5.2)$$

In matrix methods, the number of rays reaching a receiver is finite and the projection of the m_{th} ray through the imaging region is given by:

$$p_m = \sum_{n=1}^N w_{m,n} f_n. \quad (5.3)$$

These projections constitute a projection vector and the individual sums define a system of equations, which result in the matrix equation $\mathbf{p} = \overline{\mathbf{W}}\mathbf{f}$. This system is often difficult to solve. In practice this complication is a consequence of underdetermined systems, which result from sparse data sets and have no unique solution [18]. The approximate solutions of large matrix equations can be difficult to accurately obtain and minimizing the error associated with such solutions forms the foundation of algebraic tomography.

The challenge of accurately reconstructing sparse data can be minimized through certain approaches. The use of a fundamentally compatible correction algorithm, which is also appropriate for the ray geometry, is of critical importance. The calculation of the weighting factors used in the correction algorithm should be as accurate as possible and the algorithm itself should be capable of approximating solutions to highly underdetermined systems. There is a class of correction algorithms known as the algebraic reconstruction techniques (ARTs), which are able to process sparse data and are commonly used in tomographic applications. Within this set of algorithms there exist variations of the fundamental unconstrained algebraic reconstruction technique (ART) including the constrained algebraic reconstruction technique (CART), simultaneous ART (SART), and multiplicative ART (MART) [18]. Additional related algorithms include the simultaneous iterative reconstruction technique (SIRT) and a method that utilizes the ART algorithm, but stores critical values for later use known as memory ART. A slight variation of the constraint used in CART leads to the partially constrained algebraic reconstruction technique (PCART). The ART algorithms have been tested in various applications and can have vastly different convergence properties depending on their usage [25]. The authors have conducted algorithm testing in the context of the AIM/CIPS data for the previously mentioned algorithms and have determined that PCART exhibits the optimal accuracy. PCART has also been applied by the authors to two-station tomography of airglow and appears to be an apt choice when the data is particularly sparse and the resulting matrix equation is highly ill-conditioned.

The PCART correction algorithm is expressed as

$$f_{m,n} = f_{m-1,n} + \lambda \frac{(p_m - p_m^i)w_{m,n}}{N_m}, \quad (5.4)$$

where $f_{m,n}$ is the discrete value of the reconstructed image for the m th ray and the n th pixel. The iterative nature of the algorithm is evident in the addition of a correction term to previous image values $f_{m-1,n}$. The elements of the weighting matrix are given by $w_{m,n}$ and the rate at which the algorithm converges to its terminal value can be controlled by λ , the relaxation parameter. The physically measured projections are given by p_m and the corresponding computed projections, calculated using the weight matrix and the current values of the image vector $f_{m,n}$, are given by p_m^i . The measured and computed projections are compared by subtraction in the algorithm to assess the comparability between the imaging object and its reconstruction. The total weight of the m th ray, N_m , is equivalent to the sum of each individual weighting factor for the N pixels in the imaging area. It is expressed as

$$N_m = \sum_{n=1}^N w_{m,n}, \quad (5.5)$$

and used in the denominator to effectively normalize the correction term. The constraint used in PCART prevents negative correction factors by setting them to zero in the iteration.

The value $f_{0,n}$ used to initialize the algorithm can have a substantial impact on its final convergence, particularly when the inverse problem is ill-conditioned. This initial value of the reconstructed image is used as the basis for subsequent correction terms and is often called the initial guess. The choice of an effective initial guess in applications of tomography to sparse data is consequently of great importance to the accuracy of the reconstructions. In addition to the chosen correction algorithm, an accurate initial guess can substantially reduce the difficulties associated with particular imaging configurations. If the data is sufficiently limited, as it is in the case of the AIM data, a poor choice of initial guess will prevent even the most suitable of algorithms from being able to create sufficiently accurate reconstructions. Conversely, an effective initial guess can minimize the

difficulties associated with sparse data and cause the algorithm to correctly converge in a way which would not otherwise be possible.

5.2.3. Data Interpolation

Another difficulty associated with performing satellite-based tomography of PMCs is inherent in the PMC layer itself. The PMC layer is thin and only extends over a vertical distance of a few kilometers. This is in contrast to other mesospheric phenomena, such as airglow emission bands, which can exhibit vertical extents as large as 10km. The CIPS instrument onboard AIM consists of four wide-angle cameras, which measure scattered light at a wavelength of 265nm. The AIM satellite orbits approximately 517km above the PMC layer, causing the corresponding resolution at PMC altitudes to be limited by the large distances involved. The CIPS cameras are capable of providing an effective horizontal spatial resolution of 2km in the nadir. This value decreases away from the nadir and falls to roughly 5km at the edges of the forward and aft cameras. The raw data are binned on-chip to form images with spatially varying resolutions, which are then merged to form scenes (see Fig. 5.2) and in some cases intentionally degraded to 5km resolution in order to compensate for geometric smearing [93]. This is done to create a uniform spatial coverage.

Extracting a common profile from a series of scenes allows for an optimization of the resolution. This study utilized data sets with effective spatial resolutions of 2km to extract the common profile. This value, preferred to the 5km spacing of other data sets acquired from the CIPS images, still presents a challenge for tomographic reconstruction. As mentioned previously, the depth of the PMC layer is typically 1-3km. As a result, the acquired data from the CIPS images provides a spatial resolution, which is comparable to the vertical extent of the layer. The vertical distribution of the layer would accordingly be displayed as a single pixel in the reconstructions. This complication would likely prohibit the delineation of any vertical structure or altitude variation, both of which are of interest in PMC studies. For this reason the data acquired by the CIPS cameras were interpolated using a

cubic spline as shown in Fig. 5.3. Resulting data sets have been acquired with artificial resolutions of 1, 0.5, and 0.25km. The interpolated data were reconstructed using the PCART algorithm along with the 2km CIPS data reconstructions.

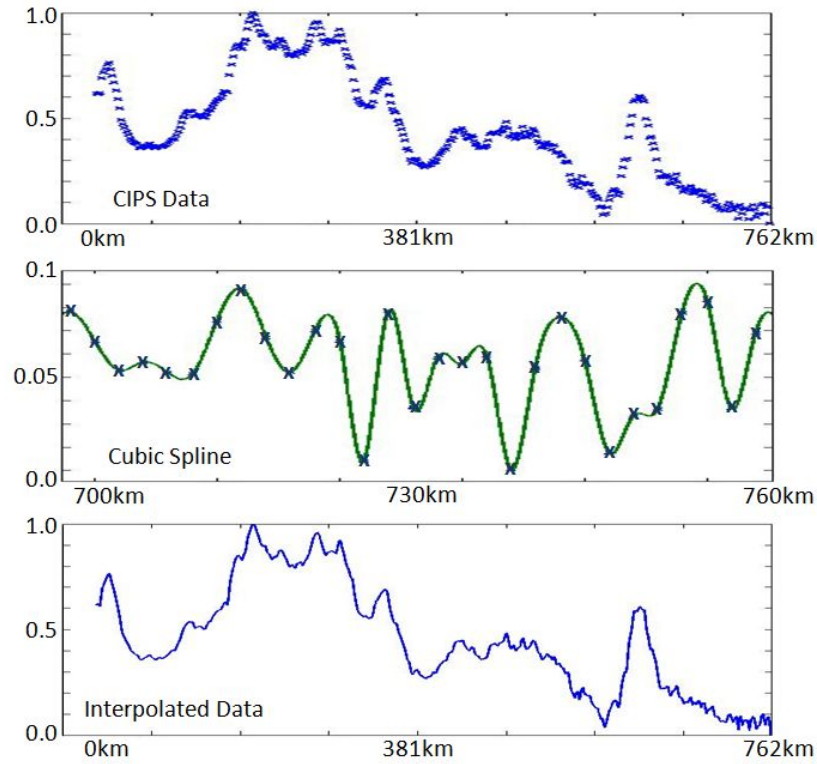


Fig. 5.3. The interpolation procedure used to refine the 2km spatial resolution of the data collected by the satellite-based CIPS cameras. The original data are shown (top) which include 381 measurements along the 762km imaging region of the PMC layer. A portion of the cubic spline used to interpolate the data is shown (center) along with the corresponding data points. The interpolated curve, used to create the higher-resolution reconstructions, is also shown (bottom). The relative intensity is displayed on the vertical axis in each plot.

5.3. Results

The presented reconstructions can be divided into three types based on the origin of the data used in their creation. A synthetic reconstruction, generated by artificial data, is first presented as a means of validating the accuracy of the tomographic algorithm. The images formed from the 2km resolution CIPS data are then presented followed by the

reconstructions of the interpolated data sets. These images show the same structure at resolutions of 1, 0.5, and 0.25km and allow for the imaging of increasingly finer PMC structure.

5.3.1. Synthetic Data and Validation

In the reconstruction of sparse data, the initialization of a correction algorithm is often critical for determining the accuracy of the generated image, and should resemble, as closely as possible, the object to be reconstructed. The object of interest in atmospheric tomography is often a cloud or emission layer, which extends over a limited vertical distance at a known altitude. The Chapman emission profiles of airglow layers approximate a Gaussian-like structure with a central peak, and the authors have successfully used a Gaussian layer as the initial guess in airglow tomography. A Gaussian layer centered at a height of 83km was therefore used as the initial guess in the reconstructions of the PMCs and is shown in Fig. 5.4.

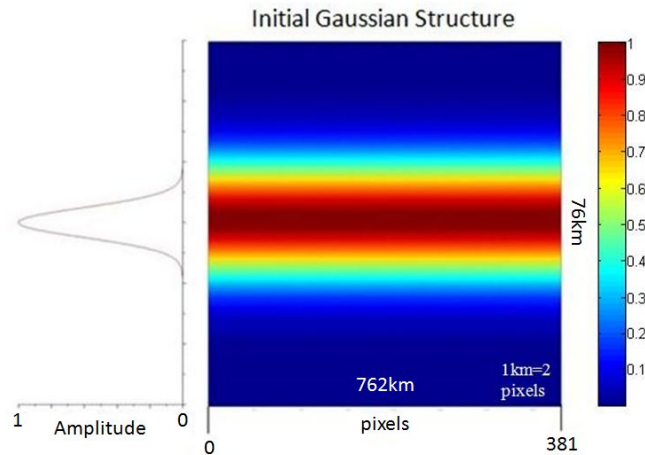


Fig. 5.4. The Gaussian layer used to initialize the PCART algorithm in the synthetic testing and PMC reconstructions. The initial guess was centered at a height of 83km to correspond with experimental predictions of PMC altitudes. The width of the layer was chosen to be sufficiently larger ($\sim 4\times$) than the typical vertical extent of PMCs. This was done to ensure that the upper and lower boundaries of the reconstructions were not influenced by the initialization of the algorithm.

The accuracy of a Gaussian initial guess in reconstructing layered objects was tested using an artificial imaging object. Synthetic testing is performed in tomographic applications as a means of validating the applied technique. Applying the imaging configuration specific to the AIM satellite, synthetic imaging objects were generated by artificially specifying the values of f corresponding to a terminal iteration value. The synthetic object was then combined with the calculated weighting matrix in a forward modeling approach to create synthetic projections of the artificial object. These synthetic projections were processed by the correction algorithm (PCART) to generate reconstructed images. The validity of these images was determined through comparison to the original artificial imaging object. Successive synthetic testing was used to acquire an understanding of the behavior of the reconstruction algorithm under specific conditions. The combination of these assessments provided the accuracy of the PCART algorithm in this particular imaging configuration. Confidence in reconstructions of measured projection data were obtained through synthetic testing of objects, which closely resembled the authentic imaging object of interest. Height variation was intentionally included in the synthetic object to test the algorithm's ability to discern vertical information in the data. The synthetic object and its reconstruction are shown in Fig. 5.5.

The accuracy of the synthetic reconstruction is evident. While minor discrepancies exist, the overall structure has been reproduced. It was determined during synthetic testing that the reconstruction algorithm achieves its maximum accuracy when the vertical position of the initial guess coincides with that of the object being imaged. The algorithm is able to accurately reproduce both horizontal and vertical structure when these altitudes coincide. The algorithm converges to a terminal value after approximately 20 iterations. An advantage of the Gaussian initialization method is its ability to create an optimal image when the thickness of the Gaussian is slightly larger than the imaging object. This ensures that the upper and lower boundaries of the reconstructed object are not artificially introduced,

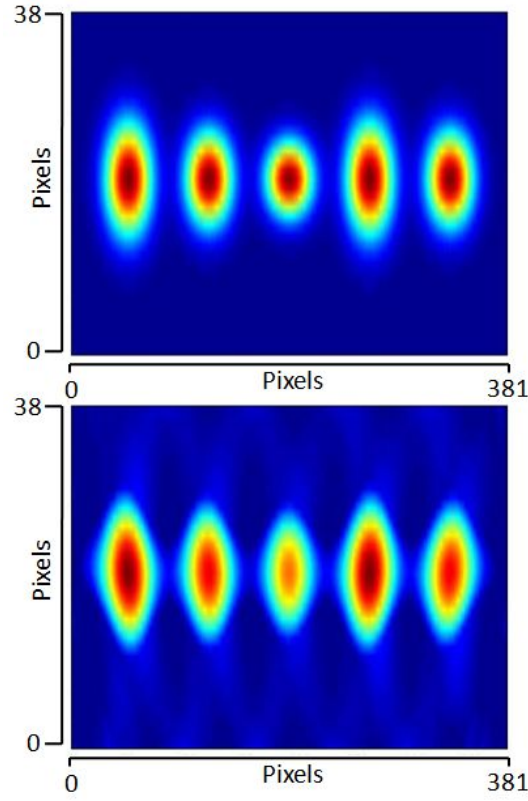


Fig. 5.5. Typical synthetic testing performed using an artificially generated object in combination with a Gaussian initial guess and actual imaging configuration. A known synthetic object is created (top) with certain properties in order to test the ability of the correction algorithm to correctly distinguish desired structure. In the case of the AIM configuration, height variation and asymmetries were intentionally included for validation purposes. The reconstructed object (bottom) demonstrates the capabilities of the applied technique.

a feature that is important in the analysis of vertical structure. It is also applicable to PMC reconstruction since the layer is relatively thin.

5.3.2. PMC Layer Reconstructions

Confidence in the presented tomographic method and the PCART correction algorithm was achieved through repeated use with a variety of data. Application to previous atmospheric tomography supported the robustness of the technique and its particular capabilities for reconstructing highly sparse data when provided with an accurate initialization. Synthetic testing provided an evaluation of the algorithm's performance relative to a specific

imaging configuration. In this case the testing was done with the ray geometries created by the orbital locations of the AIM satellite. A study of the properties of the PCART algorithm and the behavior of the applied technique under specific conditions, including the influence of the initial guess, supported its ability to accurately reconstruct AIM data. As a result, the described method was used to reconstruct images of the PMC layer using data collected by the onboard CIPS cameras.

Unlike horizontal structure, the reproduction of vertical structure in the PMC layer presents a unique challenge because of its extent. The layer is thin (1-3km) and is comparable in depth to the 2km spatial resolution of the cameras. The resulting reconstruction would consequently display the vertical dimension of the layer with only one or two pixels. This would severely complicate any analysis of altitude variation in the PMC layer. In order to overcome this difficulty, the 2km data was interpolated using a cubic spline to 1, 0.5, and 0.25km resolutions. The reconstructions from increasingly finer data sets are shown in Fig. 5.6.

The reconstructions in the figure represent the entire imaging area, a common region capable of being extracted from five consecutive scenes (yellow line in Fig. 5.2). They span a relatively large horizontal distance of 762km. In order to make vertical variation more visible, close-up images of certain regions are shown in Figs. 5.8 and 5.9, which span shorter distances and are more representative of the physical aspect ratio of the reconstructions.

Another promising feature of the reconstructed images is seen in the vertical extent of the PMC layer. As the resolution increases, the thickness of the layer gradually decreases from a non-physical value of 10-12km to a value of 5-6km, which is in closer agreement with physical measurements. The FWHM was computed for each of the layers shown in Fig. 5.6 at its widest point. These values were then fitted to a power-series curve in order to project what the thickness of the layer would be at higher resolutions. This was done in order to test the stability of the interpolated data and to determine whether the

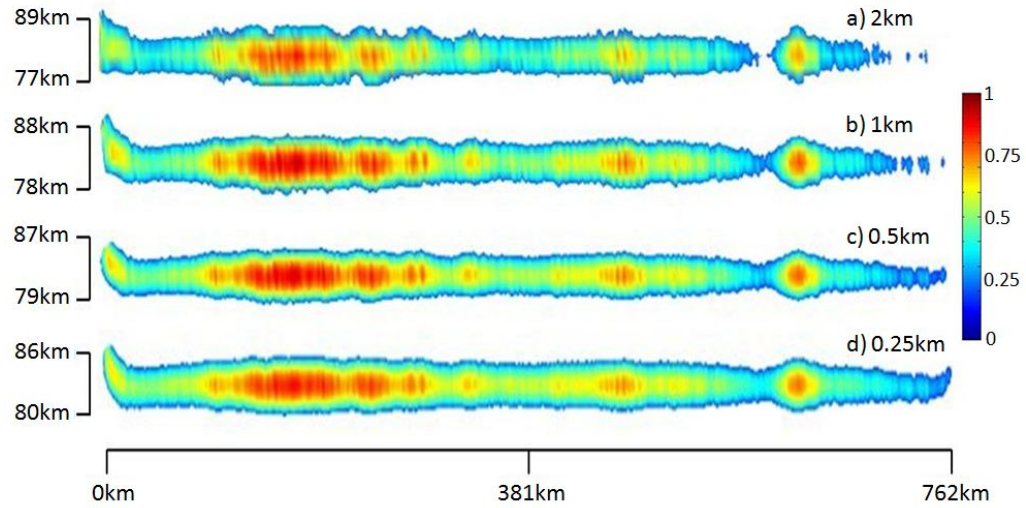


Fig. 5.6. Tomographic reconstructions of the PMC layer from data collected by the CIPS cameras onboard the AIM satellite, shown with increasingly higher resolution from top (a) to bottom (d). The gradually finer detail visible in the images is made possible by successive interpolation of the original data. The layers have been removed from their backgrounds and are shown with spatial resolutions of a) 2km, b) 1km, c) 0.5km, and d) 0.25km.

layer thickness would converge to a physically meaningful value. The FWHMs of each reconstructed layer are shown as a series of points (represented by blue circles) along with the fitted curve in Fig. 5.7.

In the figure (5.7), the FWHM is plotted as a function of the number of pixels per kilometer (p/km). A value of 0.5 thereby corresponds to the 2km resolution data set. Values of 1.0, 2.0, and 4.0 correspond to the 1, 0.5, and 0.25km resolution data sets, respectively. The FWHM of the layers reconstructed from these data sets were calculated to be 8.20, 6.53, 5.18, and 4.15km, respectively. While the curve does not converge to any nonzero value, it approaches zero slowly. The predicted FWHM is 1.15km at a value of 200 p/km, 0.91km at 400 p/km, and 0.80 at 600 p/km. These values are in good agreement with the 1-3km thickness described for PMCs in the literature.

A clearer delineation of structure and pseudo-convergence to a physically representative vertical extent supports the increasing accuracy of the successively interpolated recon-

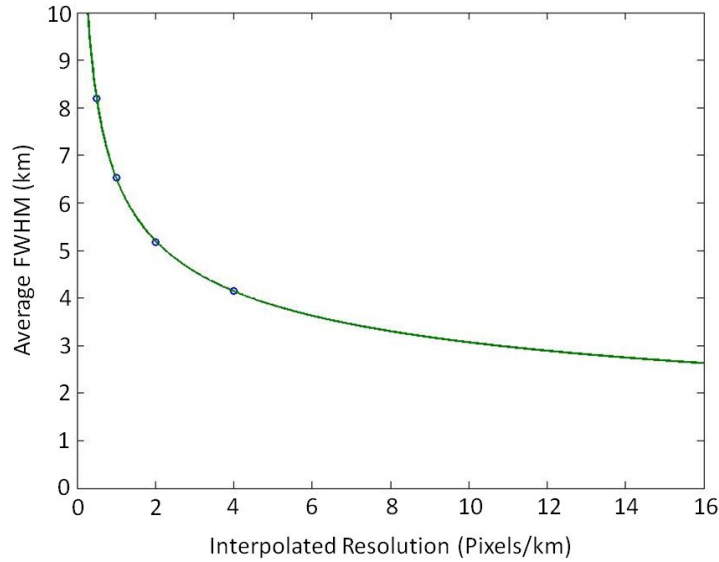


Fig. 5.7. The predicted layer thickness as a function of interpolated resolution. The FWHM of each reconstructed layer shown in Fig. 5.6 was calculated at its widest point. These values (represented by blue circles in the plot) were then fitted to a power-series curve in order to project what the layer thickness would be for higher resolution data. This was done to test the stability of the interpolated data and to determine whether the thickness would converge to a physically meaningful value. Successive interpolations are predicted to yield values within good agreement of the 2-3km PMC thickness described in the literature.

structions. The Gaussian used to initialize the correction algorithm was several times wider than the resulting layers, suggesting that the reconstructed boundaries were created by the algorithm itself and were not artificially influenced by the initial guess. The reconstructions demonstrate the viability of satellite-based tomographic measurements as a means of studying the PMC layer. More specifically, the interpolated data demonstrate the type of structure, which is visible at varying resolutions. The successful application of tomographic reconstruction, particularly from interpolated data, to PMC studies could serve as a foundation for future data collection.

5.4. Discussion

The presented results demonstrate the viability of the applied technique for use in tomographically reconstructing data from the CIPS cameras. The imaging configuration of

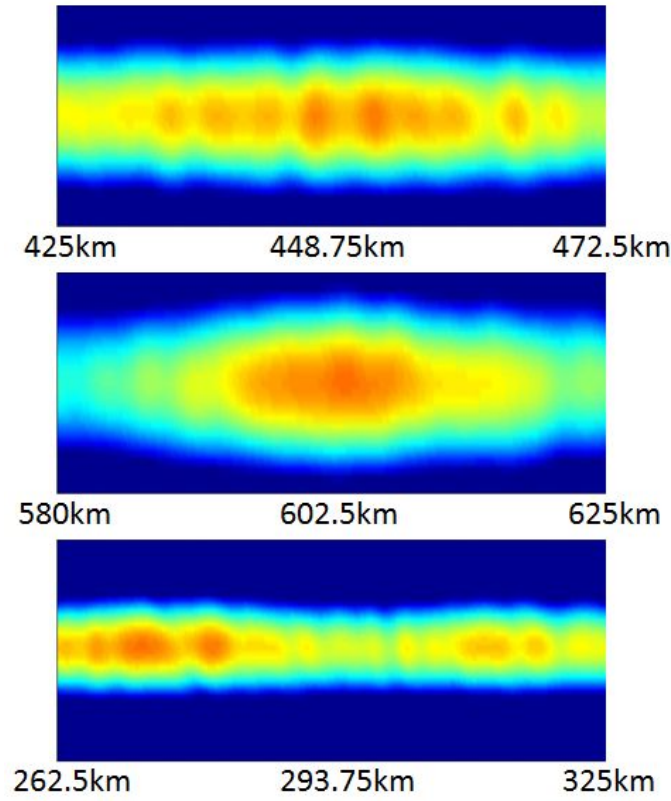


Fig. 5.8. Various portions of the 0.25km-resolution reconstruction of the PMC layer shown in Fig.5.6. The layer is seen from different vantage points (closeup) in order to aid in distinguishing structure.

the AIM satellite exhibits limited angular views, which lead to sparse data. Despite the ill-conditioned nature of the resulting inverse problem, the applied algebraic correction algorithm (PCART) has been shown to be capable of accurately imaging the desired PMC structure. The excellent convergence of the algorithm is made possible by its initialization using a Gaussian layer as the initial guess. Provided that sufficient a priori information exists concerning the depth or altitude of the structure to be imaged, the layered initial guess approach could be an effective technique in a variety of fields. One-sided imaging problems often involve layered or stratified structure. This is encountered in fields such as geophysics, biophysics, and as shown here, atmospheric studies. The relevant imaging configurations are typically prone to the same challenges of restricted ray distributions

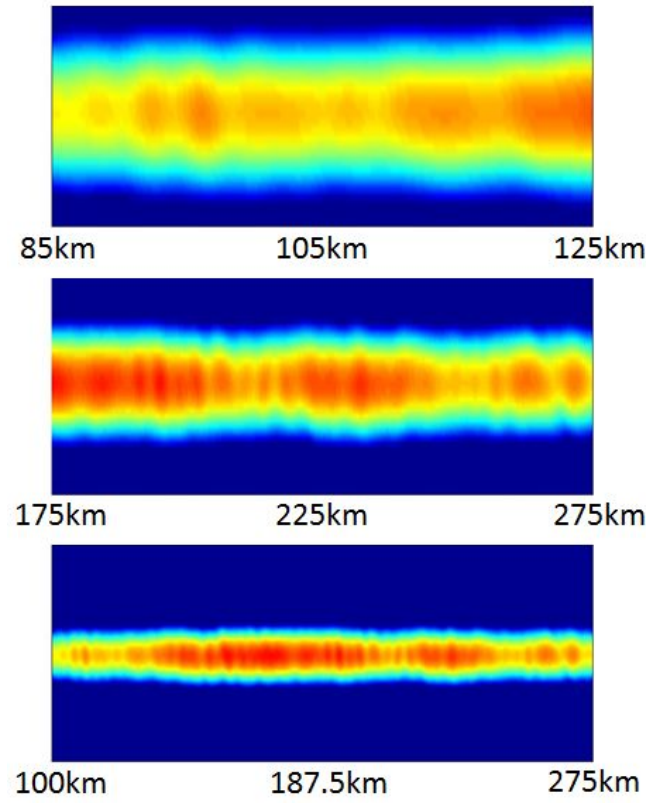


Fig. 5.9. Additional portions of the 0.25km-resolution reconstruction.

and sparse data, making tomographic inversion difficult. The successful application of the PCART algorithm, provided with a layered initial guess, to the AIM satellite data supports the use of algebraic correction techniques in PMC studies. It also provides evidence that an accurate initialization can have a substantial effect on the resulting reconstruction, making algebraic tomography a powerful tool in a variety of fields with similar imaging challenges.

This work also contributes to the validation of satellite-based measurements for use in studying the PMC layer. The AIM satellite mission was the first to proclaim PMC study as its primary objective and has provided unprecedented opportunities for data collection and interpretation. The CIPS cameras allow for relatively high-resolution imaging along the trajectory of the satellite. A common profile extraction technique using multiple composite scenes allows for data sets with 2km spacing. Further analysis and interpretation of the

data collected from the AIM mission, along with the tomographic methods presented in this paper, could help to form a foundation for future satellite-based study of PMCs.

The CIPS data were interpolated to higher artificial resolutions using a cubic spline. The reconstructions of these interpolated data revealed successively clearer structure with increasingly finer interpolation. The detail evident in these spline reconstructions establishes interpolation as a valuable technique for atmospheric imaging. The large distances associated with atmospheric tomography can limit the spatial resolution of cameras, particularly at satellite altitudes. This is of particular significance in PMC studies as the vertical extent of the layer is only a few kilometers. The ability to resolve variations in the altitude of the PMC layer consequently requires a spatial resolution, which is several times higher than its thickness. The delineation of vertical structure is important to understanding the formation of PMCs and the degree to which they are influenced by global temperature increase and climate change. Data interpolation provides for a more clearly defined structure in the resulting images and facilitates a study of height variations in PMCs.

The reconstructions suggest a number of possibilities for further data collection and interpretation. The use of 3D tomography to reconstruct a model of the PMC layer from multiple profiles could be a valuable imaging tool. Fig. 5.10 shows a fanning technique in which multiple common profiles are extracted at various angles measured from the zenith. This results in a series of reconstructed images, which represent multiple cross-sectional slices through the layer. A series of reconstructed images could be combined to generate a 3D model of the PMC layer. The authors have successfully applied this fanning technique to create 3D models of airglow layers. One advantage of such a model is the ability to image structure perpendicular to the camera array.

Tomographic imaging provides several advantages for studying the formation and dynamics of PMCs. Reconstructed images provide views of the layer's internal structure and information about its vertical extent, which are not available in ground-based or over-

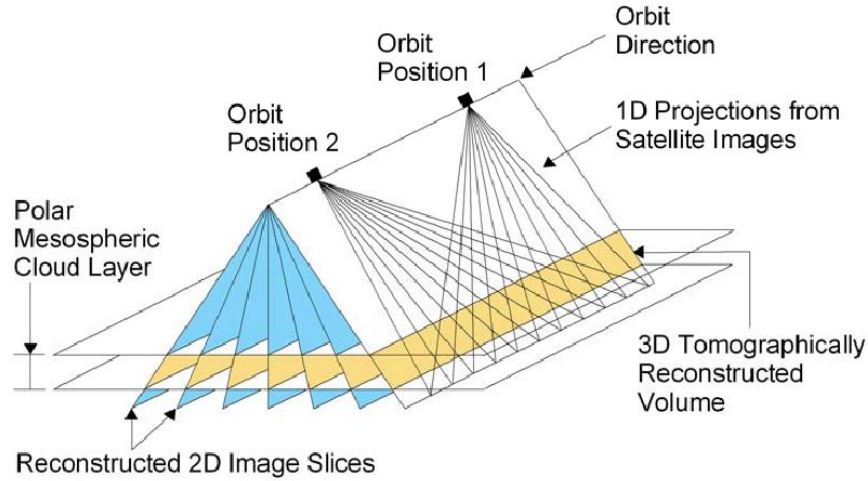


Fig. 5.10. A proposed method for creating 3D reconstructions of PMCs using the CIPS image data from the AIM satellite and the fanning technique developed by the authors for use in airglow tomography. Multiple profiles are extracted along planes forming an angle with the zenith and used to create a series of reconstructed cross-sectional slices which are combined to generate a 3D model.

head imagery. Additional information concerning the apparent increase in PMC occurrence could lead to an improved understanding of its connection to climate change. One possibility, which is of interest for further study, is the quantification of height variations observed in the layer. PMCs form under specific conditions, which include narrow ranges for temperature and ambient moisture content [68]. The altitudes at which these conditions are present could provide global climatologic information. The images reconstructed using the AIM data, however, do not show any significant altitude variations. This point is worthy of discussion as it would be important to any future tomographic studies of noctilucent clouds.

Closer examination of the CIPS instrument offers an explanation for the apparent lack of vertical fluctuation. The CIPS cameras acquire images every 43 seconds [94]. The scenes used to extract tomographic projection data consisted of five consecutive images taken at 43-second intervals. A given scene thereby represents a temporal span of 172 seconds. The effect of tides on the motion and structure of noctilucent clouds has been noted in the literature by a number of authors and tidal oscillations have been attributed

to diurnal variations in the PMC layer [95]. Tidal periods exhibit amplitudes of only a few feet and occur over the course of several hours, a temporal span much larger than the few minutes represented in scenes acquired by AIM. Consequently, the CIPS data is not particularly suited for studying long-term temporal variations.

The AIM data presents challenges tomographically for a number of reasons. The imaging configuration only incorporates five viewing angles as opposed to the several hundred angles made possible by the exposure frequency of OSIRIS aboard the Odin satellite. This leads to sparse data and an ill-conditioned inverse problem, the difficulties of which have been addressed in the presented research along with methods for overcoming limited projections. Future tomographic studies of noctilucent clouds will also need to address the feasibility of observing changes in the layer, which occur over large spatial scales or long temporal periods. Possible approaches to these challenges include comparing reconstructions acquired at the same location over a period of several days, a technique that is best suited for ground-based observation. Large-scale PMC dynamics could also be acquired from satellite imagery by reconstructing a series of adjacent scenes obtained during an entire orbital period.

Another approach is suggested here, which may provide information about small-scale fluctuations from which larger trends could potentially be identified. The intensity of the reconstructed images is vertically asymmetric and a study of the peak emission altitude at each horizontal position in the imaging grid could indicate the presence of vertical oscillations and gravity wave induced structure. The centroid c of the m th vertical intensity profile can be computed using

$$c_m = \frac{1}{E_m} \sum_{n=1}^N e_{mn} d_{mn}, \quad (5.6)$$

where e is the emission intensity at a given point and d is the distance (in pixels) from that point to the bottom of the imaging grid. The sum runs across the N pixels in a given column of the imaging grid. The sum of the intensities in a vertical emission profile can be

expressed as

$$E_m = \sum_{n=1}^N e_{mn}. \quad (5.7)$$

The values of c were computed using this formula and are plotted with respect to the horizontal location of each vertical profile in Fig. 5.11. Minor fluctuations are seen over short-range (2-3km) spans and a general upward trend across the entire length of the reconstruction is seen in the top image of the figure. Techniques such as this could be a valuable tool in the study of gravity wave perturbations in PMCs and merit further investigation.

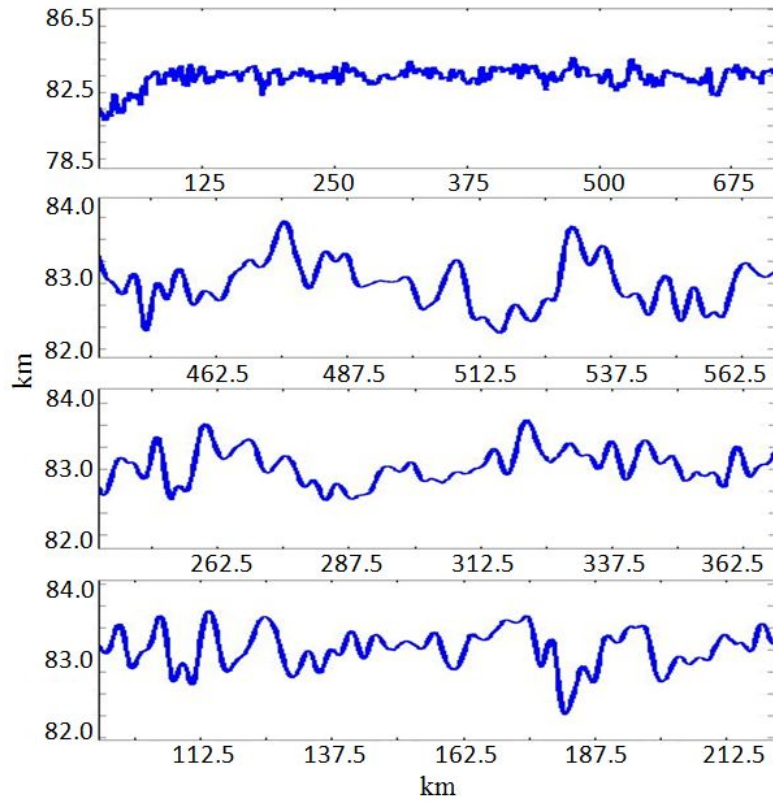


Fig. 5.11. Vertical emission profile centroids plotted against position. The tomographic reconstruction shown in Figs. 5.6, 5.8, and 5.9 is vertically asymmetric and the altitude of the peak intensity varies with the horizontal position. Vertical emission profiles were extracted from the reconstructed image and the centroid of the profiles was computed using equation (5.6). The calculated centroids are shown plotted as a function of the horizontal position of the corresponding vertical profile. The top image shows the fluctuation across the majority of the reconstructed layer with closeup views beneath. The method is suggested as a means of identifying small-scale altitude fluctuations present in the reconstructed PMC images.

5.5. Conclusion

Albedo measurements acquired by the CIPS cameras onboard the AIM satellite were used to tomographically reconstruct images of the PMC layer. An overlapping method was used to extract common profiles from a series of composite scenes. These data were used to establish a tomographic inverse problem, ill-conditioned as a result of the restricted ray geometries inherent in the high altitude of the satellite. The PCART correction algorithm was applied to the inverse problem and initialized using a Gaussian layer. This initial guess makes accurate reconstruction of sparse data possible and supports the use of algebraic tomography in a variety of fields, which encounter challenging imaging configurations. The data were interpolated to higher resolutions using a cubic spline and reconstructed using the same algorithm. The finer detail available in these higher-resolution reconstructions allows for the study of vertical variation in the PMC layer. This is essential to a better understanding of PMC formation and its relationship to climate change. The presented work demonstrates that tomographic reconstruction is a powerful technique for analyzing the AIM data and studying the PMC layer. Satellite-based measurements have provided unprecedented opportunities for atmospheric study; and continued data collection, particularly at higher resolutions, could be essential to the future of PMC studies.

CHAPTER 6

DIFFUSE TOMOGRAPHY

Each of the tomographic theories and applications, which have been presented thus far, can be classified as straight-line tomography. The majority of tomographic methods, including most medical imaging modalities, can be described as such. The distinction is appropriate for tomographic techniques in which the imaging object does not cause a significant amount of diffraction at a given wavelength. An incident ray is attenuated, but its direction is essentially unchanged. The straight-line description of projections is the most widely used and by far the simplest to implement computationally. It is also pertinent in a number of fields as the need to penetrate an object to a desired depth results in the use of wavelengths, which traverse the imaging region with little interaction.

There are, however, instances in which the imaging region is particularly dense and causes nonnegligible scattering. The use of light at certain wavelengths can provide practical advantages, but may also lead to increased diffraction. Diffuse optical tomography (DOT) is an emerging medical imaging modality, which makes use of near-infrared light for imaging sensitive regions of the body. It is nonionizing and can produce high-resolution images of tissue several centimeters below the surface of the skin. However, light at this wavelength ($\sim 1\mu\text{m}$) interacts strongly with biological tissue and undergoes significant optical scattering. The incident light is diffused through the tissue and the transmitted signal is often measured on the same side of the imaging region as the incident light. The measured signal can be used to reconstruct the object but a model of the sporadic photon propagation must be included in the inversion algorithm.

The rays are no longer straight and the path taken by a specific ray can no longer be defined. Instead, the distribution of the scattered intensity is simulated and used to create a weighted imaging region in which pixels involved in a higher number of scattering events are given a larger weight. An example of sporadic photon migration is demonstrated by

the diffusive random-walk simulation shown in Fig. 6.1. A variety of techniques exist for defining the projections once the imaging region has been weighted. Scattered ray paths can be chosen pseudo-randomly and used to form the distribution of projected intensities. Straight lines can also be conceptualized as if the emitter and probe were on opposite sides of the imaging region. The method for reconstruction must simply account for the contribution of a pixel to a projected ray in whatever manner the ray is defined. The definition of the ray must remain consistent as it is used to iteratively reconstruct the imaging object. The ART reconstruction algorithms can then be applied.

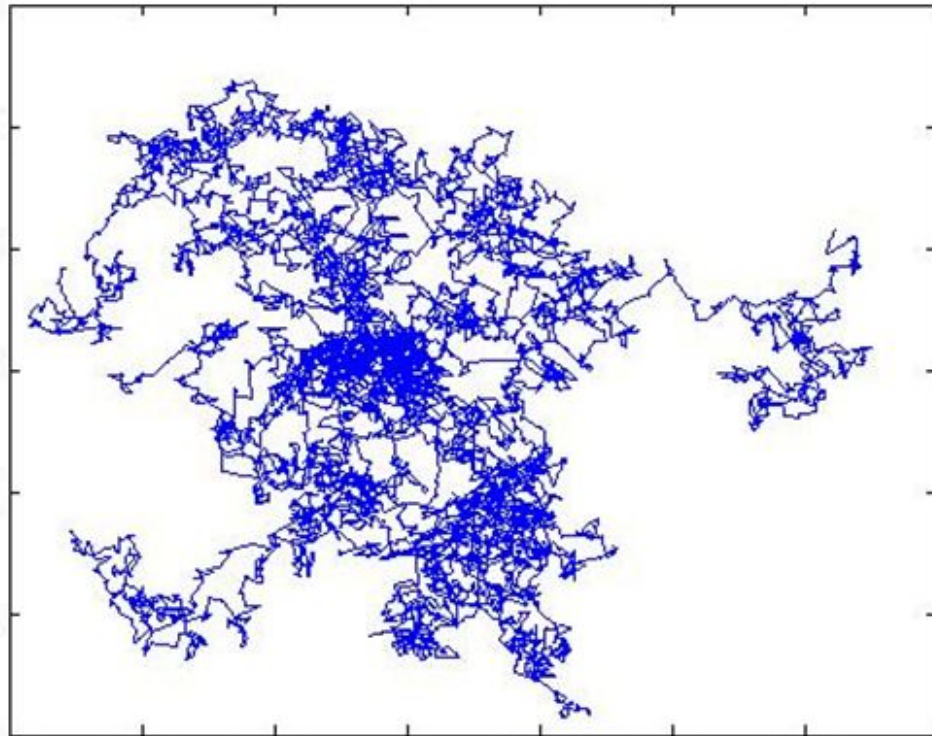


Fig. 6.1. A diffusive random-walk simulation demonstrating sporadic photon migration. Photons are given an initial position at the origin and a scattering angle and distance is then selected pseudo-randomly. The position of the photon is then updated and the process repeats until the photon is absorbed based on a weighted probability. Another photon is then launched until the algorithm terminates. This simulation demonstrates the nature of diffuse tomography in which the rays are no longer straight and the paths taken by projections are not well defined.

Diffusive projections offer several options for reconstruction and rely on the usual matrix methods to solve. The accuracy of the reconstruction, however, is heavily influenced by the model used to simulate the optical scattering. An accurate representation of the distribution of scattered intensities is crucial to the success of diffusive reconstruction methods. Since the path taken by any one ray is too difficult to simulate, a statistical Monte Carlo approach is adopted in which the accuracy of the model improves as the number of rays is increased. Thousands of simulated rays are included in the model and the locations of scattering events are recorded. The number of scattering events occurring at each coordinate is normalized and used to weight the imaging region. The algorithm used to run the Monte Carlo simulation and produce a weighted grid is relatively simple. The versatility offered by this approach is the way in which the directions of scattered photons are chosen. A few common phase function techniques, often used in DOT, are presented in the following chapter, as well as a scattering technique which utilizes Mie theory in its selection of a photon propagation angle.

The data collected during DOT are one-sided and sparse. The tomographic techniques developed during this research are therefore very applicable to DOT and other diffusive or highly scattering tomographic methods. The developed algorithms and initialization techniques could help to improve the image quality of diffusive tomography. A more advanced understanding of photon propagation in tissue could also improve imaging capabilities. The Monte Carlo techniques currently used in DOT rely on statistical methods and phase functions or on spherical Mie scattering. Much of the optical scattering, which occurs in cells, however, is caused by mitochondria and other intracellular organelles for which a spherical approximation may not be sufficiently accurate. Cell membranes and distorted cell nuclei can also acquire an elongated shape and may be more accurately described as being spheroidal. For this reason a novel Monte Carlo technique has been developed, which utilizes the optical scattering properties of spheroidal particles to determine scattering di-

rections. The method is presented in a paper, which comprises the following chapter, and is suggested to be a more physical approach to cellular scattering than current Monte Carlo techniques. Advanced scattering models such as these could lead to an improved description of diffusive photon migration in biological tissue. Improved Monte Carlo algorithms and research into accurate tomographic methods for reconstructing sparse data could lead to advances in the imaging capabilities of DOT and other diffusive imaging modalities.

CHAPTER 7

A SPHEROIDAL SCATTERING TECHNIQUE FOR SIMULATING DIFFUSE
PHOTON MIGRATION IN OPTICAL TOMOGRAPHY OF BIOLOGICAL TISSUE¹

A Monte Carlo method derived from optical scattering signatures of spheroidal particles is presented for modeling diffuse photon migration in biological tissue. The scattering solution is described using a separation of variables approach and numerical results of scattering simulations are presented. A Monte Carlo algorithm is then developed, which utilizes the scattering model to determine successive photon trajectories. The results of simulations performed using this algorithm, including three-dimensional models of scattered intensities and optical diffusion in virtual tissue, are presented and discussed. The results of additional Monte Carlo simulations performed using isotropic randomization, Henyey-Greenstein phase functions, and spherical Mie scattering are included for comparison. Linear intensity profiles are extracted from the diffusion models and compared. The feasibility of advanced scattering simulations as a diagnostic tool is addressed pertaining to the ability to distinguish specific cellular structures found in the diffused signal. Cell nuclei, which are roughly spherical when healthy, can become deformed in the earliest stages of certain cancers and their elongated shape could potentially be modeled as a prolate spheroid. Results from the Monte Carlo simulations are used to investigate the possibility of detecting large concentrations of spheroidal particles in otherwise spherical distributions, indicating the presence of unhealthy cells. The presented technique is proposed to be a more physical description of photon migration than existing phase function methods. The potential applications of the model and its importance to diffuse optical tomography are discussed.

7.1. Introduction

Throughout the history of optical tomography, emerging technological developments

¹Coauthored by Timothy E. Doyle.

have expanded the capabilities of existing imaging modalities and have broadened their use in a variety of fields. Medical applications of tomography are well known and the use of x-rays and other light sources for diagnostic purposes constitutes the conventional application of computed tomography (CT).

Modern diagnostic optics began with the advent of Röntgen rays (x-rays) in 1895 [96] and was revolutionized in 1971 by Hounsfield and the introduction of medical CT [2]. This allowed for the creation of reconstructed images, which provided more information than unidirectional projections. Images formed by an attenuated light source continue to be widely used in medical diagnostics and low-energy x-rays are typically found in most forms of CT, including mammography. As tomography usage increased, additional imaging modalities were developed, which exhibited specific advantages. The use of near-infrared light, for example, does not carry the same concerns regarding radiation exposure as does x-ray usage. This is particularly important when imaging vital or sensitive organs.

The use of nonionizing radiation in medical imaging has seen rapid expansion over the last few decades. The use of visible light for detecting breast lesions was first proposed in 1929 but had to be temporarily abandoned because the required intensities were causing the patient's skin to overheat [97]. Interest in using near-visible wavelengths for tomographic purposes was regenerated as technological advances provided for new applications. The introduction of video cameras allowed for the inclusion of spectral analysis [98] and methods such as diaphanography [99] and breast thermography were made possible by sensitivities in the infrared region. The success of these and other so-called diffusive techniques revived interest in near-infrared imaging and eventually led to the development of diffuse optical tomography, an emerging method for use in breast cancer detection [100].

Diffuse optical tomography (DOT) is an emerging modality, which has recently been applied to the imaging of breast [101], brain [102], and prostate cancer [9], as well as the mapping of brain activity [103]. The method utilizes near-infrared light which, due to its

nonionizing nature, provides opportunities for high-resolution imaging of sensitive regions of the body. However, light at these wavelengths ($\sim 1\mu\text{m}$) interacts strongly with biological tissue and significant optical scattering occurs, leading to diffusion of the incident light. Optical scattering and absorption in the body can provide important physiological information such as the oxygen saturation [104] and hemoglobin levels of blood [105], however they also create a complex imaging configuration in which the path taken by a given ray is not well defined. The creation of accurate tomographic reconstructions from this diffused signal requires a simulated description of the resulting sporadic photon migration. Optical scattering in tissue is a complex problem, which is not fully understood and improvements to existing models could provide opportunities for the advancement of current imaging capabilities. This paper presents a Monte Carlo technique for simulating diffuse photon migration using the optical scattering solution for spheroidal particles.

The potential of this approach is derived from primary features of cellular structure. Mitochondria are typically spheroidal in shape [106] and are responsible for a significant fraction of the optical scattering which occurs in cells [107–110]. It has been suggested that roughly 55% of the elastic light scattering at high angles ($>40^\circ$) comes from intracellular structures, of which a significant amount is attributed to cytoplasmic structures, such as mitochondria [111]. This is particularly true at near-infrared wavelengths, which are roughly equivalent to the typical micron-order diameters of mitochondria [112]. Cells themselves can exhibit spheroid-like shapes and the highly scattering cell nucleus, more spherical in healthy cells, can become deformed or elongated during the early stages of cancer [113]. A considerable amount of the total optical scattering, which occurs in the cell, can therefore be attributed to spheroid-like objects, thereby forming the theoretical basis for this model. Current Monte Carlo simulations used in DOT often rely on phase functions, which statistically determine scattering directions based on known macroscopic properties of the tissue [114]. It is proposed that the presented model, which relies on a knowledge of intracel-

lular structure, as well as an optical scattering solution derived from first principles, is a more physical approach to the problem, which could provide a more accurate description of diffuse light propagation in biological tissue. This in turn could lead to more accurate tomographic reconstructions using diffusive imaging techniques.

The spheroidal scattering solution used to create the Monte Carlo algorithm is presented and described in detail. The design of the Monte Carlo algorithm itself is then discussed and the results of simulated diffusive photon migration using this algorithm are presented including three-dimensional models of the scattered intensities. The results of additional Monte Carlo simulations, based on isotropic randomization, Henyey-Greenstein phase functions, and spherical Mie scattering, are included for comparison. Linear intensity profiles are extracted from the diffusion models and compared. The feasibility of using advanced scattering simulations as a diagnostic tool is addressed as it pertains to the ability to distinguish cellular structures evident in the diffused signal, specifically quasispherical and deformed spheroidal. Results from the Monte Carlo models are used to simulate the possibility of detecting large concentrations of spheroidal particles in normally spherical particulate distributions, potentially indicating the presence of unhealthy cells. The importance of the continual development and advancement of photon migration models of this type is discussed.

7.2. Spheroidal Scattering

The spheroidal scattering solution used in the development of the Monte Carlo algorithm follows a separation of variables approach. This technique has been used to model spheroidal scattering by a number of authors [115,116], but perhaps most notably by Asano and Yamamoto [117] who examined the problem in considerable detail. A solution is developed in spheroidal coordinates, which satisfies Maxwell's equations and the relevant boundary conditions.

7.2.1. Scattering Configuration

It is assumed that a linearly-polarized, monochromatic, electromagnetic plane wave is incident on a spheroidal particle embedded in a medium. The spheroid and medium are assumed to be both homogenous and isotropic, but with different indices of refraction. The system is assumed to be nonconducting, nonmagnetic, and electrically neutral. The time-dependent component of the electromagnetic field is assumed to be harmonically oscillatory and hence, can be expressed in the form $e^{-i\omega t}$. In the absence of source charges the static Maxwell equations can be written as [118]

$$\begin{aligned}\nabla \cdot \mathbf{E} &= 0, \\ \nabla \cdot \mathbf{H} &= 0, \\ \nabla \times \mathbf{E} &= ik_0 \mathbf{H}, \\ \nabla \times \mathbf{H} &= -ik_0 \mathcal{H}^2 \mathbf{E},\end{aligned}\tag{7.1}$$

where the notation of Asano and Yamamoto has been used in which

$$k_0 = \frac{\omega}{c} = \frac{2\pi}{\lambda_0},\tag{7.2}$$

$$\mathcal{H} = \varepsilon\mu + i\frac{4\pi\sigma\mu}{\omega},\tag{7.3}$$

and

$$k = k_0 \mathcal{H}.\tag{7.4}$$

In these expressions k_0 represents the wavenumber in vacuum and λ_0 the corresponding wavelength. The degree of refraction and absorption caused by the medium are described by the real and imaginary parts of the complex index of refraction \mathcal{H} at angular frequency ω . The electrical permittivity, permeability, and conductivity of the medium are defined by ε , μ , and σ respectively.

The Maxwell equations can be combined to form wave equations, which can be solved using a technique developed by Stratton [118]. Since the electric and magnetic fields are

related through vector operations, a substitution yields the result

$$\nabla \times (\nabla \times \mathbf{E}) = ik_0(\nabla \times \mathbf{H}) = k^2 \mathbf{E}. \quad (7.5)$$

The vector identity

$$\nabla \times (\nabla \times \mathbf{A}) = \nabla(\nabla \cdot \mathbf{A}) - \nabla^2 \mathbf{A} \quad (7.6)$$

can then be used to establish the additional relationship

$$\nabla \times (\nabla \times \mathbf{E}) = -\nabla^2 \mathbf{E}, \quad (7.7)$$

which results in the vector wave equation for the electric field:

$$\nabla^2 \mathbf{E} + k^2 \mathbf{E} = 0. \quad (7.8)$$

Likewise, an additional substitution leads to

$$\nabla \times (\nabla \times \mathbf{H}) = -ik_0 \mathcal{H}^2 (\nabla \times \mathbf{E}) = k^2 \mathbf{H}. \quad (7.9)$$

The use of the vector identity results in the expression

$$\nabla \times (\nabla \times \mathbf{H}) = -\nabla^2 \mathbf{H}, \quad (7.10)$$

which provides a vector wave equation for the magnetic field:

$$\nabla^2 \mathbf{H} + k^2 \mathbf{H} = 0. \quad (7.11)$$

The incident, scattered, and transmitted wave fields must then satisfy Eqs. (7.8) and (7.11). The boundary conditions imposed on the solution require the normal and tangential components of \mathbf{E} and \mathbf{H} be continuous across the surface of the spheroid. Stratton suggests that vector wave equations may be solved by finding solutions of the associated scalar wave equations [118]. Vector solutions can then be obtained from the scalar solutions using vector operations as will be demonstrated in section 7.2.3. A brief introduction to the spheroidal coordinate system is given first in order to explain the meaning of coordinate variables used in subsequent sections.

7.2.2. Spheroidal Coordinates

The scalar version of Eqs. (7.8) and (7.11), from which vector solutions can be found, is given by

$$\nabla^2 \psi + k^2 \psi = 0. \quad (7.12)$$

This is the familiar wave equation, which is separable in 11 coordinate systems including prolate and oblate spheroidal [119]. The conventions of prolate spheroidal coordinates, as demonstrated in Fig. 7.1, are similar to those of spherical coordinates. A radial coordinate, assigned to ξ , is included, which describes the distance from a given point to the origin. The azimuthal angle is given by ϕ and the inclination angle by η . Surfaces of constant ξ form ellipsoids and surfaces of constant η form hyperboloids. The prolate spheroidal coordinate variables are defined over the following ranges:

$$-1 \leq \eta \leq 1, \quad 1 \leq \xi < \infty, \quad 0 \leq \phi \leq 2\pi. \quad (7.13)$$

The axis of revolution is chosen to be the z axis from which η is measured. A value of 1 indicates that η is directed along the positive z axis, a value of -1 indicates it is directed along the negative z axis, and 0 indicates it is orthogonal to the z axis. The incident plane is defined as the plane, which includes the z axis and the incident radiation. The x axis, from which ϕ is measured, is chosen to lie in the incident plane. The y axis is defined to be orthogonal to the x and z axes in the usual right-handed system. The direction of the incident light is given by ζ , which exists over the range

$$0 \leq \zeta \leq \pi, \quad (7.14)$$

and is measured in radians from the z axis. A value of 0 indicates the light is directed along the positive z axis and will first encounter the spheroid at the point where $\eta = -1$. A value of -1 indicates the incident light is directed along the negative z axis and will initially reach the spheroid at the point where $\eta = 1$. Spheroidal coordinates are further explained in Appendix C.

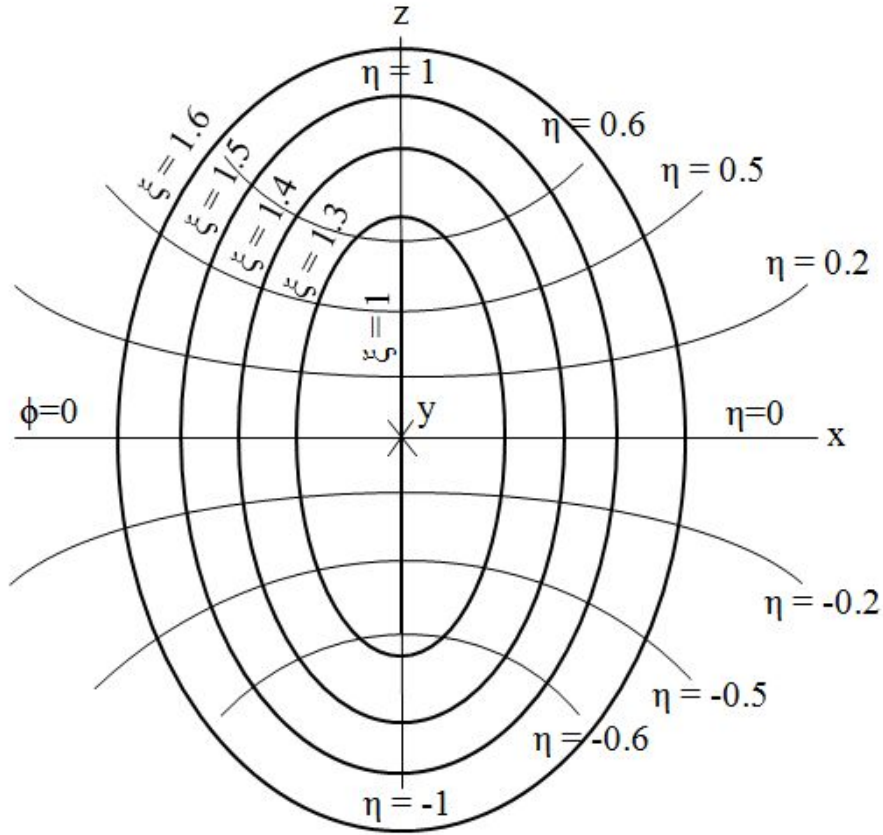


Fig. 7.1. The prolate spheroidal coordinate system.

7.2.3. Spheroidal Wave Functions

The separation of variables technique used to solve the scalar wave equation results in three ordinary differential equations (ODEs), one in each of the coordinate variables. The solution of the partial differential equation (7.12) is assumed to be the product of the separated solutions and can be expressed as

$$\psi = S(\eta)R(\xi)P(\phi). \quad (7.15)$$

The solutions of the scalar wave equation expressed in spheroidal coordinates are known as spheroidal wave functions. The separated ODE solutions constitute their radial and angular components and can be expressed as expansions of other special functions. Due to the azimuthal symmetry of spheroids, the solutions in ϕ are simply sinusoidal and take the

form

$$P(\phi) = e^{im\phi}, \quad (7.16)$$

where m is an integer, which can be restricted to zero or positive values such that

$$m = 0, 1, 2, 3, \dots$$

The equation, which results in η is given by [117]

$$\frac{d}{d\eta} \left[(1 - \eta^2) \frac{dS_{mn}(\eta)}{d\eta} \right] + \left(\lambda_{mn} - c^2 \eta^2 - \frac{m^2}{1 - \eta^2} \right) S_{mn}(\eta) = 0, \quad (7.17)$$

where c is defined as the product of the semifocal distance and the wavenumber. The focal distance of the spheroid is given by d and therefore

$$c = \frac{1}{2}kd = \frac{\pi d}{\lambda}. \quad (7.18)$$

The term λ_{mn} refers to the eigenvalue of order m and degree n for which the solution is continuous and

$$n = m, m+1, m+2, m+3, \dots$$

The solutions of Eq. (7.17) are known as the prolate spheroidal angular functions and can be expanded in terms of the associated Legendre functions of the first kind as follows:

$$S_{mn}(\eta) = \sum_{r=0,1}^{\infty} d_r^{mn} P_{m+r}^m(\eta). \quad (7.19)$$

The prime indicates a summation over even values if $n - m$ is even and over odd values if $n - m$ is odd. The d_r^{mn} represent expansion coefficients, which can be obtained using two expressions given by Flammer [119]. The recursion formula for expansion coefficients is given by

$$\frac{(2m+r+2)(2m+r+1)c^2}{(2m+2r+3)(2m+2r+5)} d_{r+2}^{mn} + \left[(m+r)(m+r+1) - \lambda_{mn} + \frac{2(m+r)(m+r+1) - 2m^2 - 1}{(2m+2r-1)(2m+2r+3)} c^2 \right] d_r^{mn} + \frac{r(r-1)c^2}{(2m+2r-3)(2m+2r-1)} d_{r-2}^{mn} = 0, \quad (7.20)$$

and the normalizing relations are defined as

$$\sum_{r=0}^{\infty} \frac{(-1)^{\frac{r}{2}} (r+2m)!}{2^r \left(\frac{r}{2}\right)! \left(\frac{r+2m}{2}\right)!} d_r^{mn} = \frac{(-1)^{\frac{n-m}{2}} (n+m)!}{2^{n-m} \left(\frac{n-m}{2}\right)! \left(\frac{n+m}{2}\right)!} \quad (7.21)$$

for $(n-m)$ even and

$$\sum_{r=1}^{\infty} \frac{(-1)^{\frac{r-1}{2}} (r+2m+1)!}{2^r \left(\frac{r-1}{2}\right)! \left(\frac{r+2m+1}{2}\right)!} d_r^{mn} = \frac{(-1)^{\frac{n-m-1}{2}} (n+m+1)!}{2^{n-m} \left(\frac{n-m-1}{2}\right)! \left(\frac{n+m+1}{2}\right)!} \quad (7.22)$$

for $(n-m)$ odd. The eigenvalues can be found from the following transcendental equation:

$$U1(\lambda_{mn}) + U2(\lambda_{mn}) = 0, \quad (7.23)$$

where

$$U1(\lambda_{mn}) = \gamma_{n-m}^m - \lambda_{mn} - \frac{\beta_{n-m}^m}{\gamma_{n-m-2}^m - \lambda_{mn} - \frac{\beta_{n-m-2}^m}{\gamma_{n-m-4}^m - \lambda_{mn} - \frac{\beta_{n-m-4}^m}{\dots}}} \quad (7.24)$$

and

$$U2(\lambda_{mn}) = - \frac{\beta_{n-m+2}^m}{\gamma_{n-m+2}^m - \lambda_{mn} - \frac{\beta_{n-m+4}^m}{\gamma_{n-m+4}^m - \lambda_{mn} - \frac{\beta_{n-m+6}^m}{\dots}}} \quad (7.25)$$

In this expression

$$\gamma_r^m = (m+r)(m+r+1) + \frac{1}{2}c^2 \left[1 - \frac{4m^2 - 1}{(2m+2r-1)(2m+2r+3)} \right] \quad (7.26)$$

and

$$\beta_r^m = \frac{r(r-1)(2m+r)(2m+r-1)c^4}{(2m+2r-1)^2(2m+2r-3)(2m+2r+1)}. \quad (7.27)$$

The equation, which results in ξ is given by [117]

$$\frac{d}{d\xi} \left[(\xi^2 - 1) \frac{dR_{mn}(\xi)}{d\xi} \right] - \left[\lambda_{mn} - c^2 \xi^2 + \frac{m^2}{(\xi^2 - 1)} \right] R_{mn}(\xi) = 0. \quad (7.28)$$

The solutions of Eq. (7.28) are known as the prolate spheroidal radial functions. The first type can be expressed in terms of the spherical Bessel functions as

$$R_{mn}^{(1)}(\xi) = \frac{1}{\left[\sum_{r=0,1}^{\infty} \frac{(r+2m)!}{r!} d_r^{mn} \right]} \left[\frac{\xi^2 - 1}{\xi^2} \right]^{\frac{m}{2}} \sum_{r=0,1}^{\infty} i^{r+n-m} d_r^{mn} \frac{(r+2m)!}{r!} j_{m+r}(c\xi). \quad (7.29)$$

Expansions of the second type of radial function ($R^{(2)}$) are more difficult to generate. Several expressions for $R^{(2)}$ have been developed using various approaches, however they are typically accurate for large values of ξ only. The function is nonfinite at the origin and accurately describing its behavior for small values of ξ can be very challenging. A number of techniques for modeling the function numerically have been proposed in the literature with varying accuracies. The authors suggest the method developed by Kirby, which initializes an algorithm using the standard radial expansion in terms of the spherical Neumann functions [120]. The technique uses the expression

$$R_{mn}^{(2)}(\xi) = \frac{1}{\left[\sum_{r=0,1}^{\infty} \frac{(r+2m)!}{r!} d_r^{mn} \right]} \left[\frac{\xi^2 - 1}{\xi^2} \right]^{\frac{m}{2}} \sum_{r=0,1}^{\infty} i^{r+n-m} d_r^{mn} \frac{(r+2m)!}{r!} y_{m+r}(c\xi) \quad (7.30)$$

to locate a value of $R^{(2)}$ for some large ξ . This beginning value can be made sufficiently accurate by increasing the value of ξ . From this selected coordinate, an iterative Bulirsch-Stoer algorithm is implemented, which integrates (7.28) backwards towards the origin in order to find the values of $R^{(2)}$ at small ξ . This approach is somewhat intensive computationally, yet produces unprecedentedly accurate results, which proved to be superior during initial testing.

7.2.4. Scattering Solution

The solutions of the scalar wave equation (7.12) can be expressed as the product of the spheroidal radial functions, the spheroidal angular functions, and a harmonic azimuthal term. The scalar spheroidal wave functions can be either even,

$$\psi_{emn}^{(j)}(\eta, \xi, \phi) = S_{mn}(\eta) R_{mn}^{(j)}(\xi) \cos m\phi, \quad (7.31)$$

or odd,

$$\psi_{omn}^{(j)}(\eta, \xi, \phi) = S_{mn}(\eta)R_{mn}^{(j)}(\xi)\sin m\phi, \quad (7.32)$$

depending upon the azimuthal behavior. In these expressions the subscript j takes the value 1 inside the spheroid and 3 outside the spheroid. The composite function $R^{(3)}$ is given by

$$R_{mn}^3(\xi) = R_{mn}^1(\xi) + iR_{mn}^2(\xi). \quad (7.33)$$

The first radial function is used to describe the field within the spheroid because it is necessarily finite at the origin. From these scalar solutions, vector wave functions can be formed as follows:

$$\mathbf{M}_{(k)mn}^{(j)} = \nabla \times (\mathbf{r}\psi_{(k)mn}^{(j)}) \quad (7.34)$$

and

$$\mathbf{N}_{(k)mn}^{(j)} = \frac{1}{k}(\nabla \times \mathbf{M}_{(k)mn}^{(j)}). \quad (7.35)$$

In this expression j takes the value 1 or 3 and k represents either e or o indicating an even function or an odd function. The vector \mathbf{r} is the position vector, which in spheroidal coordinates is a function of η , ξ , and ϕ . These are the vector spheroidal wave functions. The \mathbf{E} and \mathbf{H} fields, which satisfy the vector wave equations (7.8) and (7.11) can be expressed as infinite sums of $\mathbf{M}_{mn}(\eta, \xi, \phi)$ and $\mathbf{N}_{mn}(\eta, \xi, \phi)$.

Flammer developed the expansion of a plane wave, propagating in the x-z plane at an angle ζ from the z axis, in terms of the prolate spheroidal vector wave functions [119]. The incident field can be expressed as:

$$\mathbf{e}_y = -e^{-ik(xs\sin\zeta + z\cos\zeta)} \sum_{m=0}^{\infty} \sum_{n=m}^{\infty} i^n [g_{mn}(\zeta)\mathbf{M}_{emn}^{(1)}(\eta, \xi, \phi) + if_{mn}(\zeta)\mathbf{N}_{omn}^{(1)}(\eta, \xi, \phi)], \quad (7.36)$$

where the expansion coefficients are given by

$$f_{mn}(\zeta) = \frac{4m}{\Lambda_{mn,r=0,1}} \sum_{r=0,1}^{\infty} \frac{d_r^{mn}}{(r+m)(r+m+1)} \frac{P_{m+r}^m(\cos\zeta)}{\sin\zeta} \quad (7.37)$$

and

$$g_{mn}(\zeta) = \frac{2(2 - \delta_{0m})}{\Lambda_{mn}} \sum_{r=0,1}^{\infty} \frac{d_r^{mn}}{(r+m)(r+m+1)} \frac{dP_{m+r}^m(\cos \zeta)}{d\zeta} \quad (7.38)$$

with the normalization constant given by

$$\Lambda_{mn} = \sum_{r=0,1}^{\infty} \frac{2(r+2m)!}{(2r+2m+1)r!} (d_r^{mn})^2. \quad (7.39)$$

The incident wave of unit amplitude polarized in the TE (transverse electric) mode is described by [117]

$$\mathbf{E}^{(i)} = \sum_{m=0}^{\infty} \sum_{n=m}^{\infty} i^n [g_{mn}(\zeta) \mathbf{M}_{emn}^{(1)} + i f_{mn}(\zeta) \mathbf{N}_{omn}^{(1)}], \quad (7.40)$$

$$\mathbf{H}^{(i)} = \mathcal{H}^{(I)} \sum_{m=0}^{\infty} \sum_{n=m}^{\infty} i^n [f_{mn}(\zeta) \mathbf{M}_{omn}^{(1)} - i g_{mn}(\zeta) \mathbf{N}_{emn}^{(1)}]. \quad (7.41)$$

The scattered wave, which describes the field exterior to the spheroid is expressed as

$$\mathbf{E}^{(s)} = \sum_{m=0}^{\infty} \sum_{n=m}^{\infty} i^n [\beta_{mn} \mathbf{M}_{emn}^{(3)} + i \alpha_{mn} \mathbf{N}_{omn}^{(3)}], \quad (7.42)$$

$$\mathbf{H}^{(s)} = \mathcal{H}^{(I)} \sum_{m=0}^{\infty} \sum_{n=m}^{\infty} i^n [\alpha_{mn} \mathbf{M}_{omn}^{(3)} - i \beta_{mn} \mathbf{N}_{emn}^{(3)}]. \quad (7.43)$$

The transmitted wave, which describes the field on the interior of the spheroid is given by

$$\mathbf{E}^{(t)} = \sum_{m=0}^{\infty} \sum_{n=m}^{\infty} i^n [\delta_{mn} \mathbf{M}_{emn}^{(1)} + i \gamma_{mn} \mathbf{N}_{omn}^{(1)}], \quad (7.44)$$

$$\mathbf{H}^{(t)} = \mathcal{H}^{(II)} \sum_{m=0}^{\infty} \sum_{n=m}^{\infty} i^n [\gamma_{mn} \mathbf{M}_{omn}^{(1)} - i \delta_{mn} \mathbf{N}_{emn}^{(1)}]. \quad (7.45)$$

In each of these expressions the incident field is denoted by the superscript (i) , the scattered field by (s) , and the transmitted field by (t) . The superscript (I) refers to the medium surrounding the spheroid and (II) refers to the spheroid itself. The terms α , β , γ , and δ are the unknown scattering coefficients, which must be determined using the relevant boundary conditions. These can be written as

$$E_{\eta}^{(i)} + E_{\eta}^{(s)} = E_{\eta}^{(t)}, \quad (7.46)$$

$$E_{\phi}^{(i)} + E_{\phi}^{(s)} = E_{\phi}^{(t)}, \quad (7.47)$$

$$H_{\eta}^{(i)} + H_{\eta}^{(s)} = H_{\eta}^{(t)}, \quad (7.48)$$

$$H_{\phi}^{(i)} + H_{\phi}^{(s)} = H_{\phi}^{(t)}. \quad (7.49)$$

The solution must satisfy the boundary conditions for each point on the surface of the spheroid ($\xi = \xi_0$) simultaneously. Asano and Yamamoto accomplished this by using the orthogonality properties of the spheroidal functions. They also included series expansions for the resulting integrals [117]. The cumulative expression is a large matrix equation, which can be used to solve for the unknown scattering coefficients. The scattered field can then be determined at any given coordinate. Examples of directional scattering, back scattering, and isotropic scattering are shown in Fig. 7.2.

7.2.5. Scattering Parameters

As part of the presented research, scattering solutions were acquired for varying incident angles and stored in a database. The incident angle was set to a specific value and the solution was computed using the presented solution. The simulated intensity of the scattered wave on the surface of the spheroid was stored as a two-dimensional image, an example of which is given in Fig. 7.3. The incident angle was advanced by 0.03 radians (1.72°) from 0 to $\frac{\pi}{2}$, creating a discretized representation of all possible incident orientations. Angles greater than $\frac{\pi}{2}$ did not need to be computed due to the symmetry of the spheroid. Values of $\mathcal{H}^{(I)}=1.2$ and $\mathcal{H}^{(II)}=1.33$ were used as the refractive indices of the medium and spheroid respectively. The assumption that the spheroid and medium are non-conducting results in these values being real. The surface of the spheroid was described by $\xi_0=1.2$, which corresponds to a spheroidal eccentricity of 0.83. Values of $c=2.0$ and $c=3.0$ were used for the medium and spheroids, respectively. The spatial units were scaled to the interfocal distance such that $d=1.0$. These parameters were chosen in order to simulate the conditions found in optical scattering of biological tissue. The simulated wavelength of the

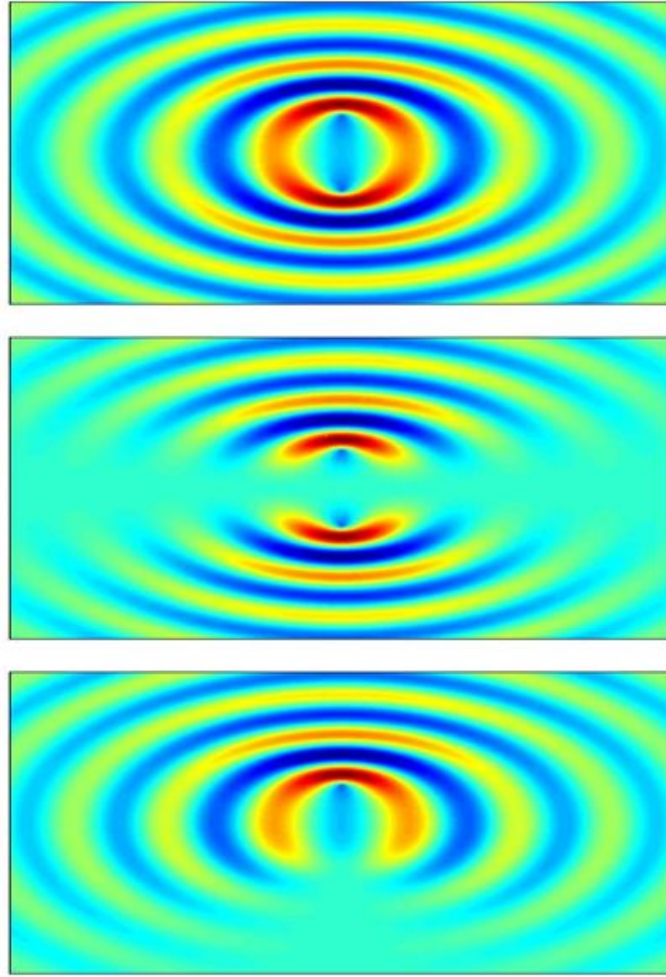


Fig. 7.2. Simulations of the scattered wave fields measured away from a spheroidal particle. The top image shows isotropic scattering in which each direction is equally probable. The center image demonstrates a process called directional scattering in which the scattered field is predominately oriented along a specific direction. The lower image shows back scattering in which the majority of the incident wave is scattered back along the incident angle. The images are composed of the spheroidal wave functions.

incident light was comparable to the semi-major axis of the spheroids. This is analogous to the $\sim 0.9\mu\text{m}$ wavelength of near-infrared light used in diffuse optical tomography (DOT) and the $\sim 1.0\mu\text{m}$ diameters of cell mitochondria. Additional scattering images for varying angles of incidence are shown in Appendix B. These scattering solutions were implemented in a Monte Carlo algorithm designed to simulate sporadic photon migration in tissue.

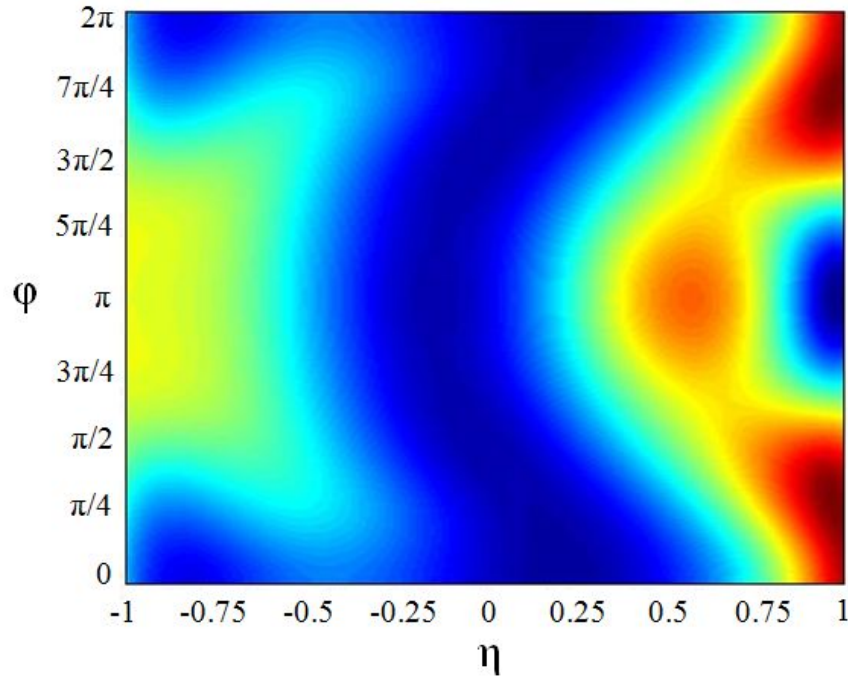


Fig. 7.3. The scattered intensity of light measured on the surface of a spheroid for the case of $\zeta=0.3$. The image was generated using the presented spheroidal scattering solution and corresponds to light incident on the spheroid at an angle of 17.76° from the z axis.

7.3. Photon Migration Models in DOT

In diffusive tomographic imaging techniques, the incident light is diffused throughout the imaging region. In order to create accurate reconstructions from the acquired data, accurate simulations must be included, which model the diffused intensity of the light at each point in the image grid. The intensity of diffused light is represented computationally using Monte Carlo simulations in which virtual photons are launched individually into virtual tissue. The photons are given an initial direction and the distance to a scattering site is determined. The position of the photon is updated as the location of the new scattering site. The relative intensity of diffused light at a given location is represented by the number of photons, which have scattered from that location. Thus, each time a scattering site is determined, the intensity at that point is increased by a set increment. A new scattering direction is then determined and the process is repeated until the photon is absorbed. Mil-

lions of photons are typically launched in order to create a diffusion profile in which the intensity at a given point is represented by the number of photons, which were scattered at that point. The length of a step is typically determined using known mean-free path data. The scattering coefficient, μ_s , assumes an average value of $100 \frac{1}{cm}$ in biological tissue. The scattering mean-free path, the reciprocal of the scattering coefficient, is then $0.01 cm$ [114]. Likewise, the absorption of a photon is controlled by the absorption coefficient μ_a , which typically acquires a value of $0.1 \frac{1}{cm}$ in tissue. The average distance a photon travels before being absorbed is then $10 cm$. The absorption mean-free path is much larger ($1000x$) than the scattering mean-free path. For this reason biological tissue is often referred to as a highly-scattering medium or a turbid medium [114]. The method used to determine the scattering direction of a photon uniquely defines a specific Monte Carlo technique. In the presented research, spheroidal scattering solutions were used to determine the propagation directions of photons in the diffusion algorithm. The results are then compared in a subsequent section to conventional diffusion techniques, which can typically be classified in two groups, phase function methods and Mie scattering methods. These techniques are discussed here for comparison.

7.3.1. Phase Functions

The current techniques used to model optical diffusion in clinical DOT are dominated by a class of Monte Carlo algorithms known as phase function methods. These algorithms are a modified version of the random-walk motion in which the azimuthal angle is selected pseudo-randomly. The inclination angle, however, is weighted based on an analytic distribution, which is a function of the scattering anisotropy. The Henyey-Greenstein phase function is perhaps the most common and is given by the distribution [121]

$$p(\cos\theta) = \frac{1 - g^2}{2(1 + g^2 - 2g\cos\theta)^{\frac{3}{2}}}. \quad (7.50)$$

In this expression g represents the scattering anisotropy of the medium. A value of $g=1$ indicates complete forward scattering, 0 indicates isotropic scattering in which all directions are equally probable, and -1 indicates complete back scattering. Biological tissue is typically represented by a value of $g=0.9$ [114]. The application of an inverse distribution method (IDM) implies that η is sampled as

$$\cos\eta = \frac{1}{2g} \left[1 + g^2 - \left(\frac{1 - g^2}{1 - g + 2g\epsilon} \right)^2 \right] \quad (7.51)$$

if $g \neq 0$ and as

$$\cos\eta = 2\epsilon - 1 \quad (7.52)$$

if $g = 0$. In this expression ϵ is a pseudo-random number between 0 and 1. The azimuthal angle is chosen pseudo randomly in this technique by

$$\phi = 2\pi\epsilon. \quad (7.53)$$

The Rayleigh phase function is an approximation used when the wavelength of the incident light is much larger than the particle diameter. It is given by

$$R(\cos\eta) = \frac{3}{8}(1 + \cos^2\eta). \quad (7.54)$$

As mentioned previously, the distances between scattering events and the number of scattering events, which occur before a photon is absorbed, are typically controlled by the scattering and absorption coefficients of the material. These are determined experimentally from scattering and absorption cross sections and are used in most photon migration models.

7.3.2. Mie Scattering

Since the recent development of DOT and other NIR imaging modalities, a considerable amount of research has been conducted into the potential for improving existing Monte Carlo diffusion algorithms. The Henyey-Greenstein phase function is widely used

and its accuracy can be altered by the choice of physical parameters such as g , μ_s , and μ_a . The phase function was, however, originally developed for describing the attenuation of light by interstellar dust grains and does not include any histological information. Alternative methods have been proposed in which cells are modeled as spheres or collections of spheres. These methods are referred to as Mie scattering methods as they are derived from the Mie scattering solution of light incident on a spherical particle. The Mie theory and variations of the solution, which account for clusters of spheres (multiple scattering), have been described in the literature [122]. The Mie solution was generated during the presented research from the spheroidal scattering algorithm. The surface value of the spheroid was increased to $\xi_0 = 3.6$ resulting in an eccentricity of 0.28. This deformed spheroid closely resembled a sphere and was used to generate the spherical diffusion pattern for comparison with the diffusion patterns created by other techniques. The scattered intensity at the surface of the sphere is shown in Fig. 7.4.

7.3.3. Spheroidal Scattering

The Monte Carlo algorithm developed during the presented research is based on solutions of the spheroidal scattering problem. The algorithm includes physical parameters designed to simulate the interaction of near-infrared light and cell organelles. This technique is proposed to be a more physical representation of diffusive photon migration because it includes information about intracellular structures. Mitochondria are roughly spheroidal in shape and account for a significant amount of the optical scattering, which occurs in cells. The technique was used to simulate optical diffusion and results are presented and compared in a subsequent section.

The spheroidal Monte Carlo algorithm was designed in a similar manner to the other techniques. Photons were launched into the tissue with a given direction and the distance to a scattering site was determined using representative scattering coefficients. At each scattering site an incident angle ζ was chosen pseudo-randomly. A surface scattering profile

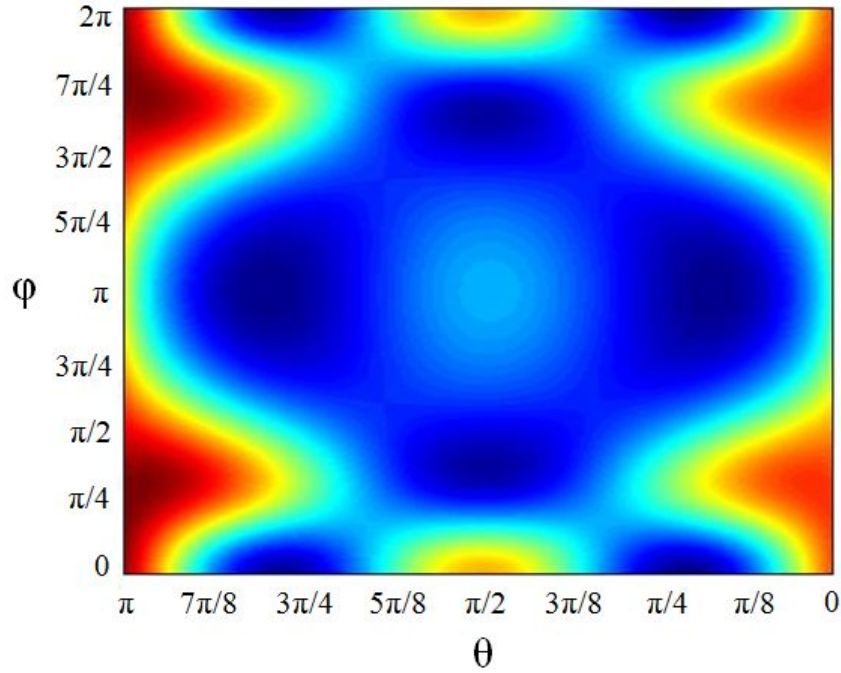


Fig. 7.4. The scattered intensity of light measured on the surface of a sphere. The image was generated by modifying the eccentricity of the spheroids in the presented scattering solution until they were approximately spherical. The symmetry and lack of dependence on the incident angle for a sphere suggests that the scattering solution and resulting simulations are accurate.

was then selected from the solution database, which corresponded to the chosen value of ζ . The surface scattering image for $\zeta=0$ is shown in Fig. 7.5. The values of the intensity at each point on the surface of the spheroid were then normalized and a scale was created in which the values were represented as a summation of all previous values. For points 1,2,3...N, the intensities were given by $I(1), I(2), I(3) \dots I(N)$. The scaled values were then given by

$$S(1) = I(1),$$

$$S(2) = I(1) + I(2),$$

$$\vdots$$

$$S(N) = I(1) + I(2) + I(3) + \dots I(N) = 1.0. \quad (7.55)$$

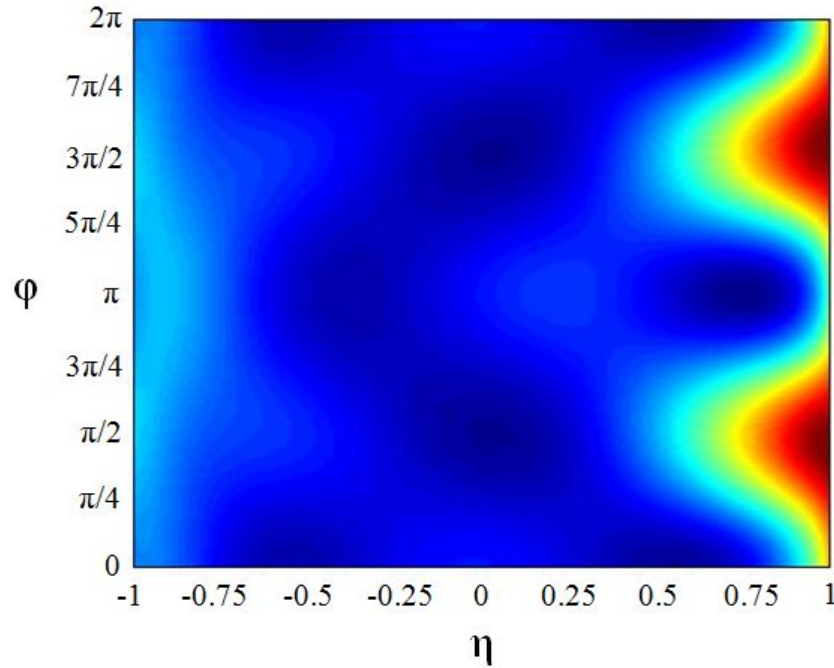


Fig. 7.5. The scattered intensity of light measured on the surface of a spheroid for the case of $\zeta=0$. The image was generated using the presented spheroidal scattering solution and corresponds to light incident on the spheroid along the z axis, the spheroid's axis of revolution.

A pseudo-random number is then selected between 0 and 1. The algorithm determines which scale value the random number is closest to and uses the corresponding values of η and ξ as the chosen scattering direction. This technique is similar to random walk, however, it biases the scattering direction toward the higher intensity angles found in the spheroidal scattering solution. The scattered angle was then used along with a free-path distance to update the position of the photon and the process was repeated until the photon was absorbed. Another photon was then launched until the algorithm terminated. Absorption was controlled by the absorption coefficient. Since spheroids lack the angular symmetry of spheres, coordinate transformations had to be performed at each scattering site. The incident angle is measured from the z axis, which is orthogonal to the surface of the tissue at the initial scattering location. After the first scattering event, however, the photons are

no longer directed along the z axis and the resulting scattering angles must be rotated into the global coordinate system. This process is demonstrated in Fig. 7.6. The intensity at each location in the imaging grid was represented by the number of scattering events that occurred at that location. Results of the simulated diffusion using spheroids are presented in the following section.

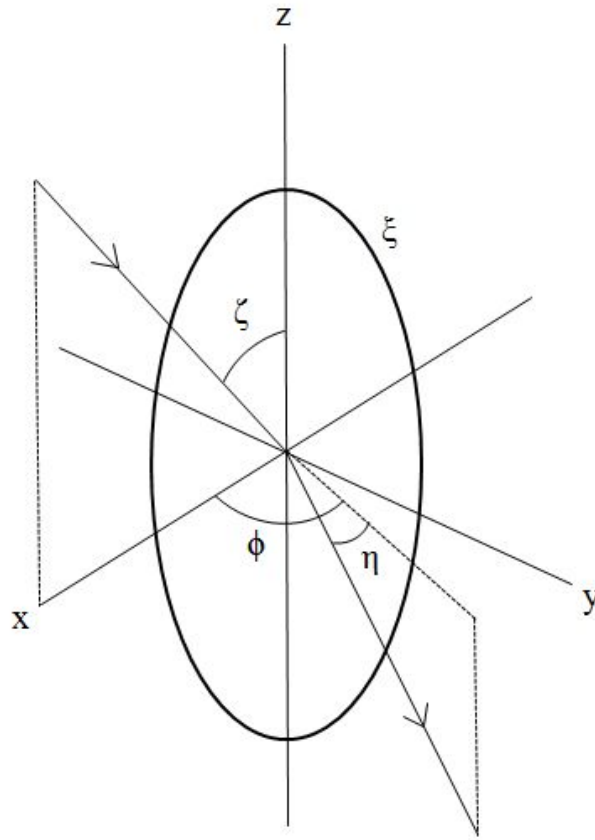


Fig. 7.6. A diagram of scattering events in the spheroidal coordinate system. The incident direction lies in the x - z plane and the incident angle ζ is measured from the z axis. Once a scattering direction is determined, it becomes the incident angle in a subsequent rotated spheroidal coordinate system. When a new scattering direction is determined, the coordinates must be rotated into the global coordinate system.

7.4. Results

Optical diffusion was simulated using isotropic (random-walk), phase function, Mie

scattering, and spheroidal scattering techniques. The resulting diffusion profiles are presented here for comparison and the importance of the results to improving photon migration models for use in DOT is discussed.

The Monte Carlo algorithms utilized in this research determined the location of successive scattering sites and increased the value of the intensity at the corresponding coordinates. The intensity at each point in the imaging grid was stored after each simulation and used to create diffusion profiles. The photons were incident at the origin and were assigned an initial direction along the $-z$ axis. Various cross-sectional views of the diffused intensity can be generated by specifying a plane in the imaging region defined by constant values of x , y , or z . An example of a diffusion profile is shown for isotropic scattering on the plane $y=0$ in Fig. 7.7. The intensities measured along the x and z axes are also shown in the figure. Plots such as these were used to quantitatively compare the results from varying diffusion simulations.

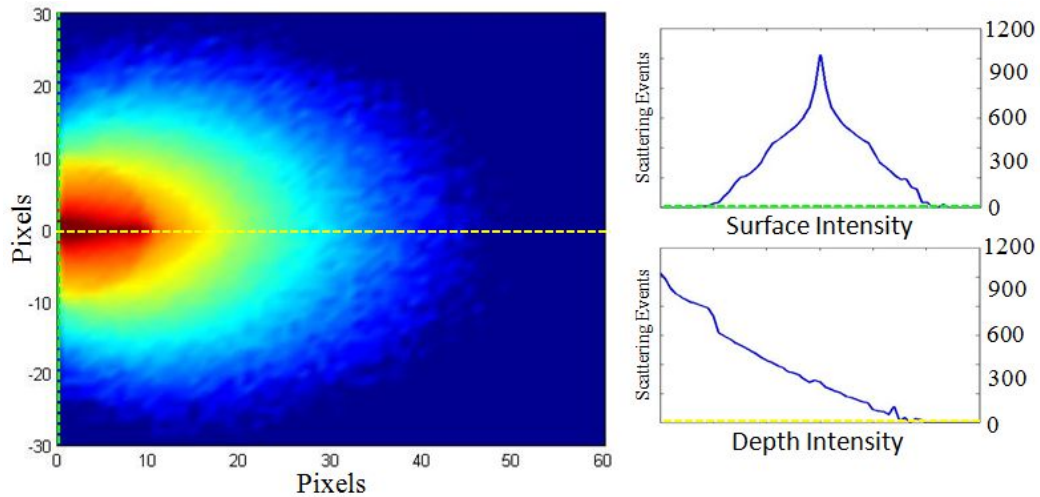


Fig. 7.7. A simulated diffusion profile along the plane $y=0$ using isotropic scattering. The image on the left shows the diffused intensity generated by a Monte Carlo algorithm. The images on the right show plots of the surface intensity (top), which is measured along the x axis and the depth intensity (bottom), which is measured along the z axis. Plots such as these are important in quantifying the differences between diffusion profiles.

Another view of the diffused intensity, which is of interest in medical applications, is the intensity along the surface of the tissue ($z=0$). In most diagnostic uses of DOT, probes are placed on the surface of the tissue and measurements are acquired of the reflected intensities. A simulated surface intensity profile is shown for isotropic scattering in Fig. 7.8.

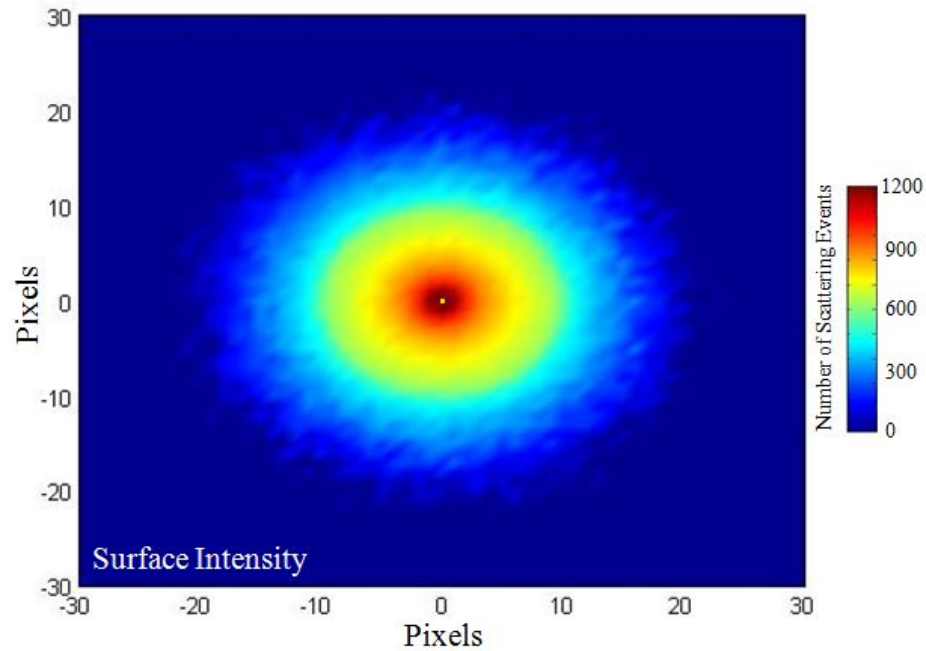


Fig. 7.8. Diffused intensity measured along the surface of the tissue. The accuracy of this simulation is of particular interest in medical applications such as DOT in which measurements are typically collected on the surface of the skin and used to create tomographic reconstructions of subdermal structure.

The profiles from multiple planes can be combined in a series of two-dimensional images to create a three-dimensional (3D) model of the diffused light. An example of this process is shown for isotropic scattering in Fig. 7.9. The azimuthal symmetry of the diffusion is evident in the image. A cross-sectional view of the model is shown in Fig. 7.10. The decrease in intensity, which occurs away from the incident point, is evident in the image.

Diffusion simulations were performed using isotropic, spherical, spheroidal, and phase function scattering based on the Henyey-Greenstein distribution. Tests were conducted

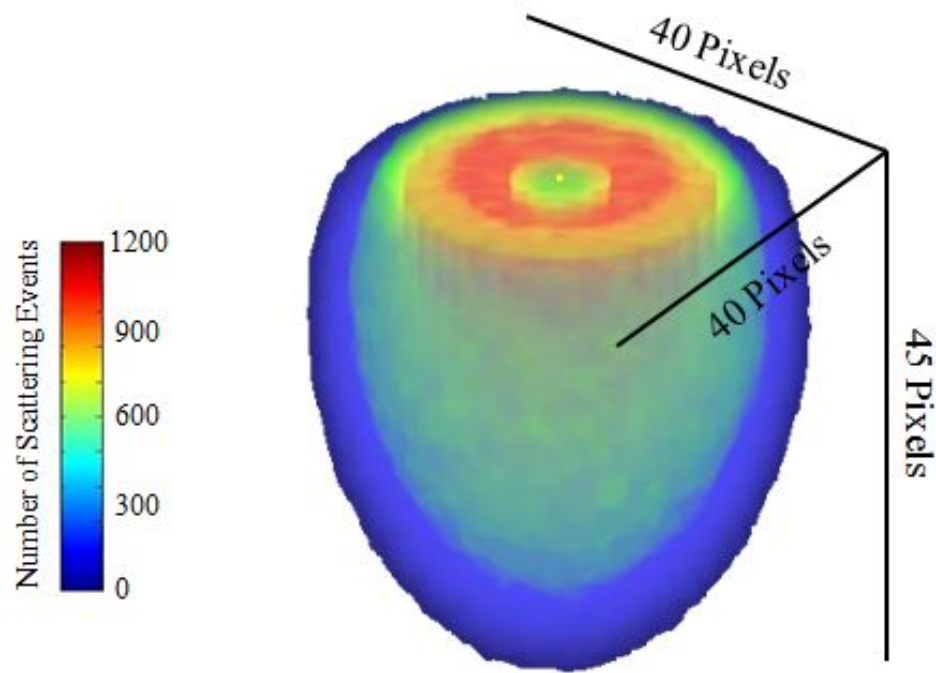


Fig. 7.9. A 3D model of optical diffusion in biological tissue. A series of 2D diffusion profiles were combined to create the image.

in order to determine whether or not the chosen scattering modality had an effect on the simulation results. All other parameters, such as those controlling absorption and path length, remained consistent across the various Monte Carlo algorithms. The results of simulated diffusion using each scattering technique are shown in Fig. 7.11. Plots of the depth intensity measured along the z axis in each of the four diffusion profiles are shown for comparison in Fig. 7.12. The differences between the intensities is immediately evident and demonstrates that the scattering mechanism used in Monte Carlo simulations of optical diffusion has a significant effect on the resulting intensities.

7.5. Discussion

The primary result of the presented research is the dependence, which diffusion simulations have on the scattering technique used in the algorithm. The presented simulations are based on physical parameters, which are generally representative of biological

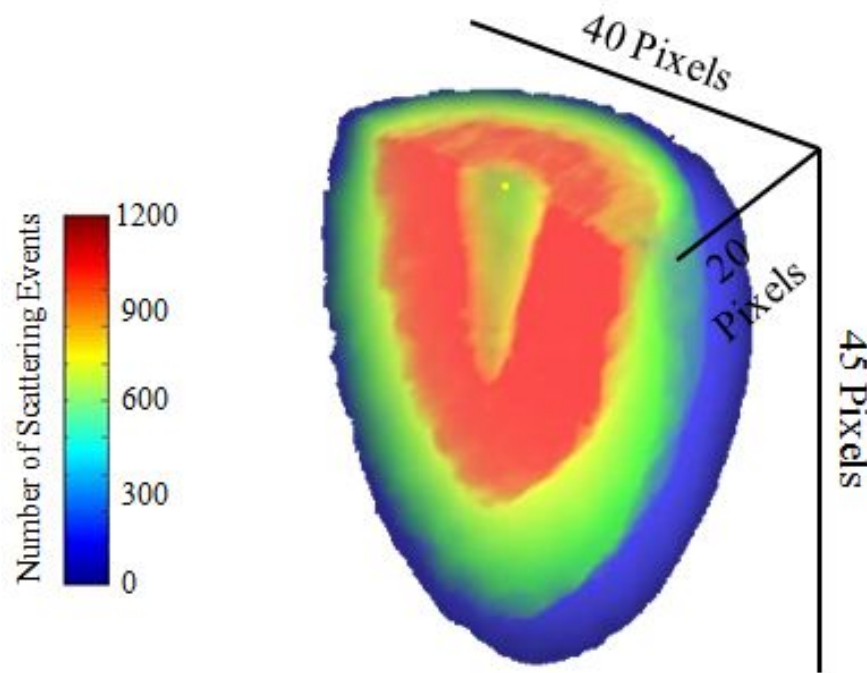


Fig. 7.10. A cross-sectional view of the 3D model of optical diffusion in biological tissue. The decreased intensity moving away from the point of incidence is evident in the figure.

tissue. The theoretical justification for using spheroids in a Monte Carlo algorithm is derived from the spheroidal shape of mitochondria and their significant effect on cellular scattering. Spheroidal parameters were chosen to be representative of the wavelength of near-infrared light and the comparable diameters of organelles. However, in order to determine the accuracy of spheroidal scattering-based diffusion, experimental results would need to be incorporated in future studies. The presented technique has been proposed to be a more physically accurate description of cellular scattering and, as such, would need to be compared with physical measurements. The presented results do, however, demonstrate the importance of the scattering method as its influence on the resulting diffusion is significant. This provides a basis for the theoretical accuracy of the presented Monte Carlo algorithm and supports the use of spheroids in diffusion models for optical tomography of tissue.

Additional results of this research, which are of interest for further study, include the differences exhibited by spherical and spheroidal-based diffusion profiles. Cell nuclei are

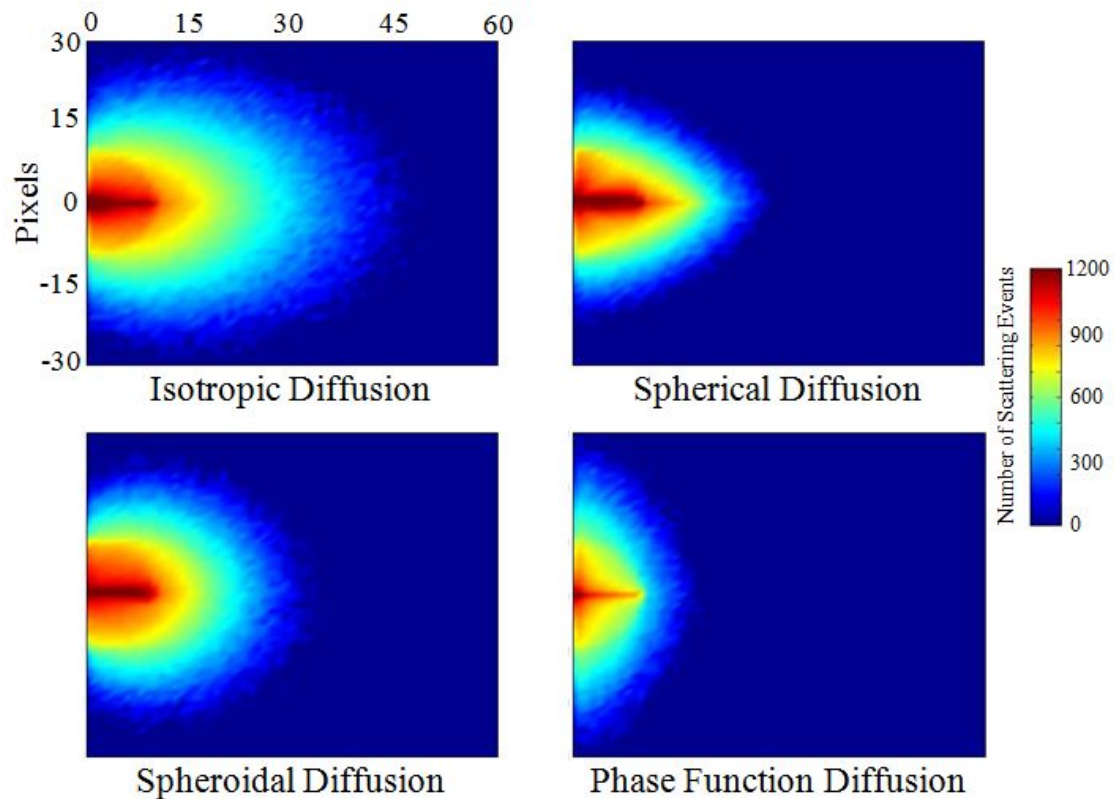


Fig. 7.11. A comparison of diffusion profiles formed using various scattering techniques. Each image was generated by a Monte Carlo algorithm, which used a different scattering method to determine subsequent photon directions. The upper left image incorporated isotropic scattering in which each direction was equally probable. The upper right image utilized the Mie scattering solution for spherical particles. The lower left image included the spheroidal scattering solution, and the lower right image used the Henyey-Greenstein phase function technique. The diffusion profiles exhibit noticeable differences indicating that the scattering mechanism included in a Monte Carlo algorithm has a significant effect on the resulting diffusion.

approximately spherical when healthy and begin to exhibit a deformed shape during the early stages of some cancers. This elongated structure may be more accurately described by spheroids than by spheres. Inhomogeneous collections of particles could be modeled with a hybrid Monte Carlo algorithm in which a given scattering site is chosen to either contain a sphere or a spheroid based on a probability weighted by concentration percentages. A hybrid algorithm optimized to be in sufficient agreement with physical measurements could be used as a diagnostic tool. A detected concentration of spheroidal particles above normal

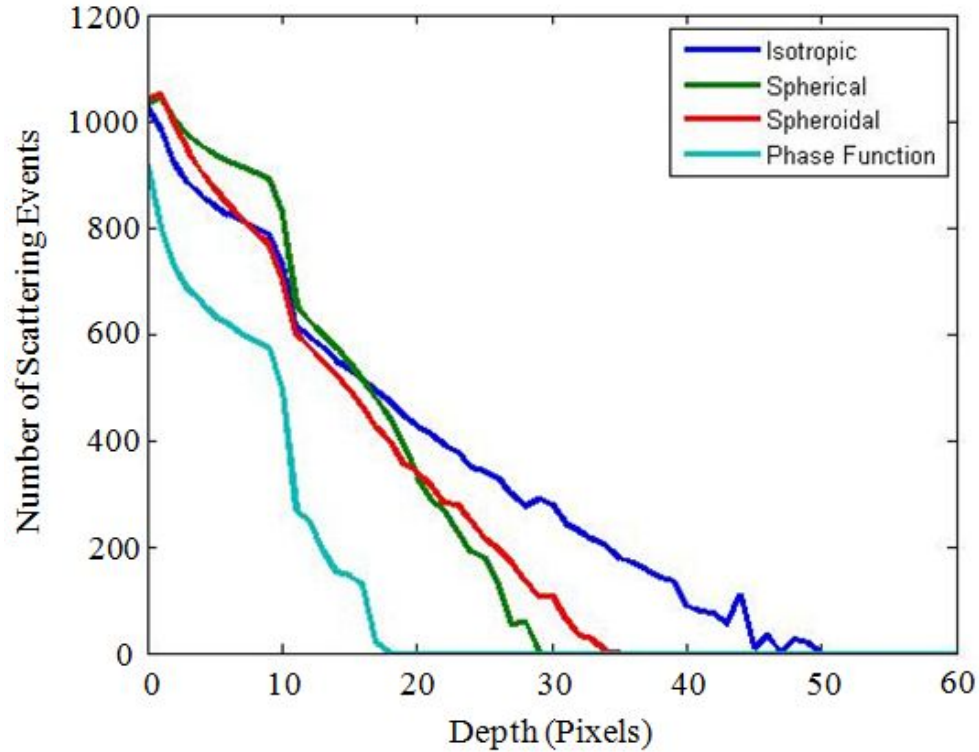


Fig. 7.12. Plots of depth intensities measured along the z axes of the diffusion profiles shown in Fig. 7.11. Plots of this type allow for a more quantitative description of the differences, which exist between diffusion profiles. The plots reaffirm that specific scattering mechanisms have a significant impact on the diffusion simulations created by Monte Carlo algorithms.

levels could potentially indicate the presence of malignant cells in otherwise healthy tissue. A hybrid Monte Carlo algorithm could also have applications in other fields, which are concerned with the existence and detection of certain types of particulate structures.

7.6. Conclusion

A spheroidal scattering solution based on the work of authors such as Flammer, Asano and, Yamamoto has been presented. The technique was used to develop a spheroidal scattering algorithm, which was capable of generating solutions to the spheroidal scattering problem for a specified angle of incidence. The algorithm was used to generate and store a series surface scattering images, which corresponded to various incident angles. The scat-

tering solution was then incorporated in a Monte Carlo algorithm for use in simulating sporadic photon migration in biological tissue. The method was supported by the spheroid-like shape of mitochondria and malignant cell nuclei. Diffusion profiles were generated using a variety of scattering methods including spheroidal scattering, spherical Mie scattering, the Henyey-Greenstein phase function, and isotropic randomized scattering. The resulting profiles were then compared in order to determine the influence a scattering technique had on a diffusive Monte Carlo algorithm. The simulated diffusion profiles exhibited noticeably different structures indicating that the incorporated scattering technique had a significant effect on the diffusion. These results suggest that an advanced Monte Carlo algorithm based on complex scattering solutions could be used as a diagnostic tool. Continued development of scattering algorithms could lead to improved tomographic capabilities. The presented results support the use of spheroids in future optical diffusion studies.

CHAPTER 8

CONCLUSION

The fundamental properties and imaging capabilities of sparse tomographic methods have been explored. This analysis has been performed for both straight-line and diffusive tomography in the context of atmospheric and biomedical imaging applications. An extensive investigation was conducted into the effect the initialization had on the convergence of the ART algorithms. It was determined through synthetic testing that the height of the initializing layer was its single most influential property. If the height of the initial guess coincided with the imaging object, other limiting factors, such as the one-sided ray configuration, could be overcome. It was demonstrated that accurate reconstructions could be created from data collected at only two viewing stations if the ART algorithms were initialized sufficiently. The accuracies of the PCART and MART algorithms were determined to be essentially equivalent and superior to other iterative reconstruction techniques including variations of ART. The highly ill-conditioned inverse problems arising from sparse data and limited imaging configurations were overcome using an initializing Gaussian profile centered at a specific height. This profile was used as the initial guess in the atmospheric applications. Mesospheric OH airglow emission layers were reconstructed using PCART and the validity of the images was verified through synthetic testing. A series of reconstructions was then used to create 3D models of the airglow layer. The presented reconstruction technique was also applied to satellite imagery of polar mesospheric clouds. Images of the PMC layer were reconstructed using this same technique and the projection data were interpolated to finer spatial resolutions using a cubic spline. A centroid technique was proposed as a means of identifying small-scale altitude variations in the layer using brightness asymmetries observed in the reconstructions. The sparse tomographic techniques developed for atmospheric applications were proposed to be applicable to the diffuse tomography methods of biomedical imaging. The one-sided imaging configuration and sparse data, which

result in near-infrared imaging modalities, are comparable to that of atmospheric tomography. The accuracy of diffusive tomographic methods is dependent upon the proficiency of the reconstruction algorithm and the photon migration model. A novel Monte Carlo algorithm was developed based on the solution of optical scattering by spheroidal particles. Mitochondria are approximately spheroidal in shape and account for a significant amount of the optical scattering, which occurs in cells. This method was suggested as a more physical approach to diffuse optical tomography due to its inclusion of intracellular structural information. Diffusion profiles were generated using Monte Carlo algorithms derived from spheroidal, spherical, isotropic, and phase function scattering. The results were compared and differences in the diffused intensities were evident. This result indicated the scattering mechanism used in a diffusive Monte Carlo algorithm affects the resulting intensity profile. This supports the use of spheroidal scattering models in diffusive optical tomography and suggests that advanced hybrid algorithms could be used as a diagnostic tool. The roughly spherical shape of cell nuclei can become deformed during the early stages of certain cancers and the ability to distinguish concentrations of spheroidal particles could allow for the detection of malignant cells in otherwise healthy biological tissue. The results of the tomographic reconstructions and diffusion simulations indicate the vast potential of sparse tomography methods and emphasizes the importance of continuing research into methods of this type.

REFERENCES

1. E. C. Beckmann, "CT scanning the early days," *Br. J. Radiol.* **79**, 5-8 (2006).
2. G. N. Hounsfield, "Computerized transverse axial scanning (tomography): Part 1. Description of system," *Br. J. Radiol.* **46**, 1016-1022 (1973).
3. R. Gordon, R. Bender, and G. T. Herman, "Algebraic reconstruction techniques (ART) for three-dimensional electron microscopy and x-ray photography," *J. Theor. Biol.* **29**, 471-476 (1970).
4. A. M. Cormack, "Representation of a function by its line integrals, with some radiological applications," *J. Appl. Phys.* **34**, 2722-2727 (1963).
5. K. M. Crowe, T. F. Budinger, J. L. Cahoon, V. P. Elischer, R. H. Huesman, and L. L. Kanstein, "Axial scanning with 900 MeV alpha particles," *IEEE Trans. Nucl. Sci.* **22**, 1752-1754 (1975).
6. J. M. Lewin, C. J. D'Orsi, R. E. Hendrick, L. J. Moss, P. K. Isaacs, A. Karellas, and G. R. Cutter, "Clinical comparison of full-field digital mammography and screen-film mammography for detection of breast cancer," *Am. J. Roentgenology* **179**, 671-677 (2002).
7. M. M. Ter-Pogossian, M. E. Phelps, E. J. Hoffman, and N. A. Mullani, "A positron-emission transaxial tomograph for nuclear imaging (PETT)," *Radiology* **114**, 89-98 (1975).
8. K. J. Friston, D. E. Glaser, R. N. A. Henson, S. Kiebel, C. Phillips, and J. Ashburner, "Classical and bayesian inference in neuroimaging: applications," *Neuroimage* **16**, 484-512 (2002).
9. J. Boutet, L. Herve, M. Debourdeau, L. Guyon, P. Peltie, J. Dinten, L. Saroul, F. Duboeuf, and D. Vray, "Bimodal ultrasound and fluorescence approach for prostate cancer diagnosis," *J. Biomed. Opt.* **14**, 64001 (2009).
10. J. F. Drake and J. Warner, "A theoretical study of the accuracy of tomographic retrieval of cloud liquid with an airborne radiometer," *J. Atmos. Ocean. Technol.* **5**, 844-857 (1987).
11. A. F. Fercher, "Optical coherence tomography," *J. Biomed. Opt.* **1**, 157-173 (1996).

12. J. M. Ollinger and J. A. Fessler, "Positron-emission tomography," *IEEE Sig. Proc. Mag.* **14**, 43-55 (1997).
13. G. F. Knoll, "Single-photon emission computed tomography," *Proceed. IEEE* **71**, 320-329 (1983).
14. T. O. McBride, B. W. Pogue, E. D. Gerety, S. B. Poplack, U. L. Osterberg, and K. D. Paulsen, "Spectroscopic diffuse optical tomography for the quantitative assessment of hemoglobin concentration and oxygen saturation in breast tissue," *App. Opt.* **38**, 5480-5490 (1999).
15. X. Duan, Y. Liang, D. S. Friedman, L. Sun, T. Wong, Q. Tao, L. Bao, N. Wang, and J. Wang, "Normal macular thickness measurements using optical coherence tomography in healthy eyes of adult chinese persons: the Handan eye study," *Ophthalmology* **117**, 1585-1594 (2010).
16. T. R. Elliot, and R. J. Heck, "A comparison of optical and x-ray CT technique for void analysis in soil thin section," *Geoderma* **141**, 60-70 (2007).
17. J. B. LeBret, M. G. Norton, and D. F. Bahr, "Examination of crystal defects with high-kv x-ray computed tomography," *Materials Lett.* **59**, 1113-1116 (2005).
18. A. C. Kak, and M. Slaney, "Principles of computerized tomographic imaging," *Soc. for Industrial and Applied Mathematics*, 49-68, 275-292 (2001).
19. J. Radon and P. C. Parks, "On the determination of functions from their integral values along certain manifolds," *IEEE Trans. Med. Imag.* **5**, 170-176 (1986).
20. T. S. Durrani and D. Bisset, "The Radon transform and its properties," *Geophys.* **49**, 1180-1187 (1984).
21. E. A. Robinson, "Spectral approach to geophysical inversion by Lorentz, Fourier, and Radon transforms," *Proc. IEEE* **70**, 1039-1054 (1982).
22. L. Zhang, F. Gao, H. He, and H. Zhao, "Three-dimensional scheme for time-domain fluorescence molecular tomography based on Laplace transforms with noise-robust factors," *Opt. Exp.* **16**, 7214-7223 (2008).
23. S. Kaczmarz, "Angenäherte auflösung von systemen linearer gleichungen," *Bulletin International De L' Académie Polonaise des Sciences et Lettres* **3**, Class A 355-357 (1937).

24. N. T. Gaarder and G. T. Herman, "Algorithms for reproducing objects from their x-rays," *Comp. Graph. Imag. Process.* **1**, 97-106 (1972).
25. G. T. Herman, A. Lent, and S. W. Rowland, "ART: mathematics and applications: a report on the mathematical foundations and on the applicability to real data of the algebraic reconstruction techniques," *J. Theor. Biol.* **42**, 1-18 (1973).
26. J. M. M. Anderson, B. A. Mair, M. Rao, and C. H. Wu, "Weighted least-squares reconstruction methods for positron emission tomography," *IEEE Trans. Med. Imag.* **16**, 159-165 (1997).
27. V. Y. Khomich, A. I. Semenov, and N. N. Shefov, "Introduction," in *Airglow as an Indicator of Upper Atmospheric Structure and Dynamics* (Springer, 2008), pp. 1-5.
28. S. Chakrabarti, "Ground based spectroscopic studies of sunlit airglow and aurora," *J. Atmos. and Sol. Terr. Phys.* **60**, 1403-1423 (1998).
29. D. M. Hunten, "Spectroscopic studies of the twilight airglow," *Space Sci. Rev.* **6**, 493-573 (1967).
30. W. E. Sharp, J. W. F. Lloyd, and S. M. Silverman, "Zenith skylight intensity and color during the total solar eclipse of 20 July 1963," *Appl. Opt.* **5**, 787-792 (1966).
31. X. Y. Zhou, D. Lummerzheim, R. Gladstone, and S. Gunapala, "Feasibility of observing dayside aurora using NIR camera onboard high-altitude balloons," *Geophys. Res. Lett.* **34**, L03105 (2007).
32. K. Kita, N. Iwagami, and T. Ogawa, "Rocket observations of oxygen night airglows: Excitation mechanisms and oxygen atom concentration," *Planet. Space Sci.* **40**, 1269-1288 (1992).
33. G. Schmidtke, P. Seidl, and C. Wita, "Airglow-solar spectrometer instrument (20700 nm) aboard the San Marco D/L satellite," *Appl. Opt.* **24**, 3206-3213 (1985).
34. I. C. McDade and E. J. Llewellyn, "Inversion techniques for recovering two-dimensional distributions of auroral emission rates from tomographic rocket photometer measurements," *Can. J. Phys.* **69**, 1059-1068 (1991).
35. I. C. McDade, N. D. Lloyd, and E. J. Llewellyn, "A rocket tomography measurement of the N_2^+ 3914 Å emission rates within an auroral arc," *Planet. Space Sci.* **39**, 895-906 (1991).

36. I. C. McDade and E. J. Llewellyn, "Satellite airglow limb tomography: Methods for recovering structured emission rates in the mesospheric airglow layer," *Can. J. Phys.* **71**, 552-563 (1993).
37. E. J. Llewellyn, W. S. C. Brooks, I. C. McDade, and D. W. Johnson, "Tomography from a Canadian small satellite in low earth orbit," *Can. Aeronaut. Space J.* **37**, 72-76 (1994).
38. D. A. Degenstein, R. L. Gattinger, N. D. Lloyd, A. E. Bourassa, J. T. Wiensz, and E. J. Llewellyn, "Observations of an extended mesospheric tertiary ozone peak," *J. Atmos. and Sol. Terr. Phys.* **67**, 1395-1402 (2005).
39. D. A. Degenstein, A. E. Bourassa, C. Z. Roth, and E. J. Llewellyn, "Limb scatter ozone retrieval from 10 to 60 km using a multiplicative algebraic reconstruction technique," *Atmos. Chem. Phys.* **9**, 6521-6529 (2009).
40. P. E. Sheese, E. J. Llewellyn, R. L. Gattinger, A. E. Bourassa, D. A. Degenstein, N. D. Lloyd, and I. C. McDade, "Mesopause temperatures during the polar mesospheric cloud season," *Geophys. Res. Lett.* **38**, L11803 (2011).
41. L. L. Cogger and C. D. Anger, "The OI 5577 Å airglow experiment on the ISIS 2 satellite," *J. Atmos. and Terr. Phys.* **35**, 2081-2084 (1973).
42. A. L. Broadfoot, D. B. Hatfield, E. R. Anderson, T. C. Stone, B. R. Sandel, J. A. Gardner, E. Murad, D. J. Knecht, C. P. Pike, and R. A. Viereck, "N₂ triplet band systems and atomic oxygen in the dayglow," *J. Geophys. Res.* **102**, 11567-11584 (1997).
43. C. D. Anger, J. S. Murphree, A. V. Jones, R. A. King, A. L. Broadfoot, L. L. Cogger, F. Creutzberg, R. L. Gattinger, G. Gustafsson, F. R. Harris, J. W. Haslett, E. J. Llewellyn, D. J. McConnell, D. J. McEwen, E. H. Richardson, G. Rostoker, B. R. Sandel, G. G. Shepherd, D. Venkatesan, D. D. Wallis, G. Witt, "Scientific results from the Viking ultraviolet imager: an introduction," *Geophys. Res. Lett.* **14**, 383-386 (1987).
44. D. A. Degenstein, E. J. Llewellyn, and N. D. Lloyd, "Tomographic retrieval of the oxygen infrared atmospheric band with the OSIRIS infrared imager," *Can. J. Phys.* **82**, 501-515 (2004).
45. Z. Wang and S. Chen, "Effective solution algorithm for tomographic inversion of volume emission rate from satellite-based limb measurement," *Chin. Geogra. Sci.* **21**, 554-562 (2011).

46. P. E. Sheese, E. J. Llewellyn, R. L. Gattinger, A. E. Bourassa, D. A. Degenstein, N. D. Lloyd, and I. C. McDade, "Temperatures in the upper mesosphere and lower thermosphere from OSIRIS observations of O_2 A-band emission spectra," *Can. J. Phys.* **88**, 919-925 (2010).
47. M. J. Taylor, "A review of advances in imaging techniques for measuring short period gravity waves in the mesosphere and lower thermosphere," *Adv. Space Res.* **19**, 667-676 (1997).
48. T. Nygrén, M. Markkanen, M. Lehtinen, and K. Kaila, "Application of stochastic inversion in auroral tomography," *Ann. Geophys.* **14**, 1124-1133 (1996).
49. T. Nygrén, M. J. Taylor, M. S. Lehtinen, and M. Markkanen, "Application of tomographic inversion in studying airglow in the mesopause region," *Ann. Geophys.* **16**, 1180-1189 (1998).
50. T. Nygrén, M. J. Taylor, G. R. Swenson, and M. S. Lehtinen, "Observing gravity wave activity in the mesopause region by means of airglow tomography," *Adv. Space Res.* **26**, 903-906 (2000).
51. D. S. Anderson, G. Swenson, F. Kamalabadi, and A. Liu, "Tomographic imaging of airglow from airborne spectroscopic measurements," *Appl. Opt.* **47**, 2510-2519 (2008).
52. J. Semeter and M. Mendillo, "A nonlinear optimization technique for ground-based atmospheric emission tomography," *IEEE Trans. Geosci. and Rem. Sens.* **35**, 1105-1116 (1997).
53. D. J. Baker and A. T. Stair, "Rocket measurements of the altitude distributions of the hydroxyl airglow," *Phys. Scr.* **37**, 611 (1988).
54. M. J. Taylor, D. C. Fritts, and J. R. Isler, "Determination of horizontal and vertical structure of an unusual pattern of short-period gravity waves imaged during ALOHA-93," *Geophys. Res. Lett.* **22**, 2837-2840 (1995).
55. R. A. Bernstein, W. L. Freedman, and B. F. Madore, "The first detections of the extragalactic background light at 3000, 5500, and 8000 Å. I. results," *Astrophys. J.* **571**, 56-84 (2002).
56. E. E. Remsberg, B. T. Marshall, M. Garcia-Comas, D. Krueger, G. S. Lingenfelter, J. Martin-Torres, M. G. Mlynczak, J. M. Russell III, A. K. Smith, Y. Zhao, C. Brown, L. L. Gordley, M. J. Lopez-Gonzalez, M. Lopez-Puertas, C. -Y. She, M. J. Taylor, and R. E. Thompson, "Assesment of the quality of the Version 1.07 temperature-versus-

- pressure profiles of the middle atmosphere from TIMED/SABER,” *J. Geophys. Res.* **113**, D17101 (2008).
57. B. Gustavsson, T. Sergienko, M. T. Rietveld, F. Honary, Å. Steen, B. U. E. Brändström, T. B. Leyser, A. L. Aruliah, T. Aso, M. Ejiri, and S. Marple, “First tomographic estimate of volume distribution of HF-pump enhanced airglow emission,” *J. Geophys. Res.* **106**, 29,105-29,123 (2001).
 58. Y. M. Zhao, M. J. Taylor, and X. Chu, “Comparison of simultaneous Na lidar and mesospheric nightglow temperature measurements and the effects of tides on the emission layer heights,” *J. Geophys. Res.* **110**, D09S07 (2005).
 59. M. J. Taylor, M. B. Bishop, and V. Taylor, “All-sky measurements of short period waves imaged in the OI (557.7 nm), Na (589.2 nm) and near infrared OH and O₂ (0,1) nightglow emissions during the ALOHA-93 campaign,” *Geophys. Res. Lett.* **22**, 2833 (1995).
 60. F. J. Garcia, M. J. Taylor, and M. C. Kelley, “Two-dimensional spectral analysis of mesospheric airglow image data,” *Appl. Opt.* **36**, 7374 (1997).
 61. D. Pautet and G. Moreels, “Ground-based satellite-type images of the upper-atmosphere emissive layer,” *Appl. Opt.* **41**, 823 (2002).
 62. D. S. Anderson, F. Kamalabadi, and G. R. Swenson, “Estimation of three-dimensional atmospheric wave parameters From ground-based spectroscopic airglow image data,” *IEEE Trans. Geosci. and Remote Sens.* **47**, 2427-2435 (2009).
 63. J. Fujii, T. Nakamura, T. Tsuda, and K. Shiokawa, “Comparisons of winds measured by MU radar and Fabry-Perot interferometer and effect of OI5577 airglow height variations,” *J. Atmos. Sol. Terr. Phys.* **66**, 573-583 (2004).
 64. S. Adler-Golden, “Kinetic parameters for OH nightglow modeling consistent with recent laboratory measurements,” *J. Geophys. Res.* **102**, 19,969-19,976 (1997).
 65. T. W. Backhouse, “The luminous cirrus cloud of June and July,” *Meteorol. Mag.* **20**, 133 (1885).
 66. R. Leslie, “Sky glows,” *Nature* **32**, 245 (1885).
 67. G. E. Thomas, “Mesospheric clouds and the physics of the mesopause region,” *Rev. Geophys.* **29**, 553-575 (1991).

68. G. E. Thomas, "Is the polar mesosphere the miner's canary of global change?" *Adv. Space Res.* **18**, 149-158 (1996).
69. M. Hervig, R. E. Thompson, M. McHugh, L. L. Gordley, J. M. Russell III, and M. E. Summers, "First confirmation that water ice is the primary component of polar mesospheric clouds," *Geophys. Res. Lett.* **28**, 971-974 (2001).
70. E. P. Shettle, M. T. DeLand, G. E. Thomas, and J. J. Olivero, "Long-term variations in the frequency of polar mesospheric clouds in the northern hemisphere from SBUV," *Geophys. Res. Lett.* **36**, L02803 (2009).
71. W. Foerster, *Von der Erdatmosphäre zum Himmelsraum* (Berlin ; Leipzig : H. Hillger, 1906).
72. S. M. Bailey, A. W. Merkel, G. E. Thomas, and J. N. Carstens, "Observations of polar mesospheric clouds by the student nitric oxide explorer," *J. Geophys. Res.* **110**, D13203 (2005).
73. O. Jesse, "Die Höhe der leuchtenden Nachtwolken," *Astron. Nachrichten* **140**, 161-168 (1896).
74. X. Chu, C. S. Gardner, and G. Papen, "Lidar observations of polar mesospheric clouds at south pole: diurnal variations," *Geophys. Res. Lett.* **28**, 1937-1940 (2001).
75. M. J. Taylor, A. P. van Eyken, H. Rishbeth, G. Witt, N. Witt, and M. A. Clilverd, "Simultaneous observations of noctilucent clouds and polar mesospheric radar echoes: evidence of non-correlation," *Planet. Space. Sci.* **37**, 1013-1020 (1989).
76. M. J. Taylor, M. Gadsden, R. P. Lowe, M. S. Zalcik, and J. Brausch, "Mesospheric cloud observations at unusually low latitudes," *J. Atmos. Sol. Terr. Phys.* **64**, 991-999 (2002).
77. J. Y. N. Cho and M. C. Kelley, "Polar mesosphere summer radar echoes: observations and current theories," *Rev. Geophys.* **31**, 243-265 (1993).
78. M. Rapp, F. J. Lübken, A. Müllemann, G. E. Thomas, and E. J. Jensen, "Small-scale temperature variations in the vicinity of NLC: experimental and model results," *J. Geophys. Res.* **107** 4392 (2002).
79. T. M. Donahue, B. Guenther, and J. E. Blamont, "Noctilucent clouds in daytime: circumpolar particulate layers near the summer mesopause," *J. Atmos. Sci.* **29**, 1205-1209 (1972).

80. E. J. Jensen, G. E. Thomas, and O. B. Toon, "On the diurnal variation of noctilucent clouds," *J. Geophys. Res.* **94**, 14693-14702 (1989).
81. O. B. Vasil'yev, C. I. Willmann, N. M. Gavrilov, V. V. Kovalenok, A. I. Lazarev, and N. P. Fast, "Studies of noctilucent clouds from space," *Gidrometeoizdat, Leningrad* (1987).
82. D. M. Packer and I. G. Packer, "Exploring the earth's atmosphere by photography from Skylab," *App. Opt.* **16**, 983-992 (1977).
83. R. J. Thomas, C. A. Barth, D. W. Rusch, and R. W. Sanders, "Solar mesosphere explorer near-infrared spectrometer measurements of $1.27\text{-}\mu\text{m}$ radiances and the inference of mesospheric ozone," *J. Geophys. Res.* **89**, 9569-9580 (1984).
84. C. A. Reber, "The upper atmosphere research satellite (UARS)," *Geophys. Res. Lett.* **20**, 1215-1218 (1993).
85. D. E. Siskind, L. Coy, and P. Espy, "Observations of stratospheric warmings and mesospheric coolings by the TIMED SABER instrument," *Geophys. Res. Lett.* **32**, L09804, (2005).
86. SSC Group, "Odin," <http://www.sscspace.com/odin-1>.
87. R. L. Gattinger, W. F. J. Evans, I. C. McDade, D. A. Degenstein, and E. J. Llewellyn, "Observation of the chemiluminescent $\text{NO}+\text{O}\rightarrow\text{NO}_2+\text{h}\nu$ reaction in the upper mesospheric dark polar regions by OSIRIS on Odin," *Can. J. Phys.* **87**, 925-932 (2009).
88. D. A. Degenstein, E. J. Llewellyn, and N. D. Lloyd, "Volume emission rate tomography from a satellite platform," *App. Opt.* **42**, 1441-1450 (2003).
89. J. M. Russell III, "AIM satellite helps to illuminate why Noctilucent Clouds form and vary," <http://aim.hamptonu.edu/>.
90. J. Y. N. Cho and J. Röttger, "An updated review of polar mesosphere summer echoes: observation, theory, and their relationship to noctilucent clouds and subvisible aerosols," *J. Geophys. Res.* **102**, 2001-2020 (1997).
91. B. Karlsson and J. Gumbel, "Challenges in the limb retrieval of noctilucent cloud properties from Odin/OSIRIS," *Adv. Space Res.* **36**, 935-942 (2005).
92. J. M. Russell III, "Instrument overview," <http://aim.hamptonu.edu/instrmt/cips.html>.

93. D. W. Rusch, G. E. Thomas, W. McClintock, A. W. Merkel, S. M. Bailey, J. M. Russell III, C. E. Randall, C. Jeppesen, and M. Callan, "The cloud imaging and particle size experiment on the aeronomy of ice in the mesosphere mission: cloud morphology for the northern 2007 season," *J. Atmos. Sol. Terr. Phys.* **71**, 356-364 (2009).
94. W. E. McClintock, D. W. Rusch, G. E. Thomas, A. W. Merkel, M. R. Lankton, V. A. Drake, S. M. Bailey, and J. M. Russell III, "The cloud imaging and particle size experiment on the aeronomy of ice in the mesosphere mission: instrument concept, design, calibration, and on-orbit performance," *J. Atmos. Sol. Terr. Phys.* **71**, 340-355 (2009).
95. J. Klostermeyer, "Effect of tidal variability on the mean diurnal variation of noctilucent clouds," *J. Geophys. Res.* **106**, 9749-9755 (2001).
96. W. C. Röntgen, "Ueber eine neue Art von Strahlen," *Ann. der Phys.* **300**, 1-11 (1898).
97. M. Cutler, "Transillumination of the breast," *Surg. Gynecol. Obstet.* **48**, 721-727 (1929).
98. E. Carlsen, "Transillumination light scanning," *Diagn. Imag.* **4**, 28-34 (1982).
99. C. M. Gros, Y. Quenneville, and Y. J. Hummel, "Diaphanologie mammaire," *Radiol. Electrol. Med. Nucl.* **53**, 297-306 (1972).
100. D. A. Boas, D. H. Brooks, E. L. Miller, C. A. Dimarzio, M. Kilmer, R. J. Gaudette, and Q. Zhang, "Imaging the body with diffuse optical tomography," *IEEE Sig. Proc. Mag.* 57-75 (Nov 2001).
101. J. Wang, S. Jiang, Z. Li, R. M. diFlorio-Alexander, R. J. Barth, P. A. Kaufman, B. W. Pogue, and K. D. Paulsen, "In vivo quantitative imaging of normal and cancerous breast tissue using broadband diffuse optical tomography," *Med. Phys.* **37**, 3715-3724 (2010).
102. H. J. Böhringer, E. Lankenau, F. Stellmacher, E. Reusche, G. Hüttmann, and A. Giese, "Imaging of human brain tumor tissue by near-infrared laser coherence tomography," *Acta Neurochirurgica* **151**, 507-517 (2009).
103. A. Custo, D. A. Boas, D. Tsuzuki, I. Dan, R. Mesquita, B. Fischl, W. E. L. Grimson, and W. Wells, "Anatomical atlas-guided diffuse optical tomography of brain activation," *NeuroImage* **49**, 561-567 (2010).
104. M. Friebe, J. Helfmann, U. Netz, and M. Meinke, "Influence of oxygen saturation

- on the optical scattering properties of human red blood cells in the spectral range 250 to 2000 nm,” J. Biomed. Opt. **14**, 034001 (2009).
105. F. E. Robles, S. Chowdhury, and A. Wax, “Assesing hemoglobin concentration using spectroscopic optical coherence tomography for feasibility of tissue diagnostics,” Biomed. Opt. Expr. **1**, 310-317 (2010).
 106. L. Zamboni, D. R. Mishell Jr., J. H. Bell, and M. Baca, “Fine structure of the human ovum in the pronuclear stage,” J. Cell Biol. **30**, 579-600 (1966).
 107. B. Beauvoit, S. M. Evans, T. W. Jenkins, E. E. Miller, and B. Chance, “Correlation between the light scattering and the mitochondrial content of normal tissues and transplantable rodent tumors,” Anal. Biochem. **226**, 167-174 (1995).
 108. A. Dunn and R. Richards-Kortum, “Three-dimensional computation of light scattering from cells,” IEEE J. Sel. Top. Quantum Electron. **2**, 898-905 (1996).
 109. C. E. Wenner, E. J. Harris, and B. C. Pressman, “Relationship of the light scattering properties of mitochondria to the metabolic state in intact ascites cells,” J. Biol. Chem. **242**, 3454-3459 (1967).
 110. T. H. Ji and D. W. Urry, “Correlation of light scattering and absorption flattening effects with distortions in the circular dichroism patterns of mitochondrial membrane fragments,” Biochem. Biophys. Res. Commun. **4**, 404-411 (1969).
 111. J. R. Mourant, M. Canpolat, C. Brocker, O. Esponda-Ramos, T. M. Johnson, A. Matanock, K. Stetter, and J. P. Freyer, “Light scattering from cells: the contribution of the nucleus and the effects of proliferative status,” J. Biomed. Opt. **5**, 131 (2000).
 112. A. Claude and E. F. Fullam, “An electron microscope study of isolated mitochondria: method and preliminary results,” J. Exp. Med. **81**, 51-62 (1945).
 113. K. Yamauchi, M. Yang, P. Jiang, N. Yamamoto, M. Xu, Y. Amoh, K. Tsuji, M. Bouvet, H. Tsuchiya, K. Tomita, A. R. Moossa, and R. M. Hoffman, “Real-time in vivo dual-color imaging of intracapillary cancer cell and nucleus deformation and migration,” Cancer Res. **65**, 4252 (2005).
 114. L. V. Wang and H. Wu, *Biomedical Optics: Principles and Imaging* (John Wiley & Sons Inc., 2007), pp. 37-60.
 115. N. V. Voshchinnikov, “Electromagnetic scattering by homogenous and coated

- spheroids: calculations using the separation of variables method,” J. Quant. Spectr. Rad. Trans. **55**, 627-636 (1996).
116. T. Rother, “Generalization of the separation of variables method for non-spherical scattering on dielectric objects,” J. Quant. Spectr. Rad. Trans. **60**, 335-353 (1998).
117. S. Asano and G. Yamamoto, “Light scattering by a spheroidal particle,” App. Opt. **14**, 29-49 (1975).
118. J. A. Stratton, *Electromagnetic Theory* (McGraw-Hill Book Company, 1941).
119. C. Flammer, *Spheroidal Wave Functions* (Stanford University Press, 1957).
120. P. Kirby, “Calculation of spheroidal wave functions,” Comp. Phys. Comm. **175**, 465-472 (2006).
121. L. G. Henyey and J. L. Greenstein, “Diffuse radiation in the galaxy,” Astrophys. J. **93**, 70-83 (1941).
122. Y. Xu, “Electromagnetic scattering by an aggregate of spheres,” App. Opt. **34**, 4573-4588 (1995).

APPENDICES

APPENDIX A

A LAYERED INITIALIZATION TECHNIQUE

Throughout the course of the presented tomographic research, an extensive amount of synthetic testing was performed in order to better understand the behavior of the ART algorithms given certain types of data. During this process, the effect the initialization had on the convergence of the algorithm was thoroughly studied. The influence of the initial guess was analyzed through simulation and a wide range of initializations were used in order to distinguish patterns and trends in the resulting images. As discussed previously, it was observed that when the vertical location of the initial guess corresponded to that of the imaging object, the resulting reconstructions were significantly more accurate. When flat initial profiles were used, which were broader than the imaging object, the reconstructed image did not localize well and the resulting structure was smeared or distorted. The ability to determine the altitude and width of an imaging object is therefore critical to successfully reconstructing sparse data. This is particularly true when the imaging object is a layered structure of some type, such as a cloud or emission layer in atmospheric science. Stratified regions of soil or rock have similar properties in geophysical applications. Often times there are additional measurements, which can be performed by supplemental instrumentation (lidar, ultrasound, etc.), in order to determine the location and dimensions of an imaging object. However, because the accuracy of the reconstructions relies so heavily on the position of the initial guess, various tests were conducted in order to assess whether the height and width of an object could be acquired solely from the measured projection data.

At times, the effects of certain initial guesses were difficult to quantify and some of the observed patterns did not remain consistent. However, one characteristic of the initialization seemed to generally hold true throughout the synthetic testing. The regions of the grid in which the initial guess overlapped the imaging object appeared brighter in the reconstructed image than those in which they did not overlap. This effect is seen in Fig. A.1. A

technique was developed based on this behavior in which a series of layered initial profiles were used to reconstruct the synthetic data. A single layer, one pixel wide, at a given altitude was used to initialize the algorithm. The reconstructed magnitude of each pixel in the layer was averaged in order to produce a quantitative reconstructed brightness value. The altitude of the initializing layer was then adjusted and the process was repeated. The layers were scanned across the entire imaging region and the resulting value of the pixel intensities were plotted against the corresponding altitudes. The resulting profile indicated the location of the imaging object as shown in Fig. A.2. Higher values in the plotted profiles coincided with higher pixel values in the imaging object.

Additional testing was performed to determine whether the algorithm could distinguish height variation moving across the layer horizontally. An enveloping effect was observed in which the outline of the object was discernable, but local altitude variations were not detected. Attempts were made to divide the imaging region into sections, but their success was inconsistent because of the sparse ray geometry. The technique does, however, demonstrate that certain properties of the imaging region can be obtained from the projection data by comparing the results of a series of initializations. Further research into this topic may yield additional insight into the amount of information that can be acquired from projections without a priori knowledge of the imaging object.

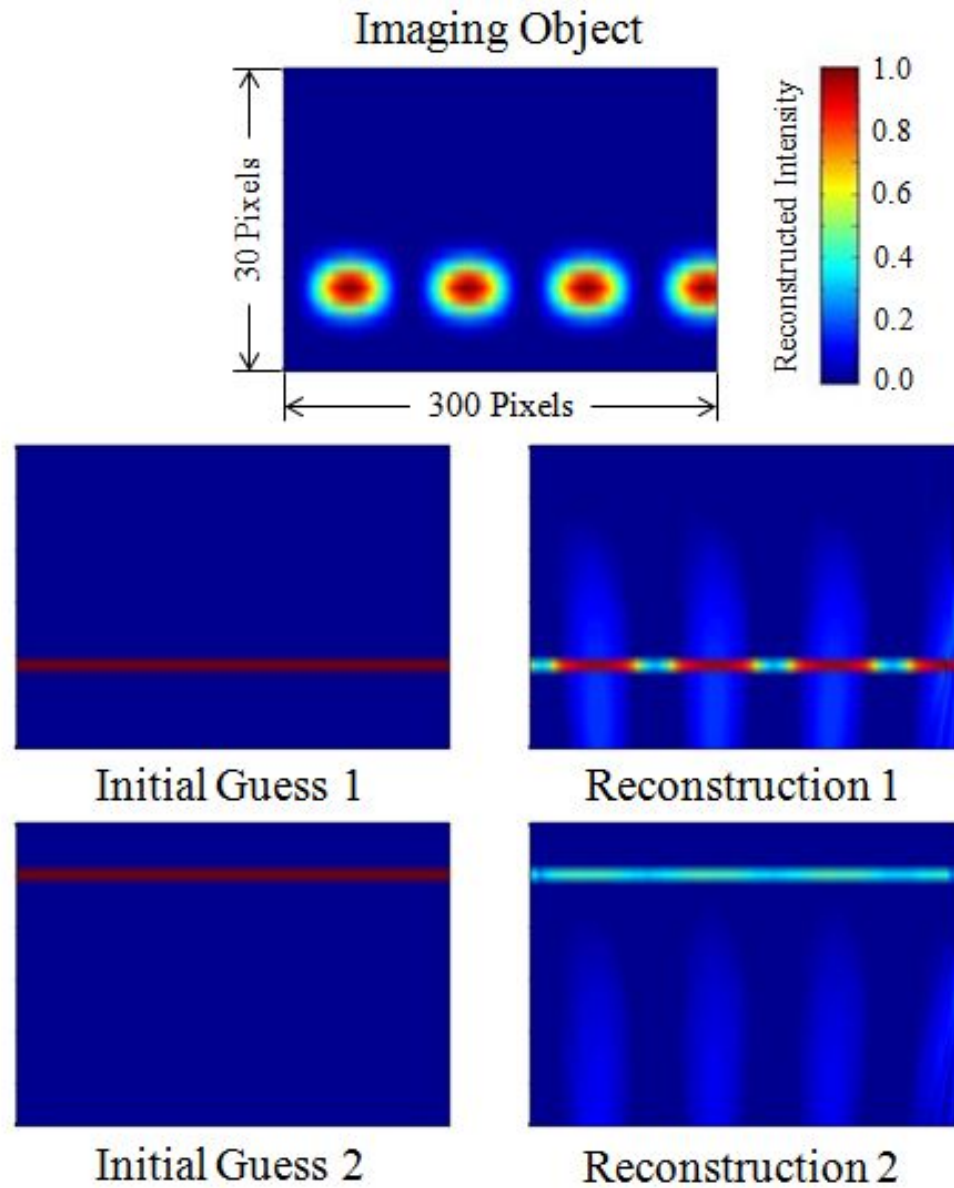


Fig. A.1. Reconstructed intensities using a single-layer initial profile. Synthetic testing was performed using a thin initial guess set at a certain height. It was determined during the testing that reconstructed images appeared brighter when the altitude of the initial guess coincided with the imaging object. This is demonstrated in the figure as Reconstruction1 appears brighter than Reconstruction2.

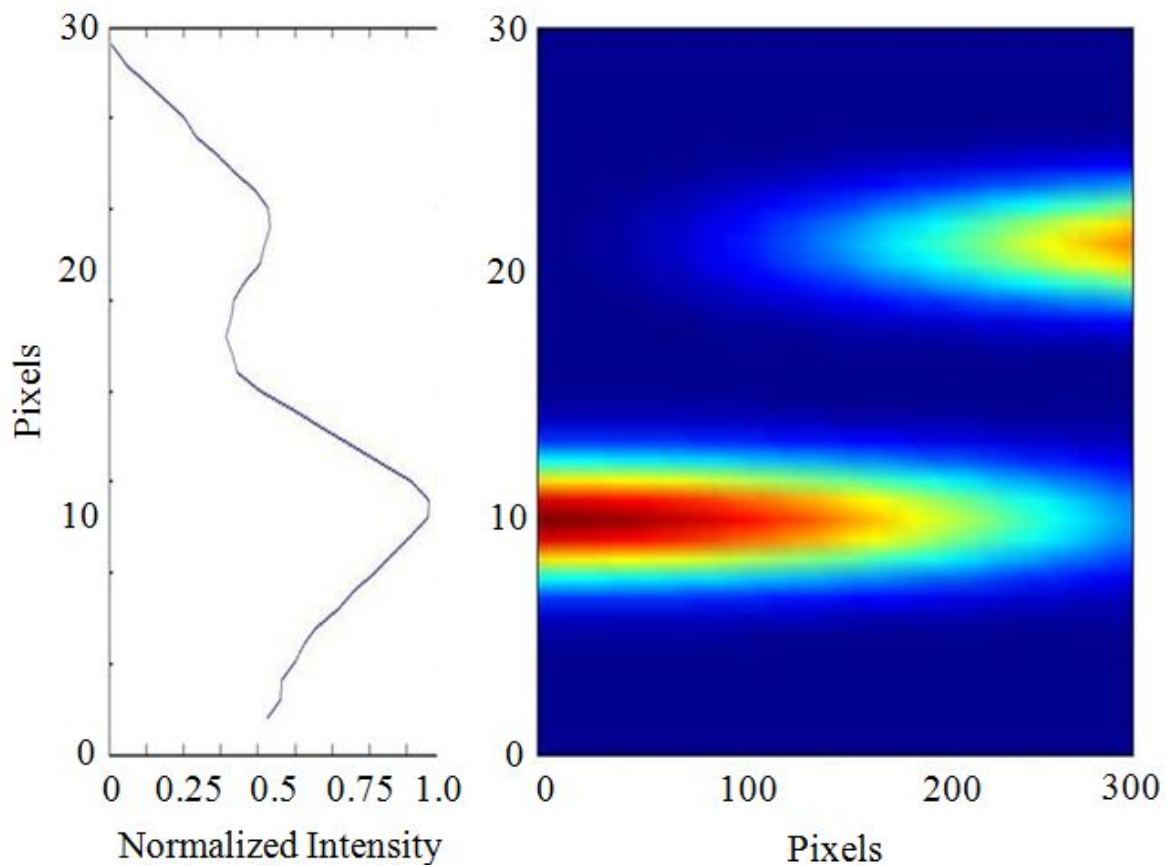


Fig. A.2. A plot of the normalized layer intensities against altitude. Single-layer profiles were used to reconstruct an imaging object as shown in Fig. A.1. The brightness of each pixel in the reconstructed layer was summed and normalized to create a brightness value, which was then associated with the given height. The altitude of the initial guess was adjusted and the process was repeated. A plot of these brightness values at each altitude is shown on the left. The plot reproduces the structure of the actual imaging object shown on the right.

APPENDIX B

ADDITIONAL SCATTERING IMAGES

Presented here are additional images of the scattered intensities from light incident on a prolate spheroidal particle. The incident angle of the light is measured from the z axis and is indicated by ζ in each figure. The images show the scattered intensities on the surface of the spheroid and were used in the spheroidal Monte Carlo algorithm to determine subsequent photon directions. The orientation of the axes is consistent in each image and is demonstrated in Fig. B.1. Additional scattering profiles for a range of incident angles are shown in Figs. B.2, B.3, B.4, and B.5.

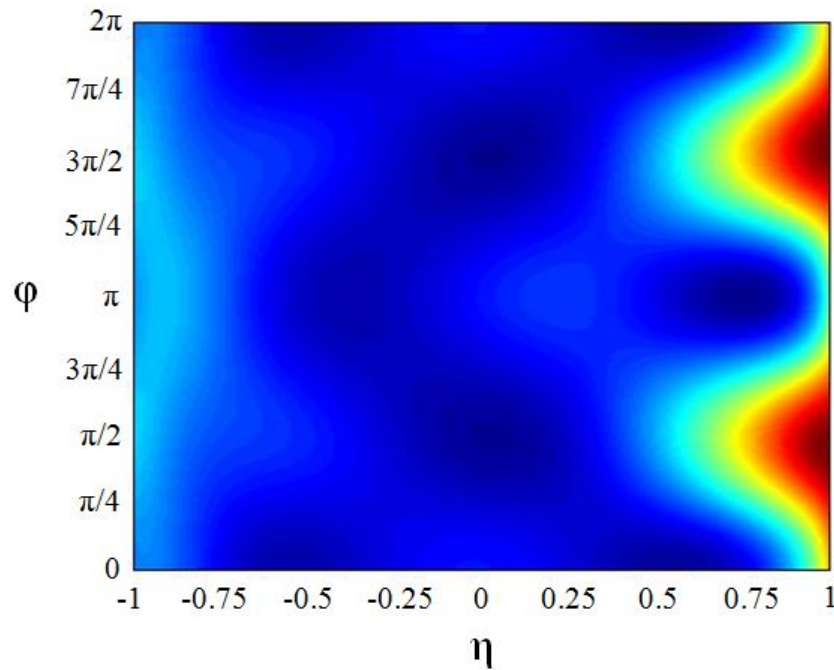


Fig. B.1. An explanation of the axes omitted in the subsequent scattering diagrams. The images show the scattered intensity on the surface of spheroids for varying incident angles. The x axis represents the inclination angle and the y axis represents the azimuthal angle.

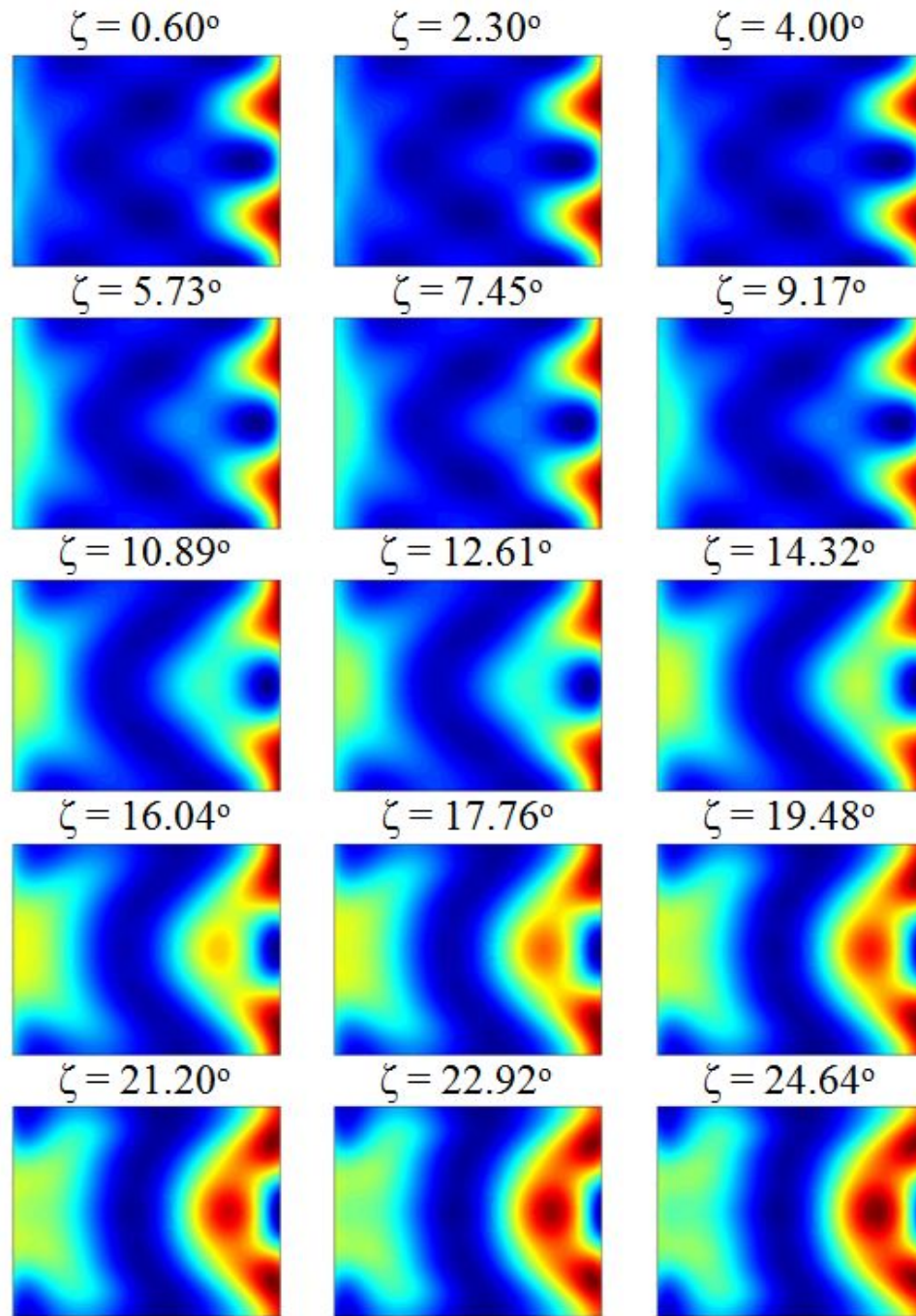


Fig. B.2. Additional scattering images shown for incident angles $\zeta=0.60^\circ$ through $\zeta=24.64^\circ$.

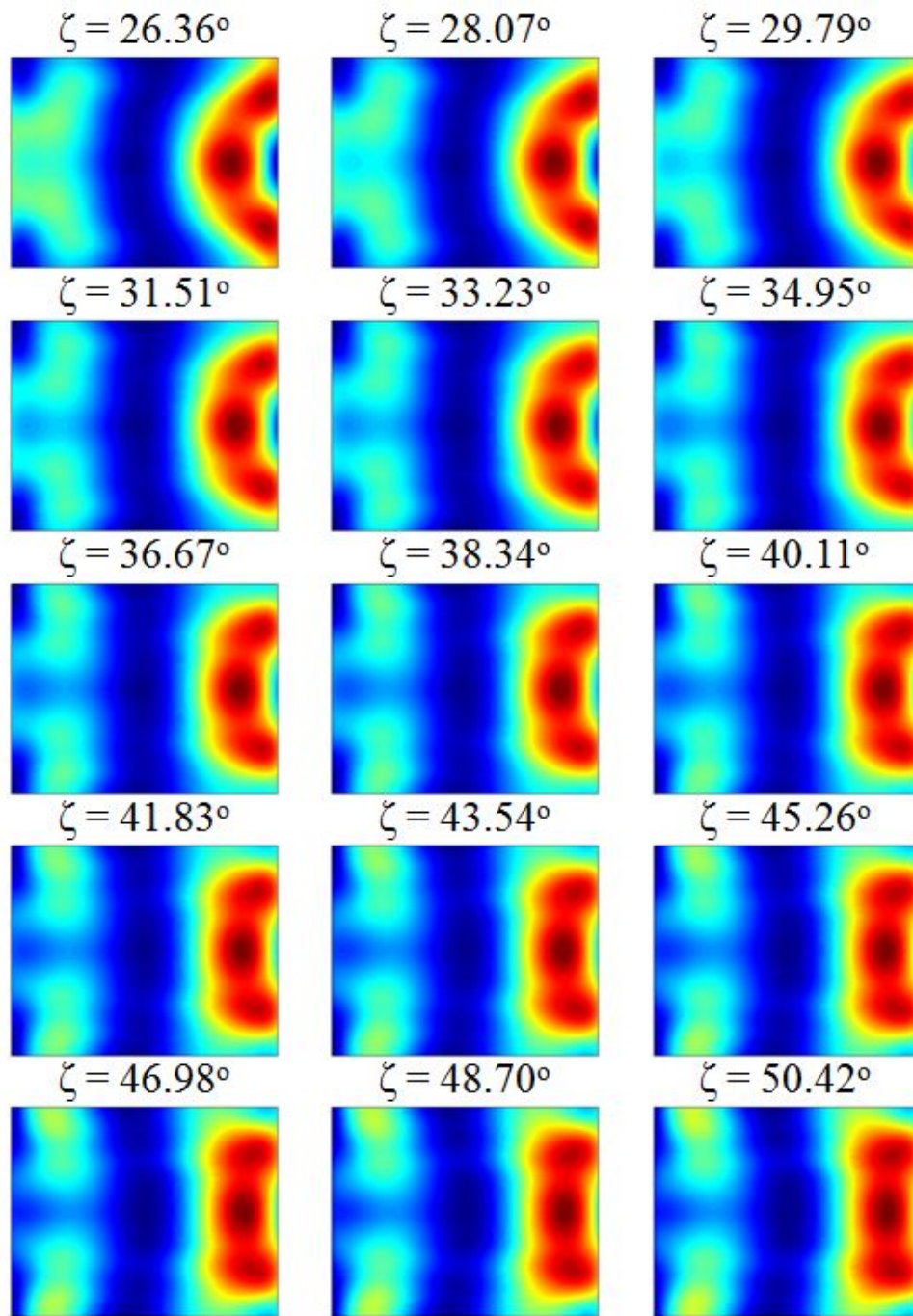


Fig. B.3. Additional scattering images shown for incident angles $\zeta=26.36^\circ$ through $\zeta=50.42^\circ$.

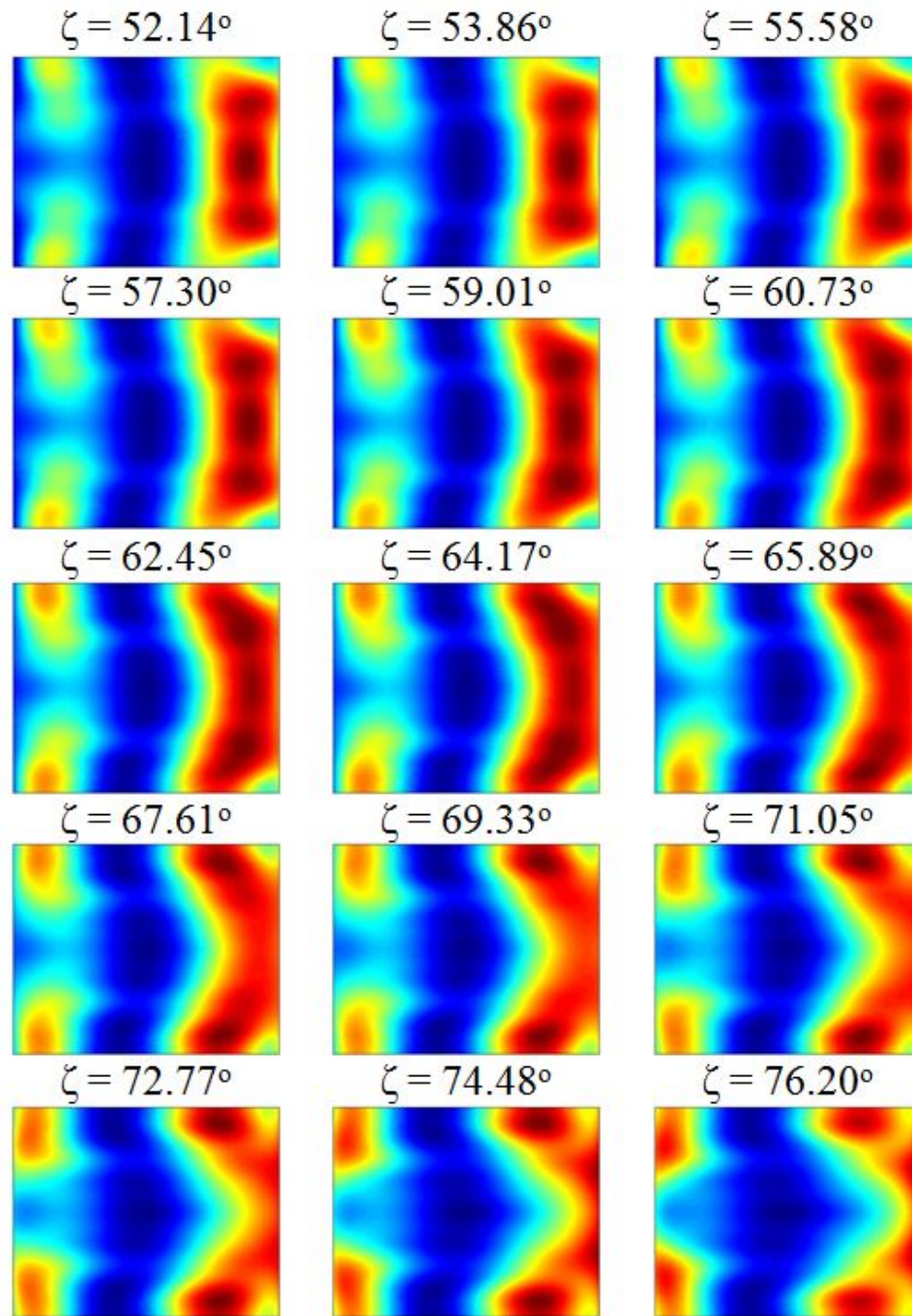


Fig. B.4. Additional scattering images shown for incident angles $\zeta=52.14^\circ$ through $\zeta=76.20^\circ$.

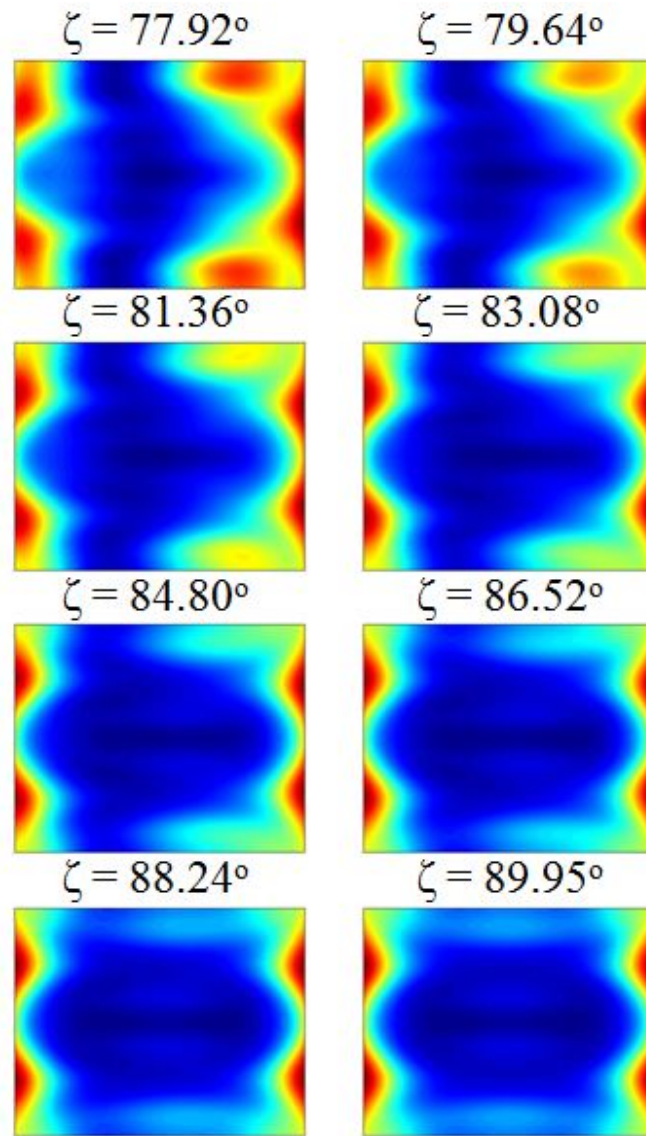


Fig. B.5. Additional scattering images shown for incident angles $\zeta=77.92^\circ$ through $\zeta=89.95^\circ$.

APPENDIX C

SPHEROIDAL COORDINATES

Partial differential equations commonly encountered in physical applications are often separable in multiple coordinate systems. The Helmholtz equation given by (7.12) is separable in 11 coordinate systems including hyperbolic, cylindrical, and spheroidal [118]. The spheroidal coordinate system is composed of two coordinate systems, prolate and oblate spheroidal. The prolate spheroidal coordinate system is relatively complex and was used to solve Maxwell's equations for the electromagnetic scattering of light by a spheroidal particle. Here the prolate spheroidal coordinate system is discussed in greater detail.

The conventions of prolate spheroidal coordinates are similar to those of spherical coordinates. A radial coordinate, assigned to ξ , is included, which describes the distance from a given point to the origin. The azimuthal angle is given by ϕ and the inclination angle by η . Surfaces of constant ξ form ellipsoids and surfaces of constant η form hyperboloids. This convention is shown in Fig. C.1. The prolate spheroidal coordinate variables are defined over the following ranges:

$$-1 \leq \eta \leq 1, \quad 1 \leq \xi < \infty, \quad 0 \leq \phi \leq 2\pi. \quad (\text{C.1})$$

The axis of revolution is chosen to be the z axis from which η is measured. A value of 1 indicates that η is directed along the positive z axis, a value of -1 indicates it is directed along the negative z axis, and 0 indicates it is orthogonal to the z axis. The incident plane is defined as the plane, which includes the z axis and the incident radiation. The x axis, from which ϕ is measured, is chosen to lie in the incident plane. The y axis is defined to be orthogonal to the x and z axes in the usual right-handed system.

The prolate spheroidal coordinates are related to cartesian coordinates through the following transformation:

$$x = d(1 - \eta^2)^{1/2}(\xi^2 - 1)^{1/2} \cos \phi, \quad (\text{C.2})$$

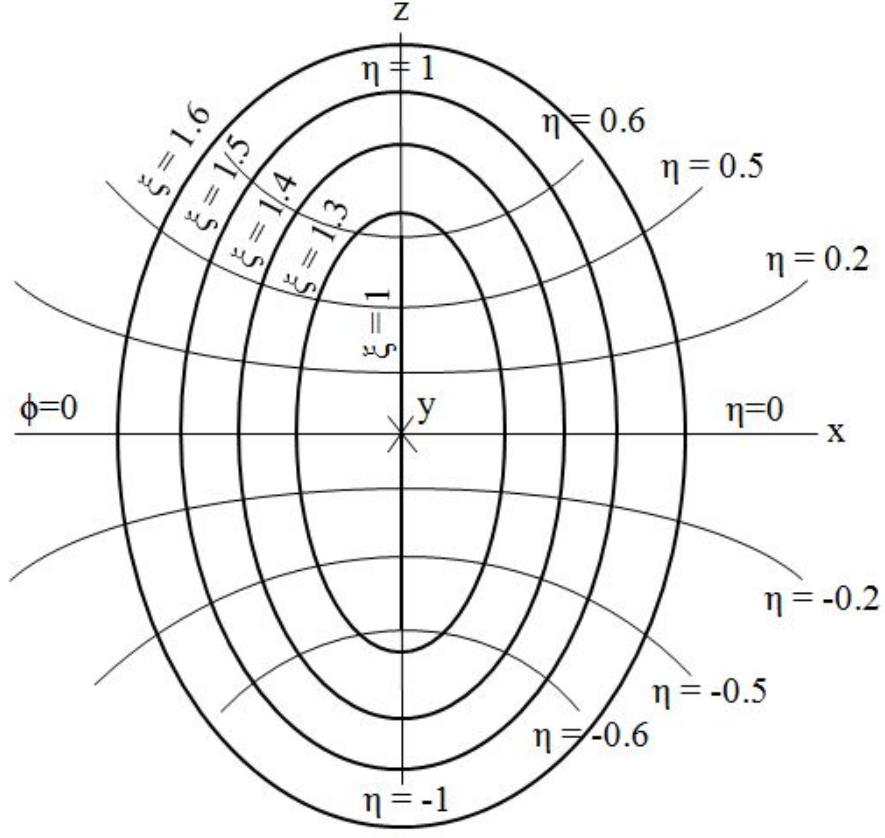


Fig. C.1. An explanation of the prolate spheroidal coordinate system.

$$y = d(1 - \eta^2)^{1/2}(\xi^2 - 1)^{1/2} \sin \phi, \quad (\text{C.3})$$

$$z = d\eta\xi. \quad (\text{C.4})$$

Vector operations defined in any coordinate system can be expressed as:

$$\nabla \Phi = \frac{1}{h_1} \frac{\partial \Phi}{\partial g_1} \hat{\mathbf{g}}_1 + \frac{1}{h_2} \frac{\partial \Phi}{\partial g_2} \hat{\mathbf{g}}_2 + \frac{1}{h_3} \frac{\partial \Phi}{\partial g_3} \hat{\mathbf{g}}_3, \quad (\text{C.5})$$

$$\nabla \cdot \mathbf{A} = \frac{1}{h_1 h_2 h_3} \left[\frac{\partial}{\partial g_1} (h_2 h_3 A_1) + \frac{\partial}{\partial g_2} (h_3 h_1 A_2) + \frac{\partial}{\partial g_3} (h_1 h_2 A_3) \right], \quad (\text{C.6})$$

$$\nabla \times \mathbf{A} = \frac{1}{h_1 h_2 h_3} \begin{vmatrix} h_1 \hat{\mathbf{g}}_1 & h_2 \hat{\mathbf{g}}_2 & h_3 \hat{\mathbf{g}}_3 \\ \frac{\partial}{\partial g_1} & \frac{\partial}{\partial g_2} & \frac{\partial}{\partial g_3} \\ h_1 A_1 & h_2 A_2 & h_3 A_3 \end{vmatrix}, \quad (\text{C.7})$$

$$\nabla^2 \Phi = \frac{1}{h_1 h_2 h_3} \left[\frac{\partial}{\partial g_1} \left(\frac{h_2 h_3}{h_1} \frac{\partial \Phi}{\partial g_1} \right) + \frac{\partial}{\partial g_2} \left(\frac{h_3 h_1}{h_2} \frac{\partial \Phi}{\partial g_2} \right) + \frac{\partial}{\partial g_3} \left(\frac{h_1 h_2}{h_3} \frac{\partial \Phi}{\partial g_3} \right) \right], \quad (\text{C.8})$$

wherein the scale factors uniquely determine a particular coordinate system. The prolate spheroidal scale factors are given by:

$$h_\xi = \frac{d(\xi^2 - \eta^2)^{1/2}}{(\xi^2 - 1)^{1/2}}, \quad (\text{C.9})$$

$$h_\eta = \frac{d(\xi^2 - \eta^2)^{1/2}}{(1 - \eta^2)^{1/2}}, \quad (\text{C.10})$$

$$h_\phi = d(1 - \eta^2)^{1/2}(\xi^2 - 1)^{1/2}. \quad (\text{C.11})$$

The prolate spheroidal coordinate system is an orthogonal coordinate system commonly encountered in scattering and radiative (antenna) problems, despite its relative complexity. The physical properties of spheroids allow for parameters, such as eccentricity, to be adjusted and generalized to a vast range of objects. Distorted spheroids can be used to model discs, cylinders, and spheres. This makes the spheroidal coordinate system a powerful tool in scattering and radiative applications, as well as diffusive tomographic imaging.

APPENDIX D

LETTERS OF PERMISSION



Dear Dr. Hart,

Thank you for contacting the Optical Society.

Because you are the author of the source paper which you wish to reproduce, OSA considers your requested use of its copyrighted materials to be permissible within the author rights granted in the Copyright Transfer Agreement submitted by the requester on acceptance for publication of his/her manuscript. It is requested that a complete citation of the original material be included in any publication.

Best,

A handwritten signature in cursive script, appearing to read "Hannah Bemba".

Hannah Bemba

Hannah Bemba
January 18, 2012
Authorized Agent, The Optical Society



UtahStateUniversity

Center for Atmospheric and Space Sciences

01/20/2012

I hereby give Vern Hart permission to include my coauthored work along with the appropriate citations in his doctoral dissertation for the degree of PhD in Physics at Utah State University. The coauthor contribution consists of two manuscripts:

Three-Dimensional Tomographic Reconstruction of Mesospheric Airglow Structures Using Two-Station Ground-Based Image Measurements

Tomographic Reconstruction of Polar Mesospheric Cloud Profiles from Image Data Collected During the NASA AIM Satellite Mission

Sincerely,

A handwritten signature in blue ink, reading "D. Pautet", with a long horizontal flourish extending to the right.

Pierre-Dominique Pautet
Center for Atmospheric and Space Sciences
Utah State University
4405 Old Main Hill
Logan, UT 84322-4405



Department of Electrical and Computer
Engineering

01/20/2012

I hereby give Vern Hart permission to include my coauthored work along with the appropriate citations in his doctoral dissertation for the degree of PhD in Physics at Utah State University. The coauthor contribution consists of two manuscripts:

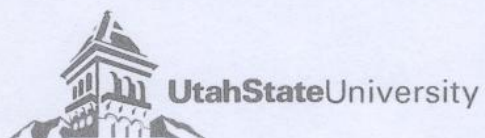
Three-Dimensional Tomographic Reconstruction of Mesospheric Airglow Structures Using Two-Station Ground-Based Image Measurements

Tomographic Reconstruction of Polar Mesospheric Cloud Profiles from Image Data Collected During the NASA AIM Satellite Mission

Sincerely,

Brent Carruth

Brent Carruth
Department of Electrical and Computer Engineering
Utah State University
4120 Old Main Hill
Logan, UT 84322-4120



Department of Physics

01/20/2012

I hereby give Vern Hart permission to include my coauthored work along with the appropriate citations in his doctoral dissertation for the degree of PhD in Physics at Utah State University. The coauthor contribution consists of two manuscripts:

Three-Dimensional Tomographic Reconstruction of Mesospheric Airglow Structures Using Two-Station Ground-Based Image Measurements

Tomographic Reconstruction of Polar Mesospheric Cloud Profiles from Image Data Collected During the NASA AIM Satellite Mission

Sincerely,

Michael Taylor
Department of Physics
Utah State University
4415 Old Main Hill
Logan, UT 84322-4415



UtahStateUniversity

Center for Atmospheric and Space Sciences

01/20/2012

I hereby give Vern Hart permission to include my coauthored work along with the appropriate citations in his doctoral dissertation for the degree of PhD in Physics at Utah State University. The coauthor contribution consists of two manuscripts:

Three-Dimensional Tomographic Reconstruction of Mesospheric Airglow Structures Using Two-Station Ground-Based Image Measurements

Tomographic Reconstruction of Polar Mesospheric Cloud Profiles from Image Data Collected During the NASA AIM Satellite Mission

Sincerely,

A handwritten signature in black ink, appearing to read 'Yucheng Zhao', written in a cursive style.

Yucheng Zhao
Center for Atmospheric and Space Sciences
Utah State University
4405 Old Main Hill
Logan, UT 84322-4405

CURRICULUM VITAE

Vern P. Hart

May 2012

Postdoctoral Research Fellow
 Department of Radiation Oncology
 The Medical College of Wisconsin
 8701 Watertown Plank Road
 Milwaukee, WI 53226

N34W23160 Circle Ridge Road
 Apartment # 202
 Pewaukee, WI 53072
 (385) 234-9493
vhart@mcw.edu

Current Position

The Medical College of Wisconsin	Imaging Science	03/2012-Present
----------------------------------	-----------------	-----------------

Education

Utah State University	Physics	PhD 2012
Brigham Young University	Physics	BS 2006

Research Experience

Research Assistant Department of Physics	Utah State University	2009-2012
Research Fellow Department of Physics	Brigham Young University	2005-2006

Teaching Experience

AP Physics Teacher	Clear Creek High School League City, Texas	2007-2008
Lab Instructor Physics 2200/2210	Utah State University	2009

Honors, Awards, and Scholarships

- Recipient of the New Century Scholarship
- Recipient of the Centennial Scholarship
- Recipient of the Seely-Hinckley Scholarship
- Three-Time Member of Dean's Honor List
- Elected to National Physics Honor Society (Sigma Pi Sigma)
- Outstanding Presentation Award (2nd Place) Intermountain Graduate Symposium

Professional Memberships and Organizations

- The American Association of Physicists in Medicine
- The American Physical Society
- Sigma Pi Sigma

Publications

Refereed Journal Articles

1. **V.P. Hart**, T.E. Doyle, M.J. Taylor, B.L. Carruth, P.-D. Pautet, and Y. Zhao, "Tomographic reconstruction of mesospheric airglow using 2-station ground-based image measurements," *Applied Optics* **51**, 7 (2012).
2. T.E. Doyle, R.E. Factor, C.L. Ellefson, K.M. Sorensen, B.J. Ambrose, J.B. Goodrich, **V.P. Hart**, S.C. Jensen, H. Patel, and L.A. Neumayer, "High-frequency ultrasound for intraoperative margin assessments in breast conservation surgery: a feasibility study," *BMC Cancer* **11**, 444 (2011).

Articles in Review

1. T.E. Doyle, J.B. Goodrich, B.J. Ambrose, **V.P. Hart**, S.C. Jensen, K.M. Sorensen, R.E. Factor, H. Patel, C.L. Ellefson, and L.A. Neumayer, "High-frequency ultrasound for the evaluation of margins during breast conservation surgery," *Journal of the Acoustical Society of America*.

Articles to be Submitted

1. **V.P. Hart**, T.E. Doyle, M.J. Taylor, B.L. Carruth, P.-D. Pautet, and Y. Zhao, "Tomographic Reconstruction of Polar Mesospheric Cloud Profiles from Image Data Collected During the NASA AIM Satellite Mission."

2. **V.P. Hart**, and T.E. Doyle, "Monte Carlo Simulation of Diffuse Light Propagation in Biological Tissue Using an Optical Spheroidal Scattering Solution."

Theses and Dissertations

1. Airy Wave Packets as Quantum Solutions for Recovering Classical Trajectories
2. The Application of Tomographic Reconstruction Techniques to Sparse Imaging Configurations in Atmospheric Science and Biomedical Optics

Presentations

Conference Papers

1. **V. Hart**, T. Doyle, B. Carruth, Y. Zhao, and M. Taylor, "Tomographic imaging of noctilucent clouds," 2010 Four Corners Section of the American Physical Society Fall Meeting, 15-16 October 2010, Ogden, Utah.
2. T.E. Doyle, **V. Hart**, and B. Ambrose, "Simulation of ultrasonic scattering in breast tissue based on cell and tissue morphology," 158th Meeting of the Acoustical Society of America, 26-30 October 2009, San Antonio, Texas. Abstract: Journal of the Acoustical Society of America **126** (4, Pt. 2), 2274 (2009).
3. S. Jensen, T. Doyle, **V. Hart**, J. Goodrich, L. Neumayer, R. Factor, and C. Ellefson, "The *ex vivo* detection of human breast cancer through high-frequency ultrasound," 2010 Four Corners Section of the American Physical Society Fall Meeting, 15-16 October 2010, Ogden, Utah.
4. S. Martini, R.J.T. Pichardo, S.C. Jensen, **V. Hart**, and T.E. Doyle, "Monitoring bubble dynamics in soybean oil," 101st American Oil Chemists Society Annual Meeting and Expo, 16-19 May 2010, Phoenix, Arizona.

International Conference Papers

1. T.E. Doyle, S. Martini, S.C. Jensen, R.J.T. Pichardo, and **V. Hart**, "Ultrasonic spectral analysis of cavitation bubbles in vegetable oils," Second Pan-American/Iberian Meeting on Acoustics, 15-19 November 2010, Cancun, Mexico. Abstract: Journal of the Acoustical Society of America **128** (4, Pt. 2), 2314 (2010).

Additional Presentations

1. **V. Hart** and T. Doyle, "The application of tomographic methods to the translation of multipolefields in multiple scattering," Intermountain Graduate Research Symposium, Logan, Utah, March 31, 2010.

2. **V. Hart** and T. Doyle, "Tomography of limited-angle projection data," Intermountain Graduate Research Symposium, Logan, Utah, March 24, 2011.
3. **V. Hart** and J.-F. Van Huele, "Airy wave packets as quantum solutions for recovering classical trajectories," Spring Research Conference, Provo, Utah, March 11, 2006.

Poster Sessions

1. **V. Hart** and J.-F. Van Huele "Is there a quantum mechanical description of Thomson's e/m experiment?" College of Physical and Mathematical Sciences - Homecoming Week Alumni Poster Session, Brigham Young University, Provo, Utah, October 14, 2005.

Research Activities

Medical Physics

Biophysics and Scattering

- Developed novel Monte Carlo simulation techniques based on spheroidal scattering for modeling of diffuse light propagation in biological tissue.
- Assisted in experimental acoustic testing of breast cancer lesions extracted during lumpectomy surgeries.
- Developed optical scattering models and tomographic inversion methods for imaging of biological tissue.

Tomographic and Acoustic Imaging

- Designed tomographic inversion algorithms for use in reconstructing vertical profiles of airglow emissions and polar mesospheric clouds from ground-based and satellite imagery.
- Performed experimental testing of the effects of ultrasound on the crystallization properties of lipids at the microscopic level.
- Studied cavitation and crystallization in lipid systems using computational models to interpret ultrasonic data.

Computational Physics

Digital Image Analysis

- Created algorithms for use in computer vision applications such as edge detection, object recognition, and image segmentation.
- Designed algorithms to model the geometry of organs using skeletal structures formed from medial locus representations.

Deformable Image Registration

- Implemented numerical methods such as least-squares optimization and optical flow for use in registration of CT and cone-beam CT images.
- Applied finite element methods and solid modeling algorithms for use in deformable image registration techniques.

Teaching Activities

Curriculum Development

- Developed course curriculum for Standard, Pre-AP, Honors, and Advanced Placement physics students at Clear Creek High School while working as a physics teacher.
- Assisted in Developing test preparation material for students preparing to take the AP Physics exam.
- Designed a physical science section study course for students preparing to take the TAKS (Texas Assessment of Knowledge and Skills) exam.

Tutoring Experience

- Sylvan Learning Center, Orem, Utah (2008)
- Utah State University Department of Physics Learning Center (2009)
- Tutor.com Physics e-tutor (2010-Present)
- Clear Creek High School TAKS Preparation Program (2008)

Additional Experience

Programming Skills

- C++
- MATLAB
- FORTRAN
- OOP
- ITK
- LaTeX
- Maple
- Labview

Research Projects

RC Grant, Utah State University (2011)
Three-Dimensional Optical CT Scanner for Breast and Prostate Cancer
Role: Assistant Researcher \$19,058

NSF, Grant No. ATM 0536876 (2006 – 2011)
Development and Optimization of Tomographic Imaging Methods for Advanced Gravity Wave Studies in the MLT Region
Role: Assistant Researcher \$494,148

NIH-NCI, Grant No. 1 R21 CA131798-01A1 (2008 – 2010)
Histology-Based Computational Tools for Ultrasonic Differentiation of Neoplasms
Role: Assistant Researcher \$334,846

Co-Authored Proposals and Annual Reports

RC Grant, Utah State University (2011) “Three-Dimensional Optical CT Scanner for Breast and Prostate Cancer,” Funded in 2010 (\$19,058).

Year-end (2010) report for NSF, Grant No. ATM 0536876, “Development and Optimization of Tomographic Imaging Methods for Advanced Gravity Wave Studies in the MLT Region.”

Collaborators and Advisors

- Medical College of Wisconsin, Milwaukee, WI (Dr. X. Allen Li, PhD)
- Huntsman Cancer Institute, Salt Lake City, UT (Dr. Leigh Neumayer, MD)
- Center for Atmospheric and Space Sciences, Logan, UT (Dr. Michael J. Taylor, PhD)
- Utah Valley University, Orem, UT (Dr. Timothy E. Doyle, PhD)

Outreach Participation

- Science Fair Judge (Clear Creek High School)
- BYU Science Demonstration Team (performed demo shows at local elementary schools)
- Participated in USU “Physics Day at Lagoon,” an outreach program for secondary science students in the state of Utah, summer 2009, 2010, and 2011 (assisted with physics knowledge bowl competition).

Volunteer Experience

- Y Group Leader, BYU New Student Orientation, summer 2005, fall 2005, fall 2006 (assisted in campus orientation of incoming freshman).
- Transfer Student Group Leader, BYU New Student Orientation, winter 2006 (assisted in campus orientation of incoming transfer students).
- Y Group Captain, BYU New Student Orientation, summer 2006 (conducted orientation seminar for new Y group leaders).

Additional Employment

Inventory Specialist, Quickutz, Inc. Orem, Utah, 2003-2004 (provided inventory management for scrapbooking company, used computer software to track supply quantities and predict shortages).

Humanitarian Service

Missionary service in Nebraska, Iowa, and Kansas, aided in tornado clean-up and relief efforts, participated in various community and church service projects.

Interests and Hobbies

Spending time with family, movies, sports.